Title
Supramolecular Assembly of Polymers, Organic Semiconductors, and Nanoparticles

Author
Rancatore, Benjamin

Publication Date
2013

Peer reviewed|Thesis/dissertation

Supramolecular Assembly of Polymers, Organic Semiconductors, and Nanoparticles

By

Benjamin John Rancatore

A dissertation submitted in partial satisfaction of the

requirements for the degree of

Doctor of Philosophy

in

Chemistry

in the

Graduate Division

of the

University of California, Berkeley

Committee in charge:

Professor Ting Xu, Chair
Professor Peidong Yang
Professor Andrew Minor

Fall 2013

Supramolecular Assembly of Polymers, Organic Semiconductors, and Nanoparticles

by

Benjamin John Rancatore

Abstract

Supramolecular Assembly of Polymers, Organic Semiconductors, and Nanoparticles

by

Benjamin John Rancatore

Doctor of Philosophy in Chemistry

University of California, Berkeley

Professor Ting Xu, Chair

This dissertation focuses on the supramolecular self-assembly of organic semiconductor small molecules (SMs), polymers, and inorganic nanoparticles (NPs) for potential applications in solution processable optical, electronic, and stimuli-responsive devices. Highly crystalline, functional SMs have a number of desirable optical and electronic properties, but their strong tendency to aggregate makes it challenging to solution process them and optimize their morphology and macroscopic alignment in thin films. Block copolymers (BCPs) are readily solution processable and assemble into well-defined, nanoscopic arrays, desirable for a number of device applications. BCP-based supramolecules can be constructed by attaching functional SMs through secondary interactions, such as hydrogen bonding, to one or more blocks of a BCP. By this method, the advantages of these two materials can potentially be combined. However, the assembly of supramolecules based on highly crystalline SMs is less straightforward and has been less thoroughly investigated compared to their non-functional counterparts.

Macroscopically aligned, nanoscopic assemblies of organic semiconductors were achieved without hindering the electronic properties of the semiconductor by constructing organic semiconductor-based supramolecules. In bulk and thin films, a number of potentially useful morphologies for optical and electronic devices were formed by tuning the annealing conditions. The high degree of crystallinity of the SM was also found to greatly increase the BCP periodicity of the supramolecule and enhanced its thermally-responsive properties compared to supramolecules based on less crystalline SMs.

This led to an investigation of supramolecules based on two different families of SMs, where the composition of the crystalline core, the location (side- vs. end-functionalization) of the alkyl solubilizing groups, and the constitution (branched vs. linear) of the alkyl groups were varied. The crystallinity and packing of the SMs were identified as key parameters governing the overall assembly and packing of the supramolecules.

Supramolecules based on non-functional SMs have also been utilized as a template to direct the assembly of inorganic NPs through favorable interactions between the SMs and the NP ligands. Using organic semiconductor-based supramolecules as the template, the effects of the SM phase

behavior as well as the NP size and loading rate on the assembly of supramolecular nanocomposites were investigated. While the assembly of these nanocomposites based on highly crystalline SMs was found to be distinct from both supramolecular nanocomposites based on less crystalline SMs and supramolecules based on highly crystalline SMs without NPs, nanostructured arrays of organic and inorganic semiconductors were obtained. These studies present a versatile method for the coassembly of polymers, highly crystalline functional SMs, and NPs for the fabrication of optical, electronic, and stimuli-responsive devices.

Supramolecular Assembly of Polymers, Organic Semiconductors, and Nanoparticles

Table of Contents

Acknowledgments

First off, I am grateful for the guidance and support that Ting has given me throughout my years in graduate school. The work described in this dissertation would not have been possible without her. I am especially appreciative of how supportive she has been in my learning new skills and techniques that weren't directly necessary for my project and for exposing me to collaborations with other groups.

Thank you to all of the collaborators who synthesized the small molecules and nanoparticles used throughout this dissertation and who tested the transistor devices in Chapter 2. A special thanks go to Dr. Clayton Mauldin, Dr. BongSoo Kim, David Hanifi, and Noah Bronstein. Without them, this project would not have existed.

To all the current and former members of my lab, I seriously doubt that there are many research groups in the world who get along as well as we have, and I am immensely grateful for that. In particular, I'm grateful for the camaraderie built and fruitful discussions during those long weeks and nights at the beamline with Kari Thorkelsson, Joseph Kao, and Peter Bai. Kari has also been an invaluable resource for all things technology, a bouncing board for ideas, and an insightful part-time psychologist. I'm also thankful for the guidance, moral support, and colorful stories offered to me by Dr. Alexander Mastroianni during the early years of my time in grad school. And to Susan Liu for helping me navigate the various university administrative mazes and giving me excuses to take much needed boba breaks.

I'd like to recognize all of the valuable friends that I've made in my time at Berkeley. "Tea time" has frequently been the highlight of my week and has helped me to put things in perspective.

My family has always been supportive of me throughout my life and have backed me even when they didn't really understand what I was doing. For fostering my love of science through extensive trips to the Exploratorium and buying me a variety of scientific toys, I thank my Aunt Roberta and Uncle George.

Lastly, I'd like to thank Rena Jan and Toro Jancatore for putting up with me during the ups and downs of grad school more closely than anyone else. I don't know if I could have made it without your support, entertainment, and love.

Chapter 1
Opportunities of Functional Small Molecule-Based Supramolecules

§ 1.1 Introduction

Functional small molecules (SMs), such as organic semiconductors (OSs) and liquid crystals (LCs), are attractive materials for the fabrication of low-cost optical and electronic devices. They have a number of desirable properties including high extinction coefficients, tunable band gaps, unique packing structures, and interesting optical and responsive properties. These materials have seen use in a number of areas including photovoltaics (PVs), light-emitting diodes (LEDs), thin film transistors (TFTs), optical devices, and stimuli-responsive materials. However, they face a number of challenges including dewetting during solution processing and optimization of their morphology, nanostructures, and macroscopic alignment. Block copolymers (BCPs) are amenable to solution processing and assemble into well-defined nanoscopic morphologies on the order of tens of nanometers. However, functional polymers, such as conjugated polymers, face challenges with the control of their purity, polydispersity, regioregularity, and molecular weight. BCP-based supramolecules can be constructed by attaching functional SMs to BCPs through secondary interactions, such as hydrogen bonding and metal ligation. This approach allows for the loading of the SMs above and below a 1:1 stoichiometry of SMs to attachment sites without synthesizing new polymers and introduces a thermally responsive component to the system. These supramolecules assemble hierarchically on the order of tens of nm from the BCPs and a few nm from the SMs and can potentially combine the advantages of both classes of materials.

There are a number of thermodynamic and kinetic factors that affect the overall assembly of these supramolecules. These include: the BCP microphase separation, the crystallinity and packing of the SM, the entropic penalty for deforming the polymer chain, and the binding strength between the polymer and SM. Attachment of the SMs can affect the BCP chain architecture, stiffness, interaction parameter (χ), and spring constant. Conversely, the polymer may affect the SMs crystal structure or its ability to crystallize. Kinetically, the distribution and diffusion rate of the SMs can depend on the T_m of the SM and the relative interaction parameter (χ) between the SMs and each block of the BCP at a given annealing temperature.[1-3] With all of these considerations in mind, it is clear that the phase behavior of the SMs is of critical importance in its coassembly with the BCP especially for highly crystalline, functional SMs. Figure 1.1 summarizes the potential advantages, applications, and thermodynamic and kinetic considerations of supramolecules based on polymers and functional SMs.

One area in which functional supramolecules may prove useful is organic electronic devices. There are two main classes of semiconductors based on organic materials: conjugated polymers and SM OSs, each with unique strengths and weaknesses. Conjugated polymers are amenable to solution processing,[4-6] but they typically exhibit mobilities lower than their SM counterparts and their polydispersity and molecular weight must be tuned to optimize their charge mobility and optical properties.[7,8] SM OSs are more readily purified and have well-defined electronic properties,[9-16] but it can be a challenge to solution process them into uniform films.[10,17] In devices based on blends of electron donors and acceptors, the nanoscopic morphology, the macroscopic orientation, and the molecular packing of the semiconductors must be tuned in order to optimize the device efficiencies.[4,18,19] This is generally achieved by kinetically trapping the crystallization of the active layer materials.[13,14,20-25] A number of techniques have been developed to optimize the nanostructure size and quality including thermal annealing,[24] controlled solvent evaporation,[5] and the addition of high boiling point cosolvents.[26,27] However, these techniques do not yield continuous nanostructures with well-defined packing and orientation. By constructing

supramolecules based on SM OSs and BCPs, solution-processed, nanostructured assemblies of the SMs can be readily achieved while preserving the properties of the semiconductor.

This chapter will first introduce and demonstrate examples of functional SM/polymer-based supramolecules and their potential applications in optical and electronic devices. This will be followed by a brief discussion of polymeric and supramolecular nanocomposite materials, and the potential future directions of a new family of supramolecular nanocomposites based on functional SMs.

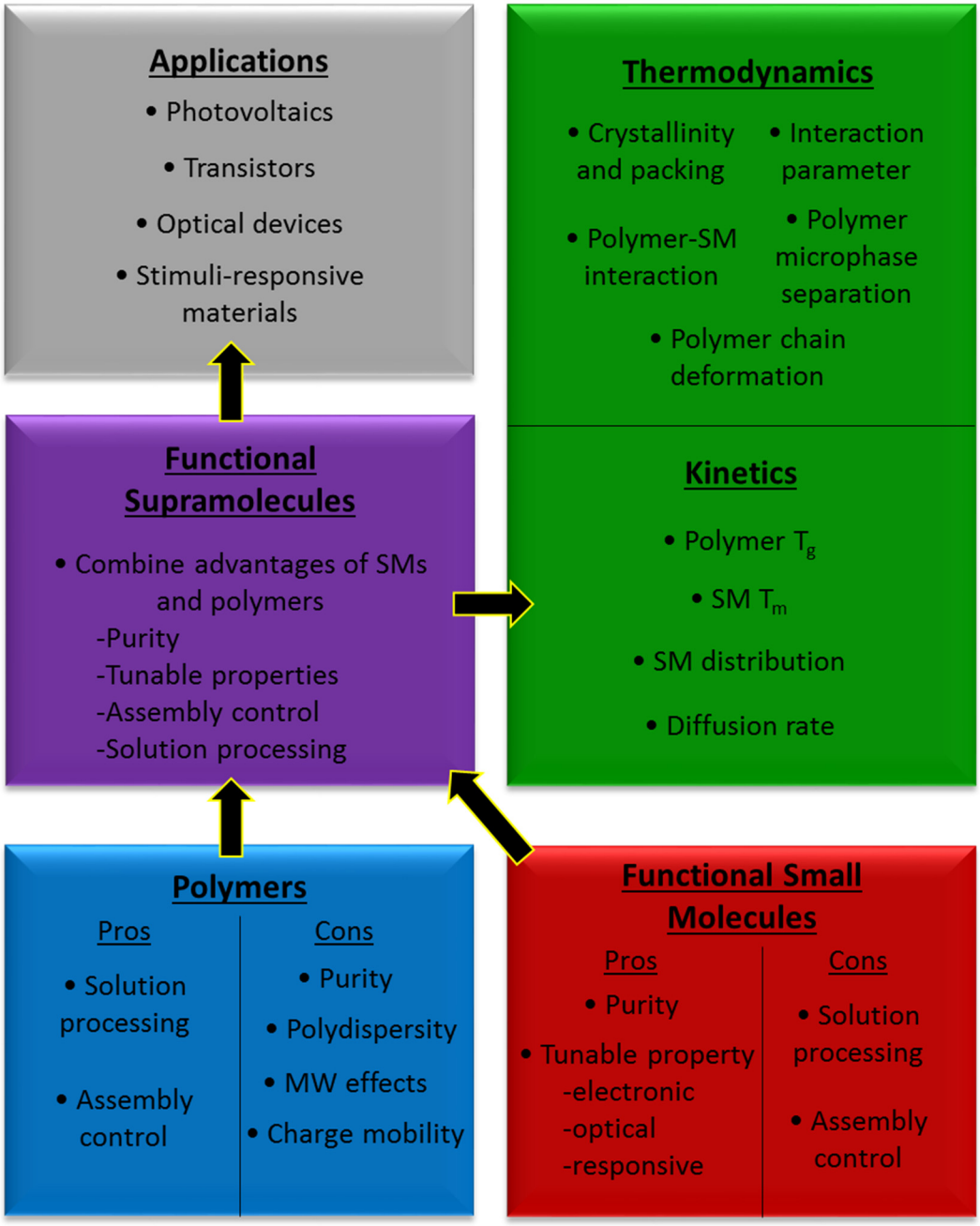

Figure 1.1. Advantages, applications, and thermodynamic and kinetic considerations of functional SM-based supramolecules.

§ 1.2 Functional SM-Based Supramolecules

BCPs with strongly interacting SMs that are covalently attached to one or more blocks of the BCP have been studied extensively and utilized in a number of areas, including LC and OS

materials. When these SMs are attached to one or more blocks of a BCP, they organize hierarchically on the order of tens of nm from the BCP framework and a few nm from the molecular packing.[28-32] This method can potentially allow for the control of the nanostructured assembly and macroscopic orientation of functional SM moieties. By attaching LC SMs to a BCP, their unique optical and stimuli responsive properties can be incorporated into the BCP, and a wide array of structural motifs have been investigated.[33-42] Donor-acceptor semiconducting BCPs have been shown to form controlled nanoscopic networks of donor and acceptor materials, which is potentially useful for OPV devices.[43-49] They have also been utilized as BCP compatibilizers to control the grain sizes and enhance the thermal stability of devices when blended with unattached donor and acceptor materials.[49] However, fine morphological and orientational control cannot be easily achieved with conjugated BCPs due to low chain mobility and strong interfacial preference of one block for the substrate.[48,50-53] Covalently linked LC or OS side-groups may also restrain the molecular packing of the attached SMs required for the desired optical or electrical properties.

BCP-based supramolecules can be constructed by attaching SMs to one or more blocks of a BCP via secondary interactions, such as hydrogen bonding, electrostatic interactions, or metal ligation.[1,2,54-64] Like BCPs with covalently attached SM side chains, these supramolecules assemble hierarchically on the order of tens of nanometers from the BCP and on the order of a few nanometers from the SM packing. There have been extensive studies on supramolecules based on functionalized alkyl SMs that do not have inherent optical or electronic properties,[1,2,57,59,62] but the noncovalent linkage between the polymers and SMs does introduce a thermally responsive component to the system.[1,2,57] They have also been shown to achieve large microdomain sizes that can be difficult for BCPs alone,[1] and selective solvent removal of the SMs after casting can lead to mesoporous materials.[65-67] SMs with optical, electronic, or stimuli responsive properties can be used to incorporate functionality into these supramolecules but are generally more crystalline and strongly interacting compared to their non-functional counterparts, which can potentially affect the assembly properties of the supramolecule. However, there have been fewer studies of BCP-based supramolecules based on these highly crystalline SMs, such as LCs and OSs.

1.2.1 LC-Based Supramolecules

LC SMs have demonstrated a number of interesting optical properties and phase transitions. By incorporating them into supramolecules, one can potentially control their orientation and macroscopic alignment and improve their processability. The observed optical properties of the LC molecules depend on the orientation and packing of the SMs, so the ability to control their assembly is critical to their applications in devices. A variety of different LC moieties have seen use in supramolecular systems, including (alkoxybenzoyloxy)benzoate,[54] biphenyl,[68-70] cholesterol,[71-73] and azobenzene.[66,74-76]

The first such LC side chain supramolecule was synthesized by Kato *et al*. using a polyacrylate homopolymer with side groups terminated with a 4-oxybenzoic acid unit designed to hydrogen bond to a SM with a trans-stilbazole ester moiety.[54] Binary mixtures of these components led to a significant enhancement of the mesophase which was attributed to the formation of an extended mesogenic unit from the hydrogen-bonded complex, as seen in Figure 1.2. However, homopolymer-based supramolecules cannot form nanostructured assemblies of SMs, which is desirable for certain optical devices. Gohy *et al.* demonstrated the first supramolecular LC BCP

using Poly(dimethylaminoethylmethacrylate)-*b*-poly(sodiummethacrylate) (PDMAEMA-*b*-PMA), where the PDMAEMA block was designed to have electrostatic binding interactions with a cholesteric SM, and the PMA block was designed to bind to an azobenzene-containing SM.[74] A number of hierarchical morphologies were achieved depending on the relative volume fraction of the BCP blocks and the loading rate of the cholesteric SM, and smectic mesophases were observed at certain combinations of these parameters. Copolymers containing both mesogens simultaneously did not microphase separate, but a unique smectic mesophase was observed.

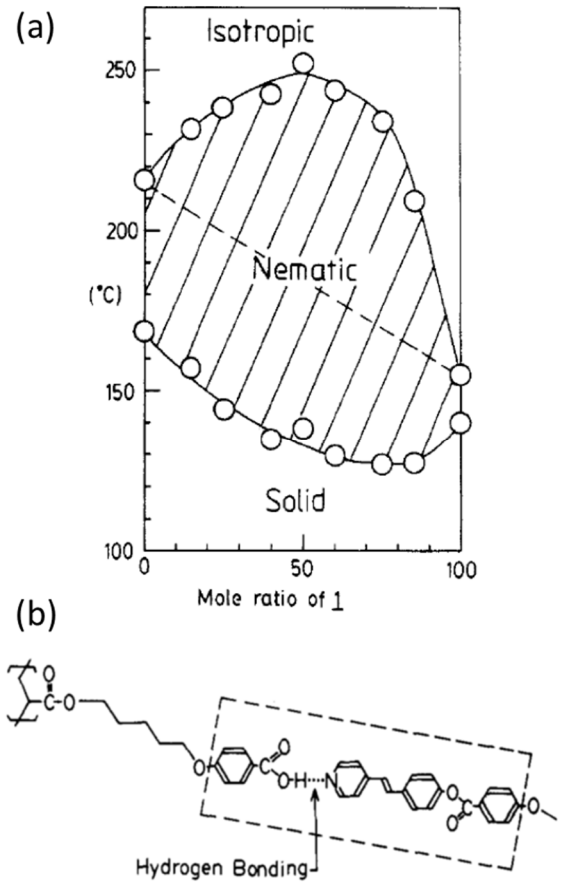

Figure 1.2. (a) Phase diagram of the supramolecule shown in (b) with a 1:1 ratio of SMs to polymer side groups. (b) Chemical structure of the LC SM-based supramolecule. The boxed region highlights the extended polymer-SM mesogen. Adapted with permission from Kato *et al.* Macromolecules **1989**, 22, 3818. Copyright 1989 American Chemical Society.

Osuji *et al.* have published a number of works using imidazole terminated, biphenyl-based LC SMs designed to hydrogen bond to the carboxylic acid groups of poly(acrylic acid) (PAA) or poly(methacrylic acid) (PMAA) in homopolymers and BCPs.[68-70,77] These supramolecules were shown to assemble hierarchically, and the SMs introduced interesting optical and thermally responsive properties to the system. Using supramolecules based on a PS-*b*-PMAA BCP and a

biphenyl SM, the photonic band gap of the material was tuned into the green.[68] When the sample was heated to an isotropic state, the photonic band gap shifted from green to orange. The orientation of the BCP and mesogenic domains of similar supramolecules based on PS-*b*-PAA could be oriented in minutes using AC electric fields[69] or magnetic fields[77] while cooling from a melt state. Due to the plasticization of the BCP from un-attached mesogens, the supramolecules could also be reoriented at a temperature between the T_g and the order-disorder transition (ODT) in some cases. Since the orientation of the LC-based supramolecules can have a significant effect on its optical properties, the use of electric and magnetic fields may prove useful for the application of these materials in devices, and the fast reorientation times offered by supramolecules could improve its scalability.

SMs with non-linear shapes, such as wedges, have also been investigated.[78-80] Tenneti *et al*. demonstrated supramolecules based on a PS-b-P4VP BCP and a bent-core molecule, 1-[4'-(3",4",5"-tridecyloxybenzoyloxy)phenyleneoxycarbonyl]-3-[(4'-hydroxyphenyl)oxycarbonyl]benzene.[78] These supramolecules adopted a smectic A LC structure within the BCP microdomains. Wang *et al*. investigated the assembly of supramolecules based on a 2-(3′,4′,5′-tris(octyloxy)benzamido)propanoic acid SM designed to bind to the pyridine groups of a P2VP-*b*-PEO BCP.[80] Despite the fact that the neat SMs did not exhibit LC ordering on their own, supramolecules based on these SMs displayed a smectic phase. This strengthened the argument that the formation of supramolecules can be used to enhance the LC character of the SMs. Additionally, the loading rate of the SMs could be used to tune the crystallinity of the PEO block.

1.2.2 OS-Based Supramolecules

OS-based supramolecules have also become a topic of interest in recent years. Supramolecules based on fullerenes have been investigated the most thoroughly and have been the topic of a few recent reviews.[81,82] Early work by Goh *et al*. demonstrated complexes of pyridine-containing C_{60} molecules[83] with four acidic polymers, poly(styrenesulfonic acid), poly(vinyl-phosphonic acid), poly(acrylic acid), and poly(methacrylic acid), as well as complexes of hydrogensulfated fullerenol[84] with poly(4-vinylpyridine) (P4VP) via ionic interactions. None of these materials showed distinct glass transitions after complexation due to the strong interactions between the fullerenes and polymer chains. X-ray photoelectron spectroscopy (XPS) and Fourier transform infrared spectroscopy (FTIR) were used to confirm the ionic nature of the binding interactions between the polymers and SMs. Fujita *et al.* used carboxylic acid-functionalized C_{60} molecules designed to hydrogen bond to the pyridine moieties of polystyrene(PS)-*b*-P4VP.[85] The amphiphilic nature of PS-*b*-P4VP was used to form polymeric micelles with a P4VP(C_{60}) core and a PS shell. This led to the formation of C_{60} NPs with relatively narrow size distributions that could be tuned by changing the degree of polymerization and relative volume fractions of the BCP. Laiho *et al.* demonstrated supramolecular assembly of PS-*b*-P4VP with non-functionalized C_{60} molecules where the pyridine groups on the polymer chains formed charge transfer complexes with C_{60}.[86] This provided an avenue to form fullerene-based supramolecules without the need for the synthesis of fullerenes with extra functional groups designed to bind to polymer chains. As the supramolecular solutions were aged, they changed color from purple (free C_{60}) to brown (pyridine-C_{60} complex), and peak shifts were observed in the UV-Vis and FTIR spectra. Unexpectedly, the

BCP morphology changed from P4VP minority cylinders to P4VP spheres as the C_{60} molecules migrated into the P4VP domains upon aging in both bulk and thin film samples. The authors hypothesized that this was due to C_{60} forming charge transfer complexes to multiple P4VP chains, as shown schematically in Figure 1.3.

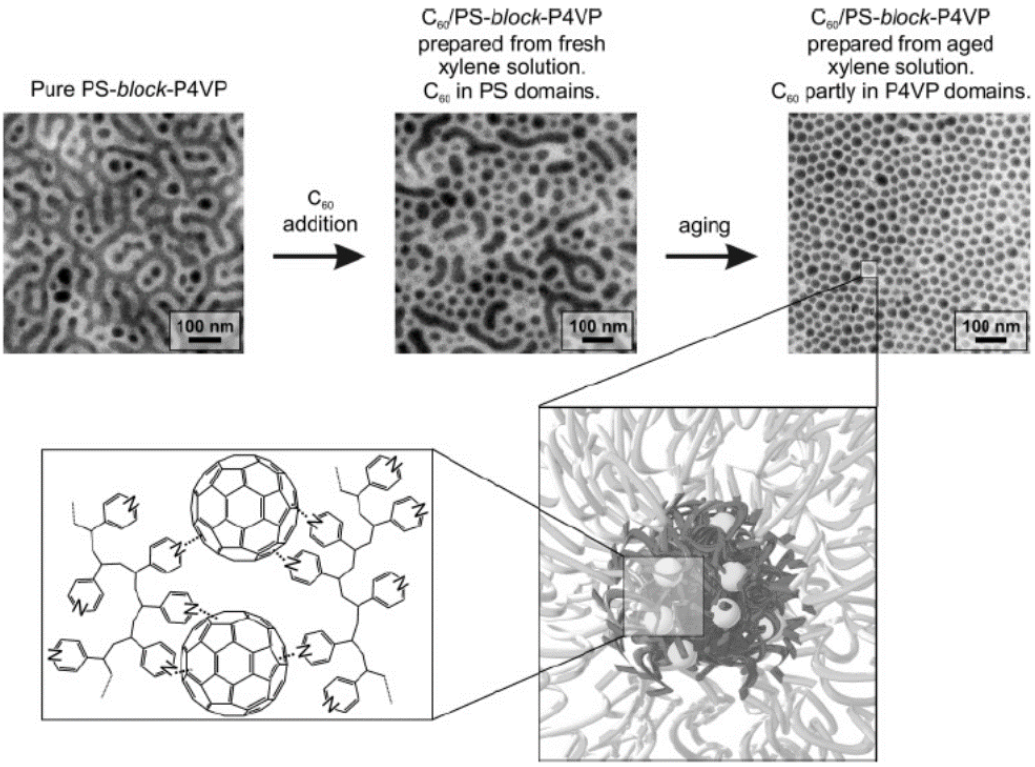

Figure 1.3. (top) TEM images of (left) neat PS-*b*-P4VP and PS-*b*-P4VP(C_{60}) supramolecules cast from (center) fresh and (right) aged solutions. Samples were stained with I_2 to enhance the contrast. (bottom) Schematic representation of the (left) pyridine-C_{60} charge transfer complexes and (right) their effects on the BCP morphology. Reprinted with permission from Laiho *et al.* Macromolecules **2006**, 39, 7648. Copyright 2006 American Chemical Society.

More recently, this idea has been expanded to conjugated BCPs, where one block was designed to bind to fullerenes, and the other was a conjugated polymer, such as poly(3-hexylthiophene), to fabricate donor-acceptor networks of controlled domain size and high thermal stability for OPV applications.[87-91] A number of recent papers by Hadziioannou *et al.* have investigated the assembly as well as electrical and optical characteristics of BCPs with a conjugated polymer-*b*-P4VP structural motif and their blends with fullerenes.[87-89] In their first work, poly(diethylhexyl-p-phenylenevinylene)(PPV)-*b*-P4VP was complexed with C_{60} molecules.[87] A homogeneous dispersion of the C_{60} molecules in the P4VP microdomains after annealing for 16 h at 180 °C was achieved with up to 10 wt% of the SM. While the lamellar morphology of the BCP was maintained, a reduction in the long range order was observed. Supramolecules with a similar structural motif were later used in the fabrication of solar cells by

complexing P3HT-*b*-P4VP with PCBM.[88] The copolymer greatly enhanced the thermal stability of the coassembly of polymer and PCBM compared to control blends of P3HT/PCBM, as shown in Figure 1.4. Within a certain loading range, the addition of PCBM was found to improve the lamellar morphology of the BCP and enhance the ambipolar charge mobility of the films.[89] Yi-Cang *et al.* synthesized an all-conjugated BCP, P3HT-*b*-poly(3-(4′-(3″,7″-dimethyloctyloxy)-3′-pyridinyl)thiophene)(P3PyT), where the P3PyT block had pyridyl-containing side groups designed to complex with PCBM.[90] This BCP was used both as the primary donor material in the active layer for OPVs and as a BCP surfactant in P3HT/PCBM blends. The highest efficiencies were achieved when P3HT-*b*-P3PyT was used as a surfactant, and it significantly improved the thermal stability of the devices after prolonged annealing. Yao *et al.* demonstrated an all-conjugated random copolymer, poly[[3-(60-bromohexyl)thiophene]-*co*-[3-(60-(1-imidazole)hexyl)thiophene]](P3HTM), which contained a mixture of photo-crosslinkable bromine groups and imidazole groups on the side chains designed to hydrogen bond to phenyl C_{61}-butyric acid (PCBA).[91] The combination of these features were shown to significantly enhance the long term thermal stability of the P3HTM/PCBA blend morphologies and device properties (75% of initial device efficiency preserved after 40 h of annealing at 130 °C).

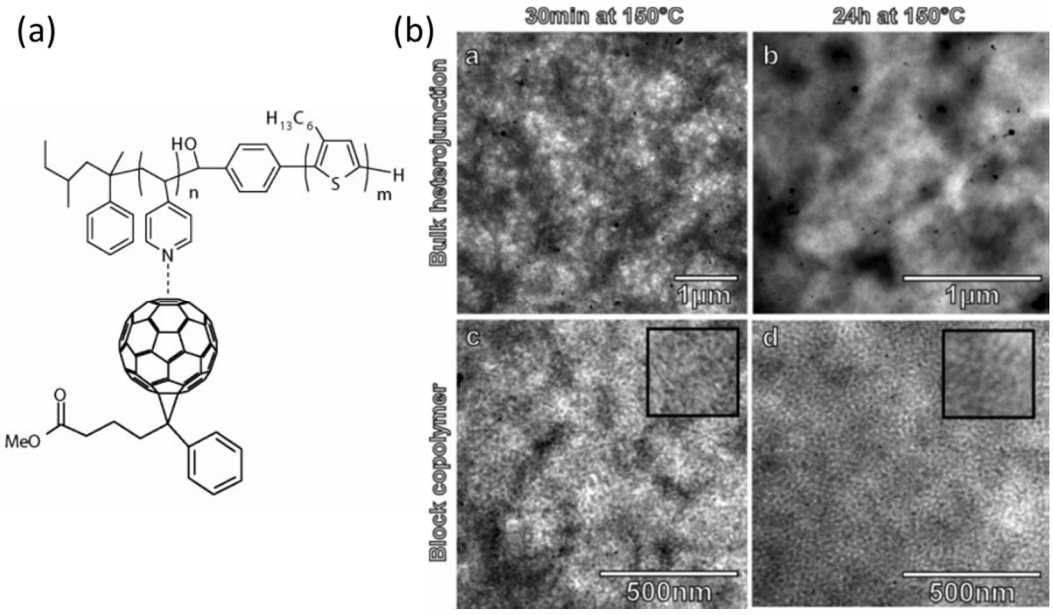

Figure 1.4. (a) Chemical structure of P3HT-*b*-P4VP(PCBM) supramolecules. (b) TEM images of thermally annealed (top) P3HT/PCBM and (bottom) P3HT-*b*-P4VP(PCBM) films. The PCBM crystal sizes are much smaller for the supramolecular films after extended annealing. Adapted with permission from Sary *et al.* Adv. Mater. **2010**, 22, 763. Copyright © 2010 WILEY-VCH Verlag GmbH & Co. KGaA, Weinheim.

Fullerene-based supramolecules have also been used for memory storage devices, such as write-once-read-many-times (WORM) memory and static random access memory (SRAM). Their electrical properties in devices have shown a significant SM loading rate and morphology

dependence. Chen *et al.* demonstrated the supramolecular assembly and nonvolatile WORM memory storage characteristics of poly[4-(9,9-dihexylfloren-2-yl)styrene](P(St-Fl))-*b*-P2VP:PCBM with the P2VP block in linear[92] and star[93] configurations. For both configurations, the charge transfer complexation between P2VP and PCBM controlled the PCBM crystal sizes and led to devices with low threshold voltages (-1.6 to -3.9 V) and high ON/OFF ratios (10^3-10^6) at low loadings of PCBM (1-5 wt%), as shown in Figure 1.4. The ON or OFF states could be maintained for over 10^4 s without obvious degradation. Higher loading rates of PCBM (10 wt% or more) led to macrophase separation of the SMs. Devices with no PCBM or a high loading did not exhibit memory storage properties. They also used PCBM blends with another fluorene-based BCP, poly[2,7-(9,9-dihexylfluorene)](PF)-*b*-P2VP, which had a conjugated backbone instead of side groups, for memory devices.[94] Devices based on the BCPs alone exhibited volatile, SRAM behavior with longer ON states for BCPs with longer P2VP blocks. The longer lifetimes were attributed to enhanced charge trapping with the longer, insulating P2VP block. Devices based on PF-*b*-P2VP(PCBM) supramolecules exhibited WORM memory behavior. PS-*b*-P4VP(PCBM) supramolecules have also seen use in devices and were shown to have morphology dependent memory characteristics.[95] Films with a PS cylinder in P4VP(PCBM) matrix morphology oriented parallel to the substrate exhibited SRAM behavior, and films with P4VP(PCBM) cylinders in the PS matrix exhibited WORM memory behavior.

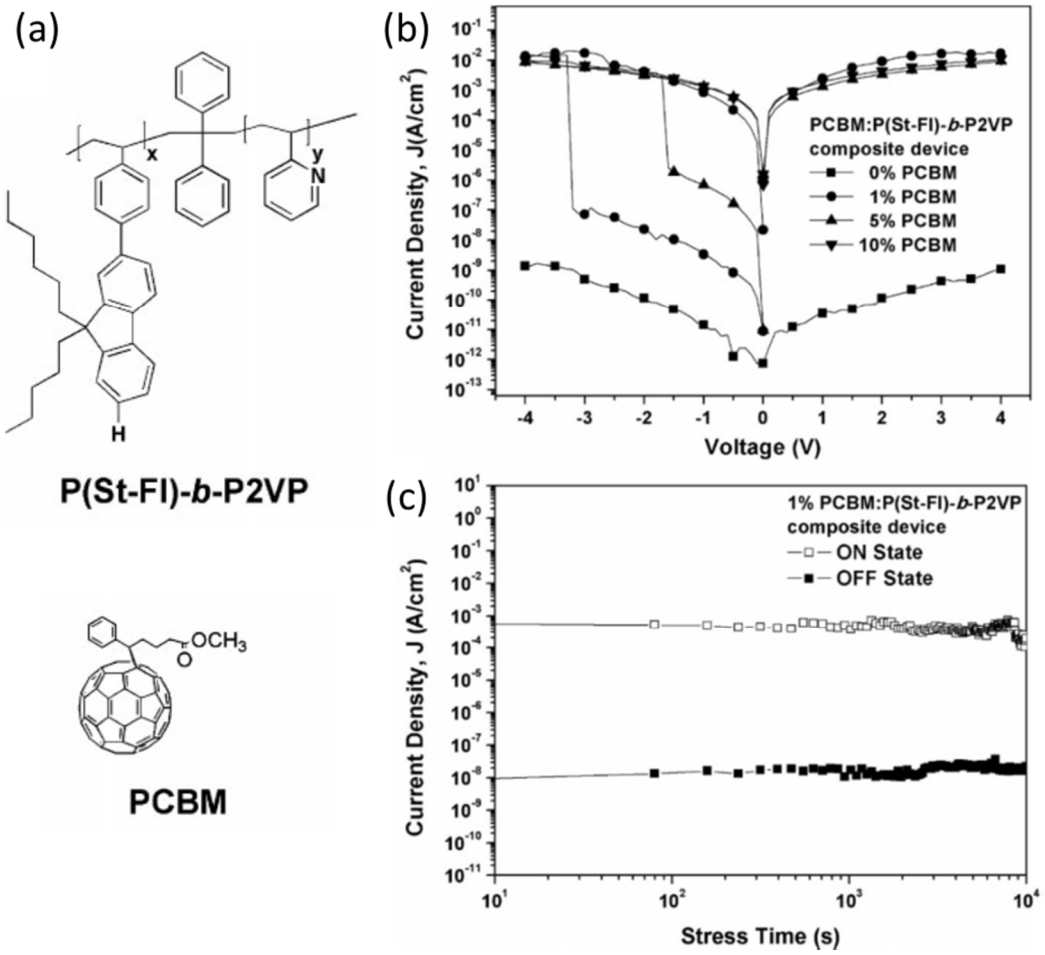

Figure 1.5. (a) Chemical structures of the BCP and SM in (P(St-Fl))-b-P2VP(PCBM) supramolecules. (b) *I-V* curves showing the PCBM loading rate dependence. (c) Retention time measurement of a 1 wt% PCBM device. Adapted with permission from Hsu *et al.* Macromol. Rapid Commun. **2011**, 32, 528. Copyright © 2011 WILEY-VCH Verlag GmbH & Co. KGaA, Weinheim.

Supramolecules have also been formed using carbon nanotubes (CNTs). Li *et al.* studied P(St-Fl)-*b*-P2VP BCPs and their blends with carboxylic acid-functionalized, single wall CNTs.[96] A wide array of morphologies of the BCP were achieved by tuning the number of repeat units on the fluorene side chains, the volume fraction of each block, the solvent used to cast the samples, and the thermal annealing history. The CNTs were successfully sequestered into the P2VP domains, and they exhibited morphology-dependent charge conductivities.

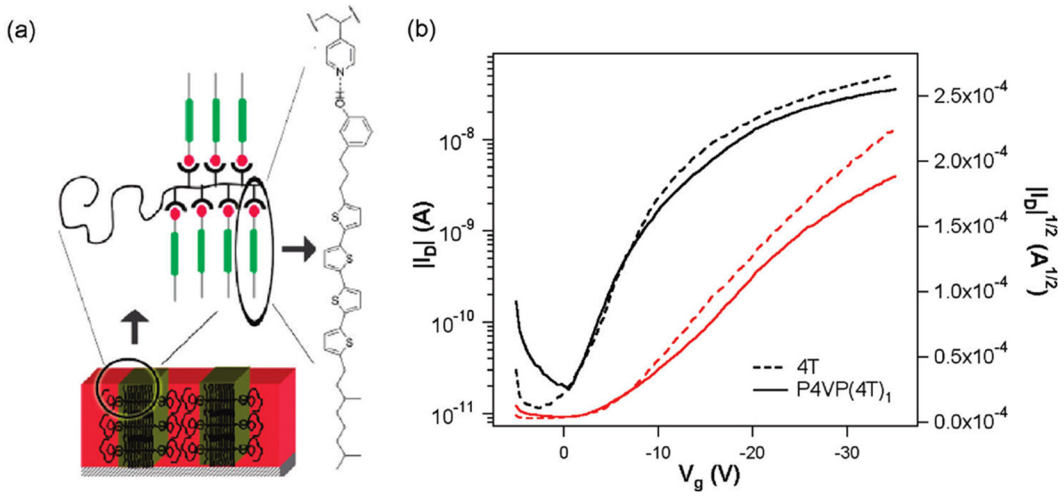

Figure 1.6. (a) Supramolecular assembly and chemical structure of PS-*b*-P4VP(4T). (b) *I-V* curves of neat 4T and P4VP(4T) supramolecules. Adapted with permission from B. J. Rancatore *et al.* ACS Nano, **2010**, 4, 2721–2729. Copyright 2010 American Chemical Society.

Blends of inert polymers and SM OSs have been shown to improve the solution processability of the semiconductors without hindering their charge mobility. In Kang *et al.*, this was demonstrated with blends of poly(α-methylstyrene) and 6,13-bis(triisopropylsilylethynyl)pentacene.[97] However, since these SMs did not bind to the polymer chain, this method did not control their assembly. In a similar vein, the supramolecular approach has been used to control the assembly of OSs and improve their solution processability without hindering their charge mobility.[98,99] These supramolecules were formed using phenol-containing oligothiophene-[98] and perylene diimide-based[99] semiconductors hydrogen-bonded to the pyridine side groups of P4VP and PS-*b*-P4VP. A schematic representation of oligothiophene-based supramolecules and their *I-V* curves as the active layer in top-contact TFTs is shown in Figure 1.6. In thin films of the oligothiophene-based supramolecules, nanostructured assemblies of the OS oriented perpendicular to the substrate could be readily achieved, ideal for OPV devices.[98] The strong crystallization of the oligothiophenes in supramolecules was shown to have a large effect on the morphology and chain architecture of both BCP blocks and significantly enhance the thermal responsiveness of the supramolecules.[100] A 70% increase in the BCP periodicity was observed when the SMs transitioned from a melt to a crystalline state. In addition, a number of potentially useful, long lived kinetically-trapped nanostructures could be accessed by tuning the annealing conditions. Tran *et al.* used magnetic fields to macroscopically align supramolecules based on imidazole-functionalized perylene diimide- SMs designed to hydrogen bond to the carboxylic acid groups of PS-*b*-poly(acrylic acid)(PAA), which could be potentially useful to control the macroscopic alignment of nanostructures over large areas in OS devices.[101] A schematic representation of the supramolecules and TEM images of their magnetically-aligned morphology is shown in Figure 1.7.

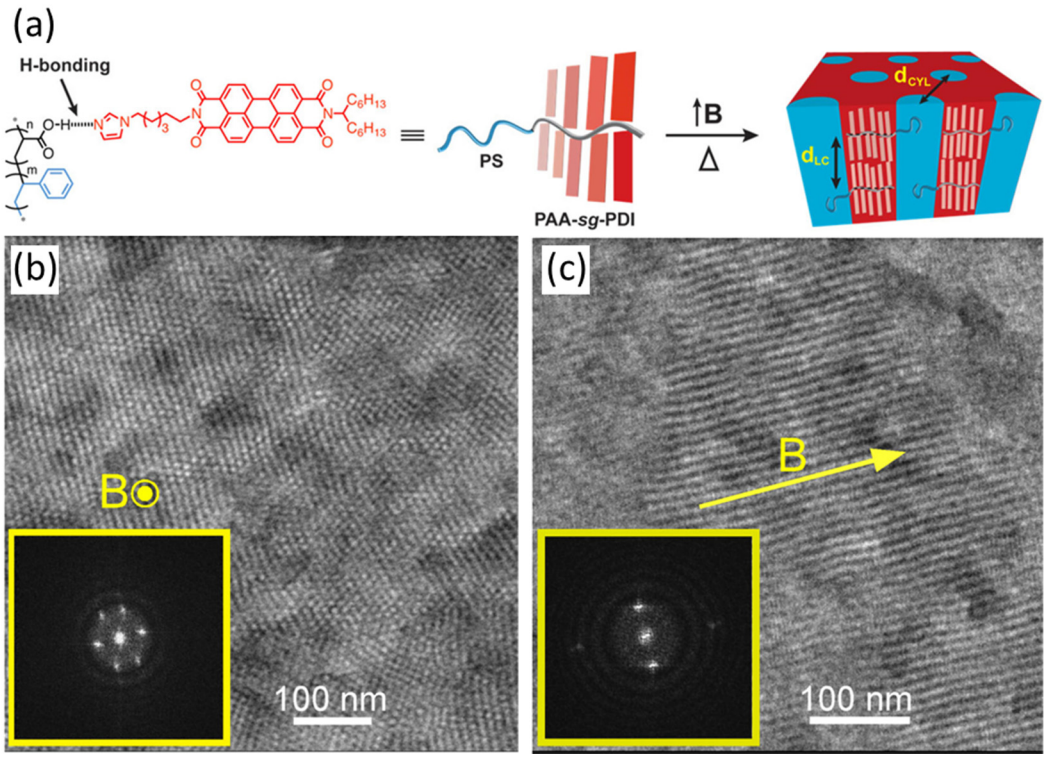

Figure 1.7. (a) Chemical structure and schematic representation of the supramolecular assembly. (b,c) Cross-sectional TEM images of supramolecules with a cylindrical morphology that were imaged (b) perpendicular and (c) parallel to the magnetic field direction. Adapted with permission from Tran *et al.* ACS Nano **2013**, 7, 5514. Copyright 2013 American Chemical Society.

Supramolecular films of pyrenebutyric acid and PS-*b*-P4VP have also been investigated[102] and was recently used as a fluorescent probe[103] to study the packing of the SMs in supramolecular thin films. H-type aggregation of the SMs was observed. By choosing selective or nonselective solvents, the supramolecular orientation could be tailored, and the fluorescence emission was enhanced compared to the neat SM both in solution and thin films. Investigations such as this are potentially helpful for improving our understanding of how the packing of the SM is affected by the supramolecular assembly method.

1.2.3 Thermodynamic and Kinetic Considerations of Functional SM-Based Supramolecules

Throughout these studies, a number of competing processes in the assembly of supramolecules based on highly crystalline functional SMs can be identified, including the BCP microphase separation, the crystallinity and packing of the SM, the entropic penalty for deforming the polymer chain, and the binding strength between the polymer and SM. The attachment of the

SMs to the BCP has a number of effects on the polymer including changes to the chain architecture, stiffness, χ, and spring constant. For example, the binding interaction between the polymer and SM forces the polymer chain to stretch to allow more SMs to attach to the polymer chain. The polymer may also affect the SM crystal structure or its ability to crystallize. In some cases, this has shown to be beneficial, where the formation of supramolecules enhanced the mesophase of LC SMs.[54] For highly crystalline SMs, the packing of the SM can play a much larger role in the overall assembly of the supramolecule compared to their less crystalline counterparts. Consequently, the phase behavior of the SMs is of critical importance in its coassembly with the BCP.

The assembly of BCP-based supramolecules is more complex compared to BCPs with covalently attached SMs. The SMs may macrophase separate from the BCP or only incorporate partially, which can depend on the strength of the secondary interaction used for attachment, the loading rate and crystallinity of the SM, and the sample treatment conditions. However, this added complexity also provides added tunability as the loading rate of the SMs above and below a 1:1 stoichiometry of SMs to attachment sites can be readily changed without synthesizing new BCPs. The non-covalent attachment of SMs also introduces a reversible, thermally responsive component to the system. The SM distribution and diffusion rate can depend on the T_m of the SM and the relative χ between the SM and each block of the BCP at different temperatures.[1-3] The SMs can also have a plasticizing effect on the polymer chains which can reduce the annealing time and/or temperature needed for the reorganization of the nanostructures.[69]

§ 1.3 Nanocomposites

Inorganic NPs display a number of interesting size-dependent optical, magnetic, and electrical properties. However, precise control of their macroscopic and interparticle ordering is requisite for their effective use in a number of devices. A rich library of BCP morphologies can be achieved on size scales comparable to NPs and are readily solution processable. Combining these two classes of materials to form organic-inorganic nanocomposites have the potential to take the advantages of both materials. Thus BCPs, and more recently BCP-based supramolecules, have been investigated as structure templates for the assembly of NPs. However, comparatively less work has been done on nanocomposites with a functional, highly crystalline organic component, such as OSs or conjugated polymers, which are potentially useful for optical and electronic devices. In this section, we will discuss different NP assembly methods in these three areas.

1.3.1 BCP-Based Nanocomposites

Hybrid nanocomposites can be fabricated using BCPs as a nanoscopic template for the assembly of various NPs into well-defined arrays that are scalable and amenable to solution processing. There are a number of factors that govern the NP assembly including the enthalpic interactions between the NP ligands and the BCP blocks, the conformational entropy loss of the polymer due to stretching around the NPs, and the entropic contribution of the number of arrangements of the NPs.[104] The enthalpic contribution of the polymer-ligand interaction can be tailored by changing the NP ligands or the side chains of the BCP.[105-108] By using polymeric

ligands that match one block of the BCP, the assembly of the NPs can be sequestered into that block by favorable Van der Waals interactions. For example, by using PS, P2VP, or a blend of the two ligands on the Au NPs, the assembly of the NPs were directed to the PS, P2VP, or the interface between the blocks, respectively.[109-112] Stronger interactions, such as electrostatic and hydrogen bonding, can be used to enhance the solubility of the NPs in the polymer matrix and increase the maximum weight fraction that can be incorporated before the NPs macrophase separate from the composite.[113,114] For neutral ligands, the size of the NPs relative to the domain size of the BCP have been shown to affect the location of the NP assembly.[115-117] A number of theoretical studies on this effect have been carried out by Balazs *et al*.[118-120] This work considered the effects of the NP size (d) vs. the BCP domain spacing (L). When $d/L < 0.2$, the particles favored assembly at the interface between microdomains, but when $d/L > 0.3$, the NPs assembled at the center of the favored domain. This is attributed to the larger deformation of the polymer chain necessary to incorporate larger particles at the interface.[118]

1.3.2 Supramolecule-Based Nanocomposites

Another method to tailor the polymer-NP interactions is to attach SMs to one block of a BCP that have favorable interactions with the ligands on the NPs. A wide variety of inorganic NP shapes (spheres, rods) and compositions (metallic, semiconducting, etc) have been aligned by supramolecules based on non-functional SMs.[3,121-128] When supramolecules are constructed from coil-coil BCPs, they adopt a coil-comblike structure, which increases the entropic penalty for deforming the polymer chain compared to coil-coil BCPs. This increased penalty can force the NPs to assemble into more localized regions within the comb block compared to coil-coil BCPs. Coassemblies of plasmonic and semiconducting NPs were achieved by this method, which could be useful for optical and electronic devices.[122] These supramolecular nanocomposites have also been used in the formation of luminescent microspheres by assembling CdSe NPs.[128] In addition, the thermal and light responsive, electronic, and dielectric properties of these nanocomposites can be tuned by changing the SM, as demonstrated in Figure 1.8.[3,126] The addition of a functional organic component to these systems has great promise to expand the possibilities of their future applications. However, the crystallinity and packing of these functional SMs can undoubtedly affect the assembly of NPs in supramolecules, which has not been thoroughly studied in these systems.

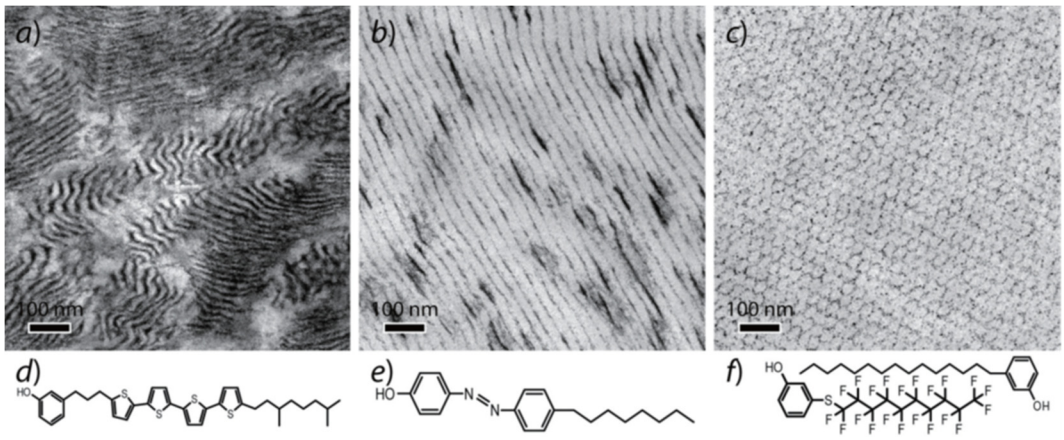

Figure 1.8. (a–c) TEM images of supramolecular nanocomposites based on PS-*b*-P4VP BCPs, functional SMs, and inorganic NPs. (d–f) The functional SMs used are pictured below each TEM image. Supramolecules based on an (a, d) OS, (b, e) a light responsive SM, and (c, f) a blend of a low-k fluorinated SM and alkyl SM were successfully used to direct the assembly of the NPs. Reprinted, with permission, from Thorkelsson *et al.* 10th IEEE International Conference on Nanotechnology **2010**, 51. © 2010 IEEE.

1.3.3 Nanocomposites with Highly Crystalline Organic Components

In the vast majority of the work on directed NP assemblies in BCP and supramolecular matrices, the organic component provides a structure framework but does not have inherent functionality. Nanocomposites that have a highly crystalline organic component, such as OSs and conjugated polymers, have the potential to combine the advantages of the functional organic and inorganic components. Much like conjugated polymer/OS blend devices, nanostructures of the conjugated polymer and NP components are typically formed by the spontaneous phase separation of the two materials in conjugated polymer/NP devices.[129] As previously mentioned, this technique does not yield nanostructures with controlled size and orientation, and this has motivated the investigation of better control methods. One method is to use BCPs where one block is a conjugated polymer and the other has favorable interactions with the NPs. For example, Chun Fang *et al*. demonstrated a triblock copolymer with a conjugated poly(fluorene) center block and polydimethylaminoethyl methacrylate blocks on each end that bonded to CdSe NPs to disperse the NPs in an organic semiconducting matrix.[130] Photoinduced charge transfer was present in the PL spectra, indicative of electron coupling between the organic and inorganic components. Maria *et al.* synthesized a BCP where one block contained hole-conducting tetraphenylbenzidine side groups, and the other block was P4VP, which had favorable binding interactions to n-type CdSe:Te NPs.[131] The NPs were successfully incorporated into the P4VP domains without disrupting the lamellar morphology of the BCP. Similarly, a rod-rod BCP, P3HT-*b*-polyselenophene, was used by Lianshan Li *et al*. to control the assembly of CdSe NPs by favorable interactions between the NPs and P3HT.[132]

Another technique to direct the assembly of NPs is to coassemble them with conjugated polymer nanowires. Hybrid nanowires were fabricated from coassemblies of P3HT nanowires and

CdSe dots through favorable interactions between the CdSe NPs and the sulfur atoms on P3HT,[133] and a similar method was utilized in hybrid PVs to achieve power conversion efficiencies (PCEs) of up to 4.1%.[134] Generally, the electronic coupling between the nanoparticles is enhanced by exchanging the long solubilizing ligands after synthesis with shorter ones, such as pyridine or alkanedithiols.[129,135] An alternative strategy is to directly attach OSs or conjugated polymers to NPs as ligands to improve the electronic coupling and interface between the organic and inorganic components.[136-138] By combining this with the hybrid nanowire assembly technique, P3HT/CdSe hybrid nanowires were fabricated by cocrystallization of P3HT with CdSe nanorods[139,140] and spheres[140] functionalized with P3HT ligands. Their assemblies are shown schematically and in TEM in Figure 1.9. The nanorods were well-oriented along the long axis of the P3HT nanowires and photoluminescence quenching of CdSe suggested that charge separation occurred between the two components.

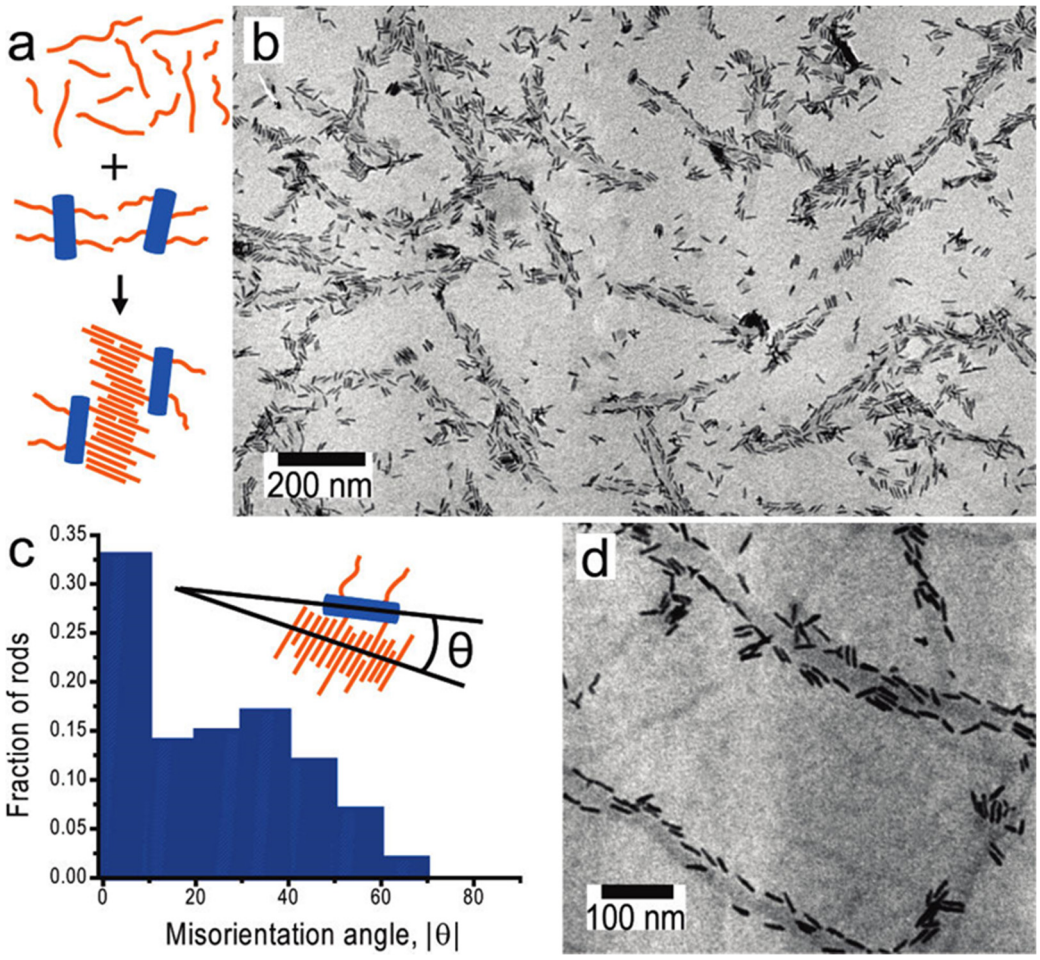

Figure 1.9. (a) Schematic of the cocrystallization of the free and CdSe nanorod-grafted P3HT chains. (b) TEM images of the P3HT nanowire and nanorod coassemblies. (c) Histogram of the orientation of the nanorods relative to the P3HT nanowire axis. Adapted with permission from Bokel *et al.* Macromolecules **2011**, 44, 1768. Copyright 2011 American Chemical Society.

§ 1.4 Conclusions and Outlook

Functional supramolecules have the potential to combine the advantages of functional SMs and polymers to yield processable, nanostructured, functional materials. These materials may prove useful for the fabrication of low-cost and flexible optical and electronic devices on their own and in blends with NPs. Although considerable progress has been made in using BCP templates to control the assembly of functional SMs and NPs separately, further work is necessary to improve our understanding of the coassembly and properties of these functional components. Improvements in devices will likely come from optimization of the morphology, interface between materials, electronic properties, optical properties, and electronic coupling between the SMs and NPs. Although there are still many challenges, recent progress suggests a bright future for these versatile materials.

One area where these composites could see potential use is organic-inorganic hybrid materials for PV devices with well-controlled nanostructures and interparticle ordering. Huynh *et al.* showed that the PCE can be enhanced by the use of anisotropic nanorods instead of spherical NPs due to the increased distance that charges could travel within a single particle before needing to "hop" to another.[129] Since the nanorods tend to adopt a non-ideal, parallel to the substrate orientation in these blends, conjugated polymers blended with tetrapods[141] and hyperbranched nanocrystals[142] have also been investigated to allow for enhanced charge transport perpendicular to the electrodes. Since BCP-based supramolecules can effectively organize semiconductor NPs into ordered arrays, this may provide a viable and effective means to control their alignment in electronic devices, such as PV devices.[3,121,124] However, in order to effectively interface organic and inorganic semiconductor materials into well-defined arrays, a greater understanding of the self-assembly of supramolecular nanocomposites based on highly crystalline functional SMs is required.

As discussed in Section 1.3.3, improvements in the charge mobility of NPs are generally achieved by exchanging the large, insulating ligands for shorter ones after film casting.[135] However, this leads to the disruption of the NP superlattices and cracking of the films. An alternative strategy is to use conducting ligands to lower the barrier to charge transport between particles.[136] This would allow for the use of ligands that are similar in size to the original, insulating ligand to reduce film cracking. Alternatively, the exchange process could be performed prior to film formation. To effectively achieve well-aligned, functional supramolecular nanocomposites with good electronic coupling among all components in the system, this surface chemistry would also need to be optimized. With the optimization of the coupling between NPs and between the inorganic and organic components, functional SM-based supramolecular nanocomposites that have well-aligned organic/inorganic assemblies with good electronic coupling could potentially be realized.

§ 1.5 General Approach and Synopsis of Subsequent Chapters

The work described in this dissertation investigates the bulk and thin film assembly as well as the electronic properties of OS-based supramolecules both alone and in blends with semiconducting NPs. It begins in Chapter 2 with preliminary experiments investigating the bulk

assembly, thin film assembly, and the electronic properties of supramolecules based on a highly crystalline, oligothiophene OS SM. Chapter 3 contains a more thorough investigation of the bulk assembly and thermally-responsive properties of these oligothiophene-based supramolecules, and Chapter 4 expands this investigation to a family of conjugated oligomer SMs. In Chapter 5, these functional supramolecules are coassembled with semiconducting nanoparticles, and their assemblies are compared to supramolecules based on less crystalline SMs.

Chapter 2
Bulk, Thin Film, and Electrical Characterization of Oligothiophene-Based Supramolecules

Small molecule organic semiconductors have many advantages over their polymer counterparts, including their high purity and well-defined electronic properties. However, to fabricate organic semiconductor-based devices using solution processing, it is requisite to eliminate dewetting to ensure film uniformity and desirable to assemble them into nanoscopic features with tailored macroscopic alignment without compromising their electronic properties. In this chapter, we introduce a modular supramolecular approach to address these concerns. A quaterthiophene organic semiconductor is attached to the side chains of 4-vinylpyridine groups of either a poly(4-vinylpyridine) homopolymer or a polystyrene-*block*-poly(4-vinylpyridine) block copolymer via non-covalent hydrogen-bonds to form supramolecular assemblies that act as p-type semiconductors in field-effect transistors. In thin films, the quaterthiophenes can be readily assembled into laterally oriented nanoscopic features, tens of nanometers in size. The supramolecules exhibited the same field-effect mobilities as that of the quaterthiophene alone (10^{-4} cm^2/Vs). Since the organic semiconductors can be readily substituted, this modular supramolecular approach is a viable method for the fabrication of functional, nanostructured organic semiconductor films using solution processing. This chapter was adapted with permission from Rancatore *et al. ACS Nano* **2010**, 4, 2721.

§ 2.1 Introduction

Small molecule organic semiconductors have many advantages over their polymer analogs, including their high purity and well-defined electronic properties.[1-4] They provide unique opportunities to fabricate low cost, high performance organic electronic devices such as organic photovoltaics (OPVs) or organic light-emitting diodes (OLEDs).[1,5-8] However, it can be challenging to solution process them into uniform films, due to dewetting and their strong tendency to crystallize.[2,9] When blending electron donors and acceptors, one major hurdle is to assemble each type of the functional small molecules into nanoscopic grains, tens of nanometers in size, in order to increase the donor/acceptor interfaces and optimize the efficiencies of the devices.[10-12] To effectively transport charges to the electrodes, these nanoscopic grains need to be macroscopically oriented normal to the substrate and the orientation and molecular packing of the organic semiconductors within each grain need to be tailored.[10]

A number of approaches have been explored to overcome these barriers. Uniform films of conjugated polymers can be readily cast using solution processing and are used extensively,[12-14] though they typically exhibit lower charge mobilities than their small molecule counterparts.[15] In blends of conjugated polymers and fullerene-based small molecule semiconductors, solution processed OPVs with power conversion efficiencies of ~5–6 % were achieved by kinetically trapping the phase separation of the active layer.[16-18] However, one of the main remaining concerns is to obtain ideal morphologies for OPVs with nanoscopic features with sizes comparable to typical exciton diffusion lengths that are vertically aligned to allow charges to reach electrodes.[16]

Block copolymers (BCPs) microphase separate and form well-defined arrays of microdomains, tens of nanometers in size. In thin films, BCP microdomains can be oriented normal to the surface by applying an external surface, electric, or solvent field.[19-21] Thin films of conjugated BCPs with microdomains oriented normal to the surface over macroscopic areas are of particular interest since they provide ideal morphologies for high efficiency, bulk heterojunction OPVs or OLEDs. However, such fine morphological control has proven far more difficult with

conjugated BCPs due to their poor solubility, low chain mobility, and high tendency to aggregate.[22-27] Electronic properties can also be built-in through the covalent attachment of conjugated molecules to the side chains of BCP blocks.[22,28] However, the generality is limited, since the synthesis of such BCPs is challenging, as monomers containing conjugated molecules have limited solubility. The covalently linked side-groups may also reduce the mobility of the polymer chain and restrain the molecular packing of the attached conjugated molecules required for high charge mobility.

BCP-based supramolecules can be constructed by attaching small molecules to pendant functionalities of a polymer chain via non-covalent interactions such as hydrogen bonding, electrostatic interactions or metal ligation.[29-33] By selective attachment of small molecules to one block of a coil-coil BCP, a coil-comblike supramolecule can be formed. These supramolecules phase separate into arrays of well-defined microdomains similar to those seen in BCPs alone and the small molecules order within the BCP microdomains. In thin films of BCP-based supramolecules, the macroscopic orientation of the supramolecular assemblies can be tailored.[34-38] By adjusting the loading of the small molecules, the BCP microdomains can be aligned perpendicular to the surface.[36,38] Within the BCP microdomains, lamellar assemblies from the comb block, several nanometers in size, are oriented parallel to the surface and small molecules are aligned perpendicular to the surface.[36,38] It has also been demonstrated that blends of inert polymers and organic semiconductors can be used to improve the solution processability the semiconductor.[39] The supramolecular approach provides a new avenue to improve the solution processability of organic semiconductors as well as to assemble them into nanoscopic structures in thin films. It circumvents some of the synthetic challenges inherent to the preparation of conjugated BCPs and enables the tailoring of electronic properties of the supramolecule without the need to synthesize new polymers.[33] Kinetically, the non-covalent linking of an organic semiconductor to a BCP block may preserve the chain mobility of the polymer necessary for ordered self-assembly during annealing, while constraining crystallization of the small molecule to within the microdomains. Nanostructured thin films were recently obtained in blends of regioregular poly(3-hexylthiophene)(P3HT)-*block*-poly(4-vinylpyridine)(P4VP) rod–coil block copolymers with [6,6]-phenyl-C61-butyric acid methyl ester (PCBM).[40] Favorable interactions between PCBM and P4VP sequestered the PCBM crystallization to within the BCP microdomains and led to bicontinuous electron donor/electron acceptor networks with high thermal stability.

§ 2.2 Results and Discussion

2.2.1 Small Molecule and Supramolecule Design

We can construct supramolecules by attaching oligothiophene organic semiconductors to the polymer side chains via hydrogen bonding and investigate critical parameters governing their assembly and electronic properties. 5’’’-(3,7-Dimethyloctyl)-5-(3-(3-hydroxyphenyl)propyl)-[2,2’;5’,2’’;5’’,2’’’] quaterthiophene, a semiconductor with a pendant phenol moiety, identified as “**4T**,” was designed to hydrogen bond to the 4-vinylpyridine units of a P4VP(46.7 kDa) homopolymer or a polystyrene(40 kDa)-*block*-poly(4-vinylpyridine)(5.6 kDa) (PS-*b*-P4VP) BCP, as shown in Figure 2.1. This small molecule was synthesized by Dr. Clayton Mauldin in a previously reported publication.[41] The resultant supramolecules are identified as P4VP(**4T**)$_r$ (in

which *r* denotes the ratio of **4T** to 4VP unit). A delicate balance between several competing processes including the BCP phase separation, macrophase separation of the BCP and semiconductor, and crystallization of the semiconductor is required in order to obtain the desired hierarchical assemblies. The favorable interaction between the phenolic end group of the semiconductor and the pyridyl side group of the BCP must balance the tendency of the quaterthiophene semiconductor to crystallize and phase separate from the BCP as a result of strong π-π interactions. The crystallization and melting temperatures of the semiconductor must also be tailored such that its amorphous state is accessible without completely breaking its non-covalent link to the BCP side groups. This will provide some mobility to the comb block while preserving the integrity of the hierarchical assemblies. A solution to this problem is to inhibit crystallization of the quaterthiophene through the use of a branched alkyl chain, while preserving its ability to transport charge.

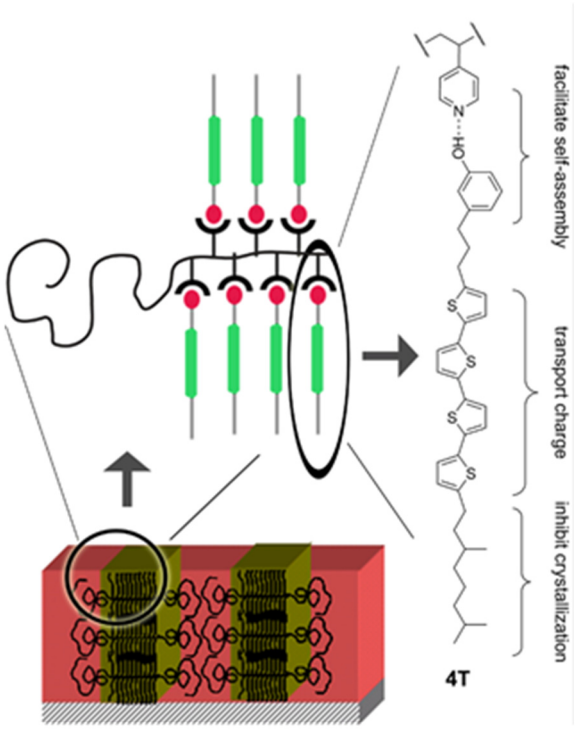

Figure 2.1. Phenol-pyridine hydrogen bonds between the **4T** molecules and the 4-vinylpyridine groups of a BCP. This forms a coil-comblike supramolecular architecture. The three-component design of the **4T** molecules allows for the tailoring of its properties for the desired application.

Differential scanning calorimetry (DSC) reveals a pair of endotherms at 126 and 142 °C upon heating and exotherms at 138 and 106 °C upon cooling (Figure 2.2). The H-bond between the phenol group and the 4VP is not significantly reduced until ~170-190 °C.[42] The melting temperature of **4T** is, therefore, within the temperature range necessary to access **4T**'s amorphous state without completely breaking its non-covalent link to the BCP side groups. This provides mobility to the P4VP(**4T**)$_r$ block while preserving the integrity of the hierarchical assemblies.

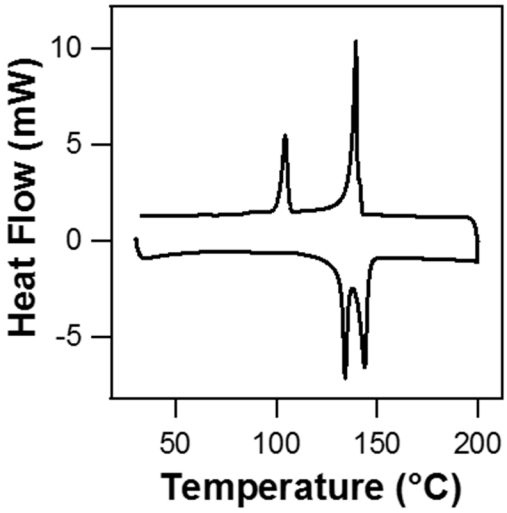

Figure 2.2. DSC thermogram of **4T**. Endotherms are observed at 126 and 142 °C upon heating, and exotherms are seen at 138 and 106 °C upon cooling.

2.2.2 Bulk Structural Characterization

Characterization of bulk samples was performed by small-angle X-ray scattering (SAXS) and transmission electron microscopy (TEM) to verify P4VP(**4T**)$_r$ self-assembly and determine the overall hierarchical structure. Hydrogen bonding **4T** to a BCP, PS-*b*-P4VP, results in a BCP-based supramolecule, PS-*b*-P4VP(**4T**)$_r$. The synergistic co-assembly of the BCP and **4T** may lead to hierarchical assemblies that may satisfy many morphological requirements for high efficiency OPVs and OLEDs. However, most of the previous studies on BCP-based supramolecules have focused on small molecules which have a much weaker tendency to aggregate in comparison to **4T**. For highly crystalline organic semiconductors, such as **4T**, the crystallization may induce macrophase separation. A delicate balance between the BCP self-assembly and crystallization of the semiconductor is required to obtain the desired hierarchical assemblies. Thus, we first investigated the assembly of PS-*b*-P4VP(**4T**)$_r$ in bulk, which provided guidance to manipulate **4T** assemblies in thin films.

Figure 2.3a, b show the SAXS profile and TEM image of PS-*b*-P4VP(**4T**)$_1$ annealed at 110ºC. This annealing temperature was selected since the hydrogen bonding between **4T** and 4VP becomes unstable at temperatures above 110ºC.[42] The presence of q, $2q^*$, and $3q^*$ peaks in the SAXS profile confirms the formation of lamellae-within-lamellae hierarchical assemblies, where the BCP forms a lamellar morphology with a periodicity of ~33.7 nm and the P4VP(**4T**)$_1$ comb block forms lamellae with a periodicity of ~6.3 nm. The TEM image shows that the **4T**s are completely incorporated within the BCP lamellae. In addition to these lamellae, irregularly-sized rectangular microdomains are seen, which may be caused by an irregular distribution of **4T** in these regions or "T"-junction defects.[43] Once the **4T** crystallizes, the P4VP(**4T**)$_1$ comb block stiffens. Packing the P4VP(**4T**)$_r$ block into a curved morphology is not energetically favorable because it requires the rigid lamellae to spread apart. Despite the energetic cost of the sharp

curvatures, the π-π interactions between the comb blocks are strong enough to stabilize the morphologies observed in this image. However, the weight fraction of **4T** in PS-*b*-P4VP(**4T**)$_1$ is only 42 %. It is likely that the **4T** fraction needs to be increased to ensure charge injection and transport.

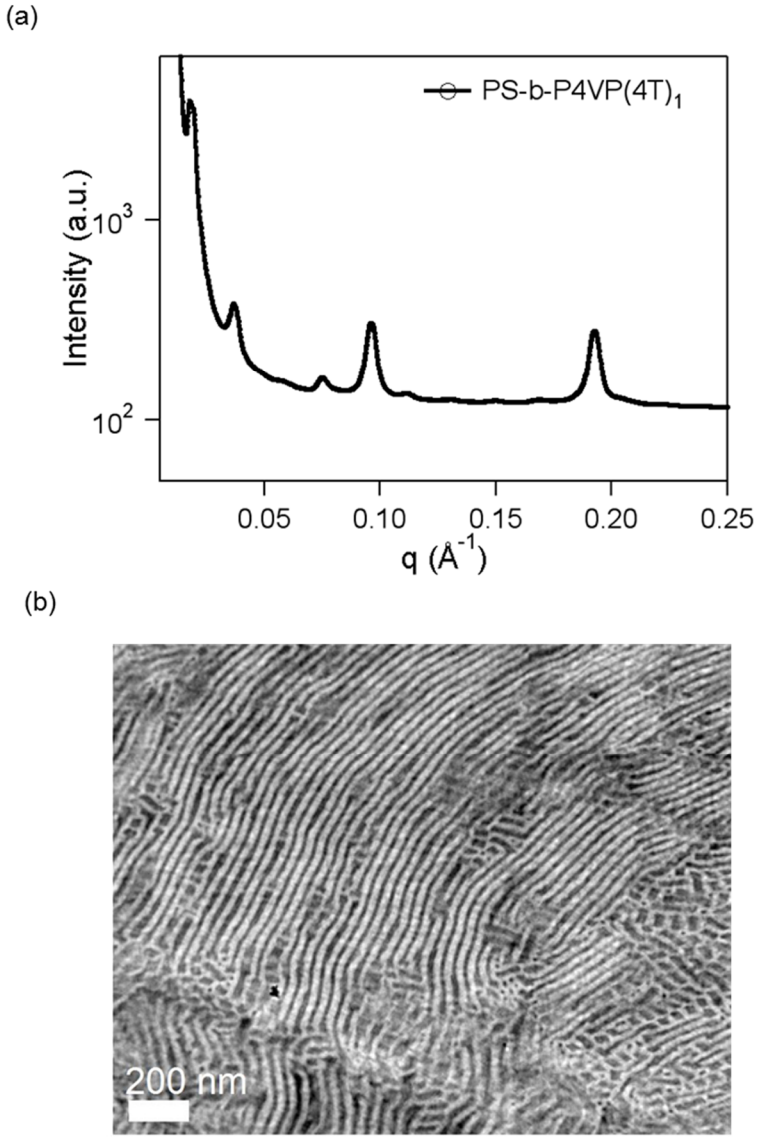

Figure 2.3. (a) SAXS profile and (b) TEM image of PS-*b*-P4VP(**4T**)$_1$ annealed at 110 ºC, showing a lamellae-within-lamellae morphology.

After increasing *r* to 1.5 and annealing at 110ºC, the SAXS profile (Figure 2.4a) indicates the presence of nanostructures resulting from BCP microphase separation in addition to the packing of small molecules that are incorporated (6.3 nm) and not incorporated into the supramolecule (5.7 nm). Figure 2.4b shows a representative TEM image and no large grains of

macrophase separated **4T** are observed. However, a mixture of two morphologies is present, indicating a non-uniform distribution of **4T**. On the right side, P4VP(**4T**) microdomains appear to pack into hexagonal arrays embedded in the PS matrix. In the lamellar morphology region on the left hand side of the image, many defects are seen and the ordering is poor. In many regions, as indicated by the circle in the inset, two BCP microdomains are connected with lamellae with a much smaller periodicity of ~6 nm. It is highly likely that these lamellae are assemblies of **4T** alone and correspond to the diffraction peak at $q \sim 0.011$ Å^{-1} (5.7 nm). At $r > 1$, the excess amount of **4T** crystallizes during the drying process, leading to an inhomogeneous distribution of **4T**. At 110ºC, below the melting temperature of **4T**, the mobility of PS-*b*-P4VP(**4T**)$_r$ is insufficient to achieve uniform supramolecular assemblies. Mixed morphologies have not been observed previously in BCP-based supramolecules and can be attributed to **4T**'s strong tendency to crystallize.

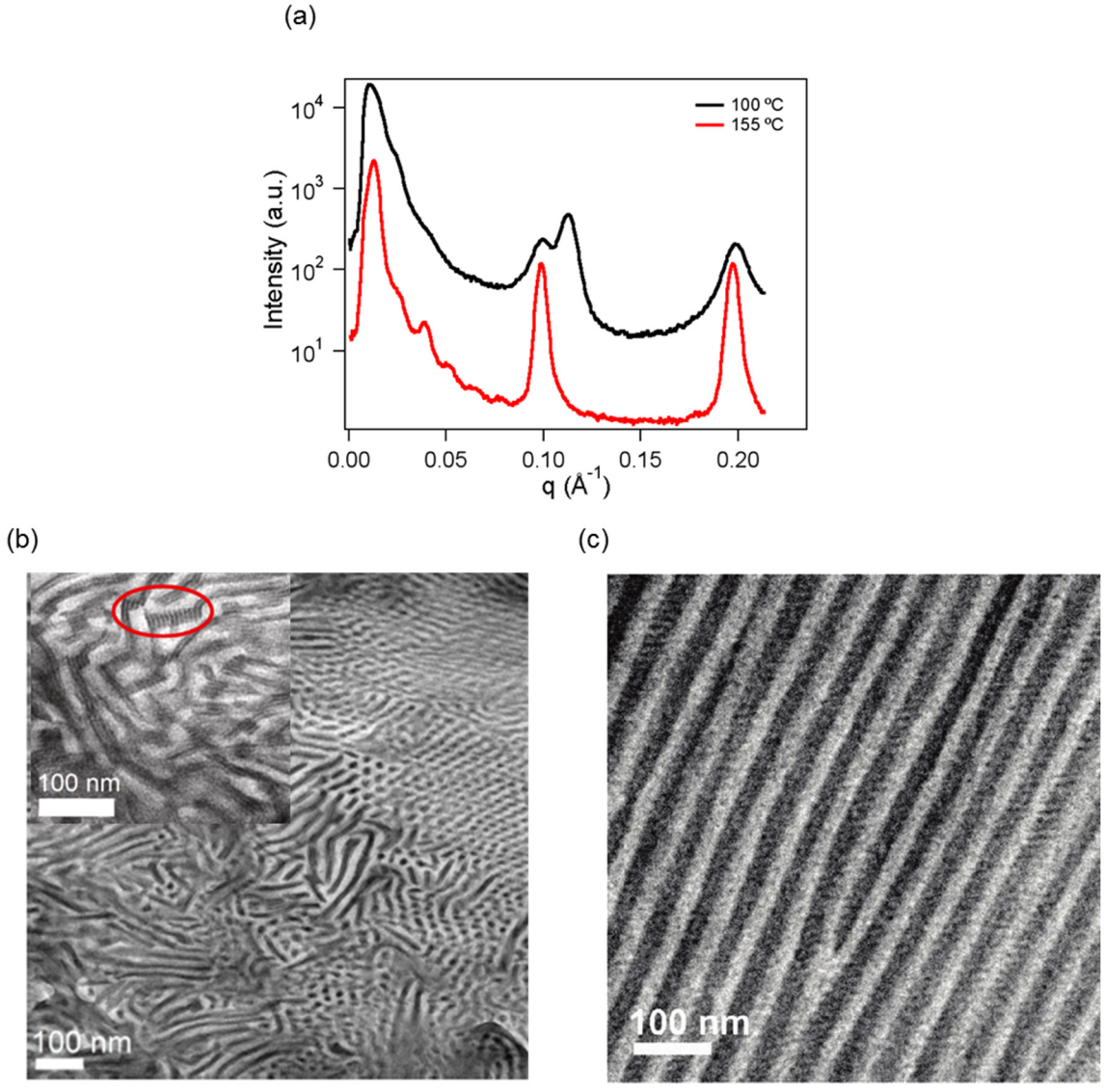

Figure 2.4. (a) SAXS profiles of PS-*b*-P4VP(**4T**)$_{1.5}$ annealed at 110 ºC and 155 ºC. The TEM images are shown in (b) and (c), respectively. For PS-*b*-P4VP(**4T**)$_{1.5}$ annealed at 110 ºC, mixed

morphologies are observed and **4T** organizes into lamellae, ~ 6 nm in periodicity, bridging the BCP lamellae, as seen in the zoom-in TEM image in the in-set of (b).

By further increasing the thermal annealing temperature to 155 ºC, above the melting temperature of **4T**, a uniform lamellae-within-lamellae morphology is observed for PS-*b*-P4VP(**4T**)$_{1.5}$, as shown in Figure 2.4c. The SAXS profile in Figure 2.4a shows a complete incorporation of **4T** into the supramolecules, which increases the BCP periodicity to ~52 nm. Within the BCP lamellar microdomains, the P4VP(**4T**)$_{1.5}$ comb blocks assemble into lamellae, ~6 nm in periodicity, and can be clearly seen in TEM. Although a significant fraction of hydrogen bonds are broken at 155 ºC and $r > 1$, the favorable interaction between the phenolic end group of the semiconductor and the pyridyl side group of the BCP and strong π-π interactions between the oligothiophenes provide sufficient driving force to sequester the **4T**s into the BCP microdomains and prevent macrophase separation.

2.2.3 Thin Film Structural Characterization

The orientation and structural ordering of the domains containing the organic semiconductors in thin films is critical to the performance of these supramolecules in electronic devices. Consequently, the hierarchical assembly of P4VP(**4T**)$_1$ and PS-*b*-P4VP(**4T**)$_{1.5}$ were studied in thin films using grazing-incidence small-angle X-ray scattering (GISAXS). Thin films of P4VP(**4T**)$_1$ and PS-*b*-P4VP(**4T**)$_{1.5}$, ~50–60 nm in thickness, were spin-casted onto untreated silicon wafers and subsequently solvent and thermally annealed. The incidence angles (α_{in}) are in the range of 0.15–0.20^o, where the incident X-rays penetrate the whole film and probe structural information throughout the entire thickness of the film. Figure 2.5a shows the GISAXS pattern of a solvent annealed P4VP(**4T**)$_1$ film, and the q_z scan is shown in Figure 2.5d. Diffraction spots, instead of rings, are seen in the q_z direction, indicating that the P4VP(**4T**)$_1$ forms lamellar domains, ~6.3 nm in periodicity, mainly oriented parallel to the substrate. The spreading of the diffraction spots suggests that a small fraction of P4VP(**4T**)$_1$ lamellae are tilted from the parallel orientation. Thermal annealing at 110ºC for 1 h enhances the P4VP(**4T**)$_1$ ordering, sharpens the diffraction peaks, and reduces the periodicity to 5.7 nm, as seen in the GISAXS pattern and q_z scans shown in Figure 2.5c, d. Since the phenol-4VP H-bond has been found to be stable at 110°C, and there were no observed decreases in film thicknesses, we speculate the periodicity of P4VP(**4T**)$_r$ reduced upon heating due to changes in packing of the supramolecules.[42] This macroscopic alignment of **4T**, as schematically shown in Figure 2.5b, is similar to that seen in thin films of oligothiophenes alone.[44]

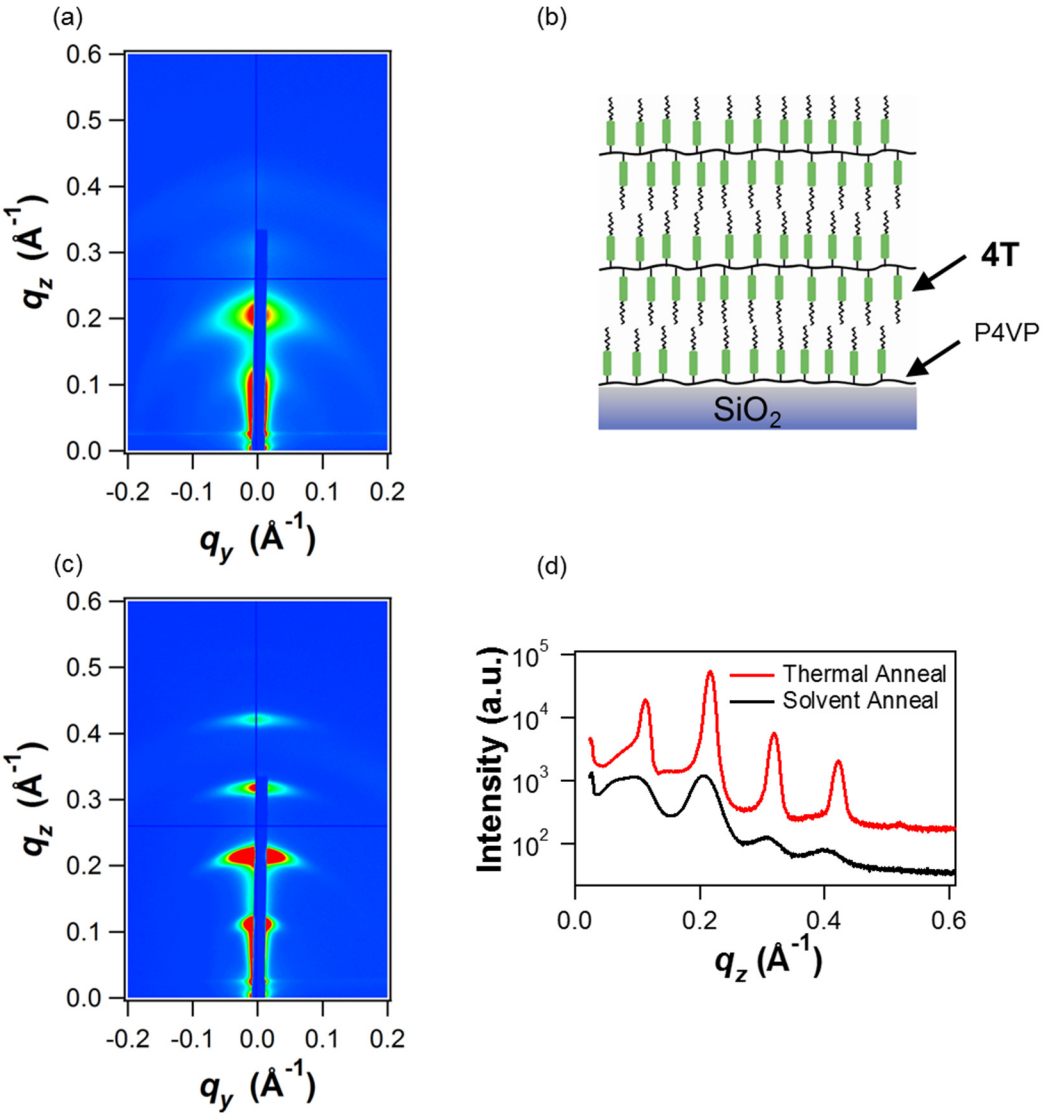

Figure 2.5. (a, c) GISAXS patterns of a ~60 nm P4VP(**4T**)$_1$ thin film at an incident angle of 0.15° after (a) solvent annealing for 36 h and (c) thermal annealing for 1 h at 100 – 110 °C under N_2. (d) The q_z scans at q_y = 0.017 Å^{-1} show that the (black) solvent and (red) thermally annealed P4VP(**4T**)$_1$ lamellae, ~6.5 nm and ~5.6 nm in periodicity, respectively, are oriented parallel to the surface, as schematically shown in (b). Thermal annealing enhances the P4VP(**4T**)$_1$ ordering and sharpens the diffraction peaks.

The ideal morphology for OPVs and OLEDs requires an alignment of BCP microdomains in thin films normal to the film surface. Upon attaching **4T** to the P4VP side chains, the BCP microdomain orientation depends on the interactions between each component with the underlying substrate. As shown in Figure 2.5b, favorable interactions between P4VP with the Si substrate orient the P4VP(**4T**)$_1$ lamellae parallel to the surface. For PS-*b*-P4VP(**4T**)$_{1.5}$ supramolecules, the parallel orientation of P4VP(**4T**)$_1$ lamellae may overcome the non-favorable interactions between

the PS block with the underlying substrate and cause the BCP microdomains to orient normal to the surface, as shown in Figure 2.1.

Figure 2.6a shows the GISAXS pattern of a ~50 nm PS-*b*-P4VP(**4T**)$_{1.5}$ thin film at $\alpha_{in} = 0.20^{o}$ after solvent annealing. Features in both q_z and q_y directions are observed. The q_y scan in Figure 2.6d only shows a broad diffraction peak at $q_y \sim 0.017$ Å^{-1}, corresponding to the lateral microphase separation of PS-*b*-P4VP(**4T**)$_{1.5}$ with a periodicity of ~37 nm. The solvent annealed PS-*b*-P4VP(**4T**)$_{1.5}$ film is microphase separated with fairly poor lateral order. However, only diffraction spots, instead of rings, were seen in the GISAXS pattern, indicating the BCP microdomains are mainly oriented normal to the substrate. Grazing-incidence wide-angle X-ray scattering (GIWAXS) was used to investigate the ordering of PS-*b*-P4VP(**4T**)$_{1.5}$ at much smaller length scales, as seen in Figure 2.6e. In the high q_y region, diffuse scattering originating from the molecular packing of **4T** can be seen around $q_y \sim 1.3–1.5$ Å^{-1}.[44] The crystallinity of **4T** in thin films of PS-*b*-P4VP(**4T**)$_{1.5}$ is somewhat low. However, there are a series of diffraction peaks along the q_z direction, originating from the P4VP(**4T**)$_r$ lamellae with a periodicity of ~6.3 nm oriented parallel to the surface, similar to the schematic in Figure 2.5b. The atomic force microscopy (AFM) image of a solvent-annealed PS-*b*-P4VP(**4T**)$_{1.5}$ thin film shows some degree of nanostructured ordering, but it is not well-defined (Figure 2.7). Thermal annealing at 110˚C for 1 h improves the hierarchical ordering of PS-*b*-P4VP(**4T**)$_{1.5}$ significantly and results in a sharpening of peaks in the q_y and q_z directions, shown in Figure 2.6b–d. The peaks in the q_y scan indicate that thermally annealed PS-*b*-P4VP(**4T**)$_{1.5}$ thin films form BCP lamellae oriented normal to the film surface with a periodicity of ~52 nm and suggests a complete incorporation of **4T** into the BCP lamellae. Thus, thermally annealed thin films of PS-*b*-P4VP(**4T**)$_{1.5}$ form hierarchical structures similar to those shown schematically in Figure 2.1.

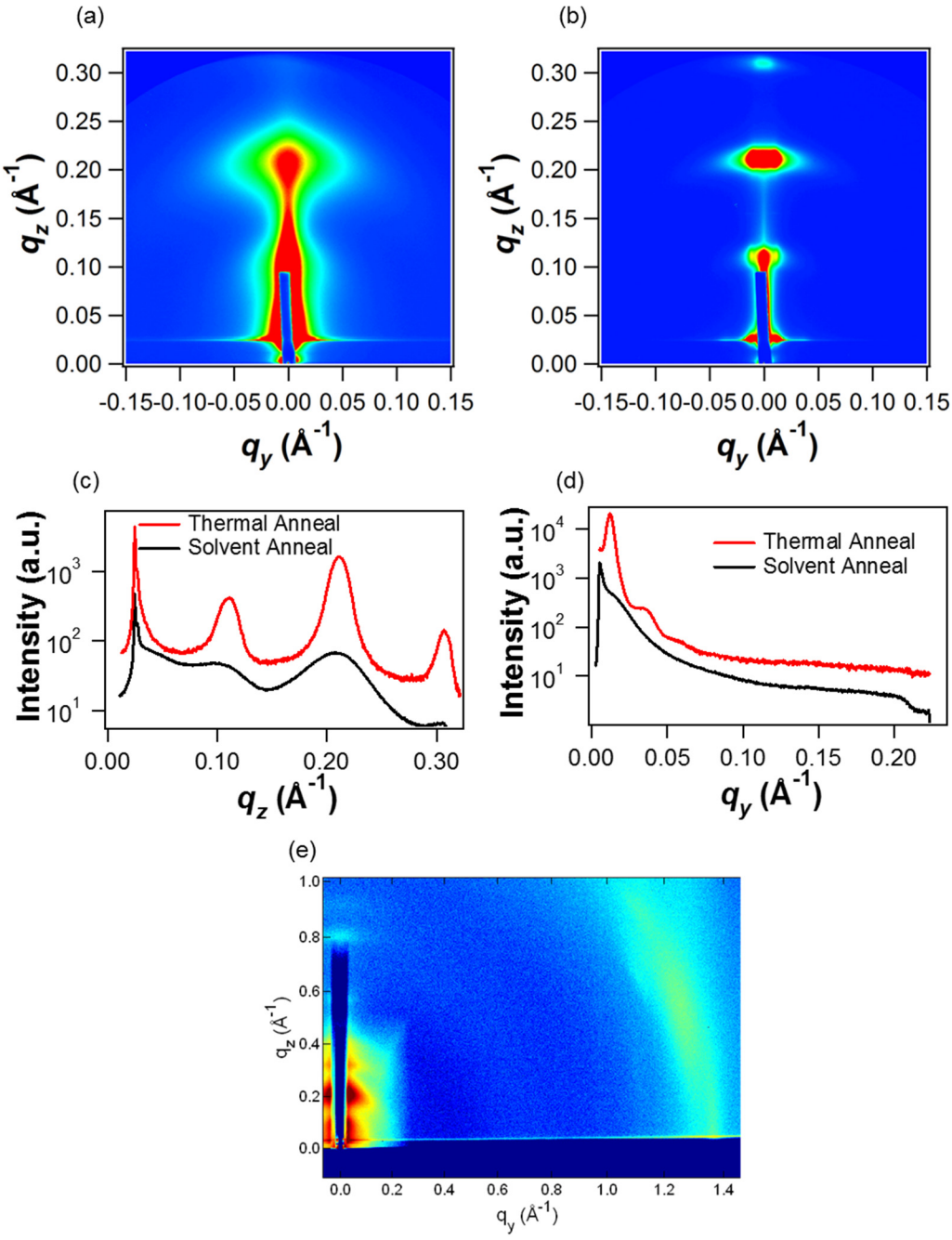

Figure 2.6. (a, b) The GISAXS and (e) GIWAXS patterns of a ~50 nm PS-*b*-P4VP(**4T**)$_{1.5}$ thin film after (a) solvent annealing for 24 h and (b) thermal annealing for an hour at 100–110 °C under N_2 at incident angles of 0.19 - 0.2°. (c) The q_z scans at q_y = 0.018 Å^{-1}, show the solvent and thermally annealed P4VP(**4T**)$_r$ lamellae, ~6.2–6.6 nm and ~5.7 nm in periodicity, respectively, are oriented parallel to the surface. (d) The q_y scans at q_z = 0.025 Å^{-1}, show the solvent and thermally annealed BCP lamellae, ~30–37 nm and ~52 nm in periodicity, respectively, are oriented perpendicular to the surface.

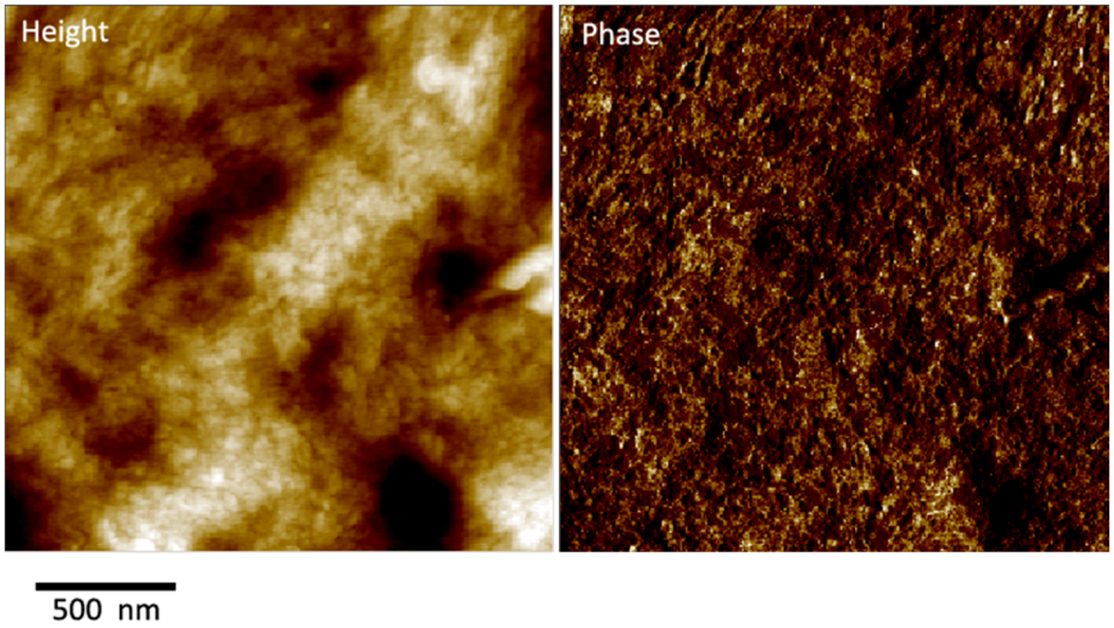

Figure 2.7. AFM images of a ~50 nm solvent-annealed PS-*b*-P4VP(**4T**)$_{1.5}$ film.

Thus, solvent annealed PS-*b*-P4VP(**4T**)$_{1.5}$ do not form a well ordered lamellae-within-lamellae morphology in thin films as previously found with other BCP-based supramolecules. We speculate that after solvent annealing, PS-*b*-P4VP(**4T**)$_{1.5}$ may form morphologies similar to those shown in Figure 2.4b, where a significant fraction of **4T**s organize into lamellae bridging the BCP lamellae in different grains to provide a pathway to transport charges between P4VP(**4T**)$_r$ lamellae. Upon thermal annealing, **4T**s are incorporated within P4VP(**4T**)$_r$ microdomains, which results in an increase in the BCP periodicity. This improves macroscopic alignment of the BCP lamellae normal to the surface, however, very likely removes this electronic pathway and reduces charge mobility.[45]

2.2.4 Electrical Characterization

Analysis of OFET data enables the calculation of charge mobility for the organic semiconductor and provides a qualitative evaluation of the level of dopants and charge traps introduced into the films during the process of supramolecule formation. In order to demonstrate the electronic functionality of our supramolecular structures, p-channel OFETs were constructed with 1000 Å SiO_2 as the gate dielectric and either **4T**, P4VP(**4T**)$_1$, PS-*b*-P4VP(**4T**)$_1$ or PS-*b*-P4VP(**4T**)$_{1.5}$ as the active layer. Devices were fabricated in top-contact/bottom-gate geometry (see Figure 2.8) in order to verify that these supramolecular films are semiconducting throughout their entire thickness, which is critical for fabricating OPVs.[39] OFET devices were tested by Dr. Clayton Mauldin. Saturation mobilities (μ) were calculated using eq. 2.1, where g_m = transconductance, I_D = drain electrode current, C_{ox} = insulator capacitance, W = electrode width, and L = channel length.

$$\mu = g_m^2 / 2I_D C_{ox}(W/L) \qquad \text{(eq. 2.1)}$$

Although the **4T** molecule is highly soluble in numerous organic solvents, uniform films cannot be formed by spin coating. In addition, **4T** dewets the Si substrate upon thermal annealing. These factors significantly decrease the OFET yield for **4T** devices. However, uniform films of controlled thicknesses can be readily cast from the P4VP(**4T**)$_1$ and PS-*b*-P4VP(**4T**)$_r$ (r = 1, 1.5) supramolecules.

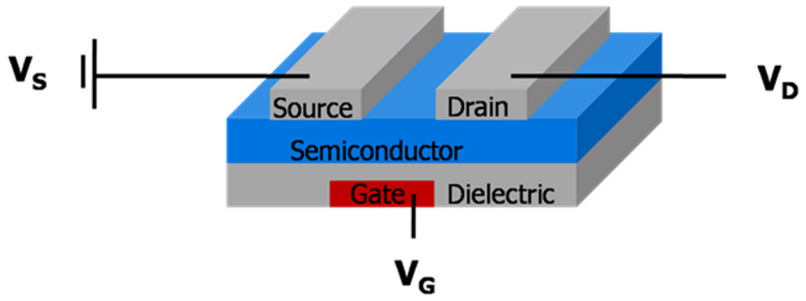

Figure 2.8. Schematic of an OFET in top-contact/bottom-gate geometry.

Unannealed films of **4T** fail to provide ideal transfer curves as evidenced by the non-linear plot of $|I_D|^{1/2}$ (Figure 2.9a). While the devices do exhibit gate-modulated conductivity, this non-ideal behavior makes it impossible to calculate the charge mobility in these films. Thermal annealing of the **4T** films at 135 °C for 10 minutes result in a significant increase in saturation currents measured in OFETs and produce linear plots of $|I_D|^{1/2}$ in transfer IV curves and charge mobilities of 10^{-4} cm^2/Vs. Low off-currents, the minimum I_D measured in the devices, suggest a low level of doping in the pristine small molecule films.[2] A representative transfer plot of an annealed **4T** device is shown in Figure 2.9b. The charge mobilities of **4T** are comparable to or higher than many conjugated polymers that have been used in OLEDs[42] and OPVs.[24,46-48] Furthermore, devices exhibited a low turn-on voltage, which suggests a low barrier to mobile charge injection.

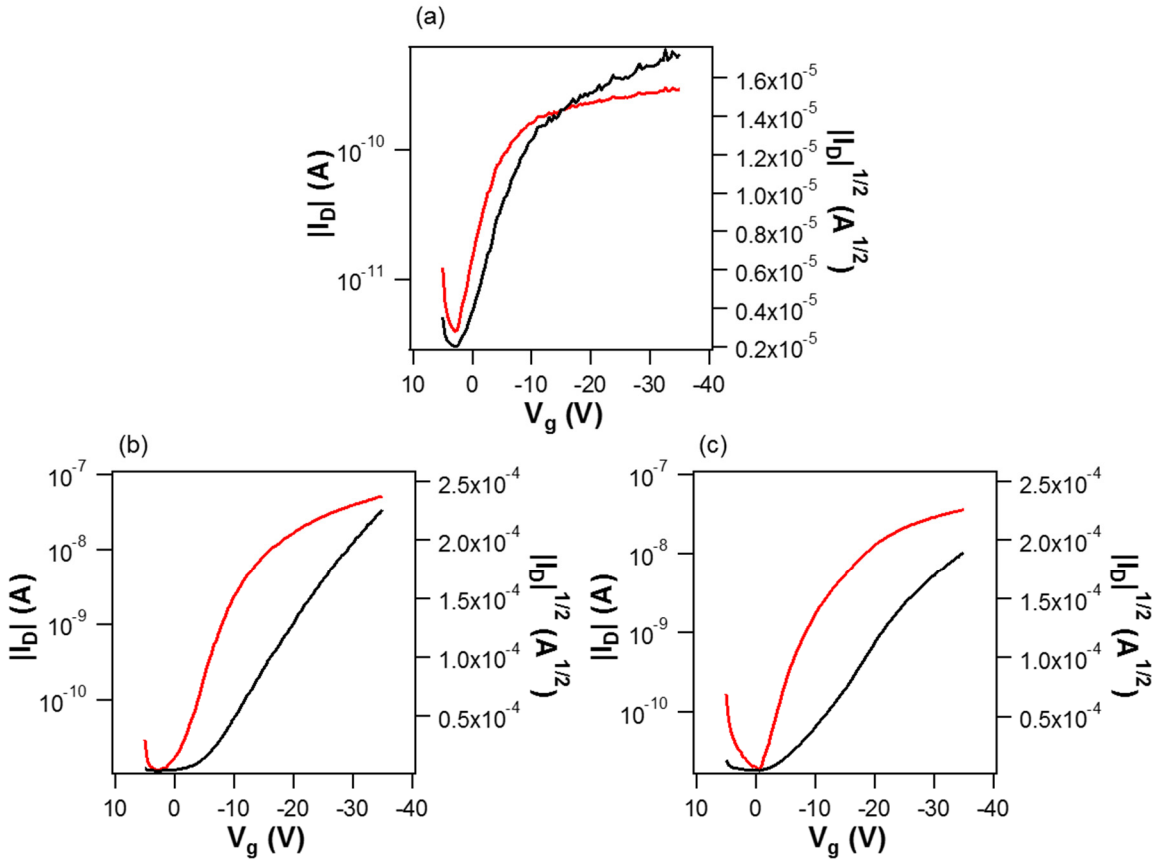

Figure 2.9. Transfer IV plots of (a, b) **4T** and (c) P4VP(**4T**)$_1$ devices. (a) A plot of |ID| (red) and $|ID|^{1/2}$ (black) for an unannealed **4T** device with W = 400 μm and L = 10 μm. (b) A plot for a thermally annealed **4T** device with W = 400 μm and L = 10 μm. (c) A solvent annealed P4VP(**4T**)$_1$ device with W = 400 μm and L = 20 μm. The charge mobilities for thermally annealed **4T** and solvent annealed P4VP(**4T**)$_1$ devices are calculated to be 10^{-4} cm^2/Vs, and the on/off ratio of the devices are 10^3.

Having validated **4T** as an organic semiconductor in p-channel OFETs, we studied the charge transporting capabilities of the P4VP(**4T**)$_1$ supramolecule. While the **4T** films were observed to dewet the device substrates, decreasing the OFET device yield, uniform films of controlled thicknesses can be readily cast from P4VP(**4T**)$_1$ solutions. High quality thin films can also be processed for $r > 1$. Thin films of P4VP(**4T**)$_1$, ~60 nm in thickness, were solvent annealed under chloroform vapor for 24 h to improve the ordering of P4VP(**4T**)$_1$. As shown in a representative transfer IV plot in Figure 2.9c, the solvent annealed P4VP(**4T**)$_1$ films function as the active layer in OFETs with charge mobilities of 10^{-4} cm^2/Vs. The saturation current levels are similar to those obtained in annealed pristine **4T** OFETs, and off-currents remain low. Consecutive scans of V_G show bias stress effects (BSEs) in the devices, as seen in Figure 2.10. Charge traps or defect formation in OFET device channels are thought to produce BSEs.[49-52] Since these effects are absent in **4T** OFETs, the defect formation or charge trapping cannot be attributed to the structure of **4T**. It is unclear if the chemistry of P4VP leads to defect formation in active device

channels or if the P4VP(**4T**)$_1$ films simply contain more trap sites due to the greater thickness of the films obtained from the supramolecule.[52] Since P4VP preferentially interacts with SiO_2 and the **4T** molecule dewets the silicon substrate, the higher affinity of P4VP to silicon oxide layer precludes **4T** enrichment at the P4VP(**4T**)$_1$/SiO_2 interface.[34] Thus, the OFETs measure the mobility of charge in a thin layer (~5-10 nm) of the P4VP(**4T**)$_1$ next to the SiO_2 dielectric, not phase-separated **4T**.[53,54]

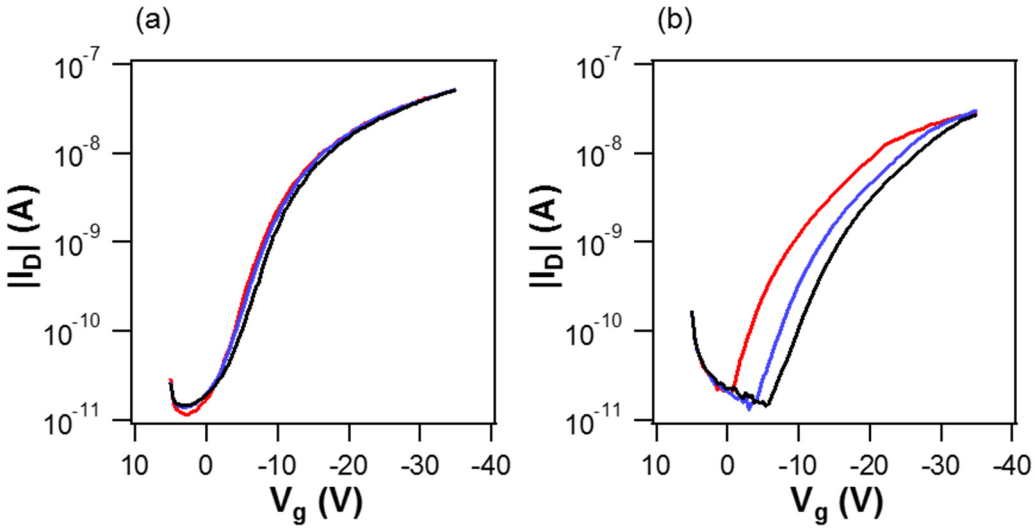

Figure 2.10. A set of three consecutive (red, blue, then black) scans of thermally annealed (a) **4T** and (b) P4VP(**4T**)$_1$ OFETs. Consecutive scanning of the **4T** device gives nearly identical IV curves, while bias stress effects are observed in the P4VP(**4T**)$_1$ device.

Since a bottom-gate and top-contact test structure requires a film with semiconducting properties through its entire thickness, the OFET results clearly demonstrate that by hydrogen bonding **4T** to P4VP, P4VP(**4T**)$_1$ thin films transport charges in both the lateral and vertical directions. Constructing P4VP(**4T**)$_1$ supramolecules does not sacrifice the charge mobility of **4T**, yet enhances its solution processability into uniform films and control over its spatial arrangement.

Devices were prepared with PS-*b*-P4VP(**4T**)$_1$ films to determine if the domains of P4VP(**4T**)$_1$ within the BCP film could provide conductive pathways in OFET channels (Figure 2.11). These devices yield saturation currents an order of magnitude lower than **4T** and P4VP(**4T**)$_1$ films. The threshold voltages of the devices are generally shifted to slightly more negative values, which suggest that restriction of **4T** into the block copolymer lamellae hampers the injection of mobile charge carriers. However, the weight percent of **4T** in these films is significantly lower (42 %) compared to P4VP homopolymer films (85%).

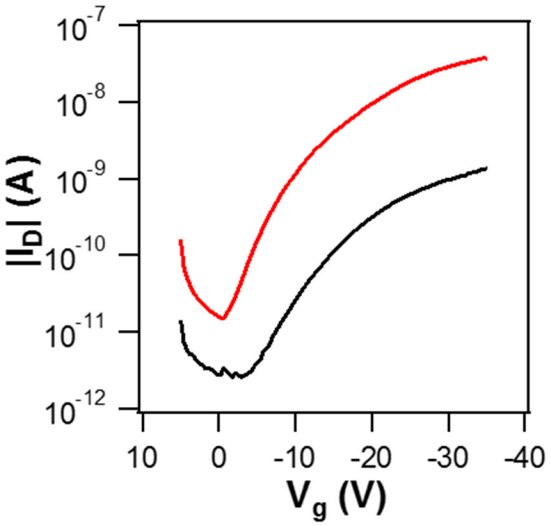

Figure 2.11. A comparison of IV plots for PS-*b*-P4VP(4T)$_r$ OFETs where r = 1 (black) and r = 1.5 (red). The devices are the same geometry with W = 200 μm and L = 10 μm. The charge mobility was calculated to be 10^{-6} and 10^{-4} cm^2/Vs for r = 1 and 1.5, respectively. The on/off ratio for PS-*b*-P4VP(4T)$_{1.5}$ OFETs was 10^3.

Increasing the ratio of **4T** to 4VP enhances the **4T** fraction in the film, the backbone stiffness of the P4VP block, and possibly the comb block packing. The TEM image in Figure 2.4b shows that the **4T** lamellae bridge the BCP lamellae in different grains and potentially improve the electronic connectivity between the BCP lamellae in PS-*b*-P4VP(**4T**)$_{1.5}$ films. To determine if this effect would increase charge mobility in the supramolecular films, PS-*b*-P4VP(**4T**)$_{1.5}$ OFETs were fabricated as described above. A comparative plot of saturation currents in PS-*b*-P4VP(**4T**)$_r$ OFETs, where r = 1 and 1.5, is shown in Figure 2.11. The saturation currents in these devices increase by an order of magnitude relative to analogous PS-*b*-P4VP(**4T**)$_1$ OFETs, and the charge mobility of PS-*b*-P4VP(**4T**)$_{1.5}$ is calculated to be 10^{-4} cm^2/Vs, comparable to **4T** and P4VP(**4T**)$_1$. The OFET results suggest that there is a conductive pathway normal to the surface through the P4VP(**4T**)$_r$ microdomains.

§ 2.3 Conclusion

We have demonstrated a molecular design strategy involving the non-covalent linking of organic semiconductors to a polymer chain which greatly improves the solution processability, ordering, and macroscopic alignment of the semiconductor molecules without hindering the charge mobility in OFET devices. In thin films of PS-*b*-P4VP(**4T**)$_{1.5}$, the BCP microdomains orient normal to the substrate and form a lamellae-within-lamellae supramolecular structure. Within the lamellar BCP microdomains, P4VP(**4T**)$_r$ forms lamellae oriented parallel to the substrate. In addition, this supramolecular comb block transports charge in OFET channels, thus these films act as nanostructured semiconductor composites. Although effectively measuring the mobility of

charge in a thin layer (~5-10 nm) of the organic semiconductor next to the SiO_2 dielectric instead of the bulk property,[53,54] the top-contact, bottom-gated OFET experiments demonstrate the functionality of the supramolecular film assemblies throughout their entire thickness. Additionally, the charge mobilities of **4T**, P4VP(**4T**)$_1$, and PS-*b*-P4VP(**4T**)$_{1.5}$ measured in OFETs are comparable to organic semiconductors that have been used in OLEDs[55] and OPVs.[24,46] Furthermore, this mobility value is greater than that measured in some conjugated polymers, such as poly(*p*-phenylene vinylene), where nanoscopic assembly is challenging.[47,48] The presented supramolecular approach and design principles should be applicable to other organic semiconductors, thus providing a versatile method to access films with spatial and orientational control of the semiconductor, which is otherwise difficult. Furthermore, recent studies have shown that BCP-based supramolecules can effectively organize semiconductor nanoparticles into ordered arrays, which provides a viable and effective means to incorporate electron donor or acceptors as needed.[56] This, in conjunction with the use of other small molecules with improved optical and electronic properties, may potentially lead to the fabrication of high performance OPVs and OLEDs.

§ 2.4 Experimental Section

2.4.1 Materials

P4VP(46,700) (PDI=1.14) and PS(40,000)-*b*-P4VP(5,600) (PDI=1.09), were purchased from Polymer Source, Inc. Chloroform was purchased from Fisher and filtered through basic alumina. All other chemicals were purchased from Aldrich and used as received. The synthetic procedure to prepare **4T** is described in detail in a previous publication.[41]

2.4.2 Sample Preparation

The PS-*b*-P4VP or the P4VP was first dissolved in chloroform to form 1% - 2% (wt/v) stock solutions. The desired amount of **4T** was dissolved in chloroform. The polymer solution was then added to the **4T** solution, followed by stirring overnight. Thin films were prepared by spin-coating the mixed solutions onto silicon wafers at spinning speeds between 1000 and 4000 rpm. **4T** is light and oxygen sensitive and so cautions were paid to avoid light exposure during the sample preparation process. Sample thicknesses were measured using a FilmetricsTM F20 interferometer. For solvent annealing, thin films were placed together with a beaker of 40 ml chloroform at 22 °C inside an inverted dish (170 Dia. x 90 H mm) on which a ~2 kilogram weight was loaded for 24–48 hours. For thermal annealing, samples were wrapped in aluminum foil inside an inverted dish and placed in an oven under a nitrogen atmosphere at 100 – 110°C for 1 h.

2.4.3 Differential Scanning Calorimetry (DSC)

4T was heated and cooled from 0 °C – 200 °C – 0 °C at a rate of 10 °C/min. DSC thermograms were collected on a TA Q200 DSC with an RCS 40 refrigeration unit.

2.4.4 Small-Angle X-ray Scattering (SAXS) and Grazing-Incidence SAXS (GISAXS)

Bulk samples were prepared by casting and drying the supramolecule solutions in PTFE beakers inside an inverted dish and allowing the solvent to evaporate over 48 hours. Samples were then thermally annealed at ~100 – 110 °C or 155°C under vacuum overnight and then slowly cooled to room temperature. The SAXS data were collected on beamline 7.3.3 in the Advanced Light Source (ALS) at the Lawrence Berkeley National Laboratory. X-rays, with a wavelength of 1.240 Å (10KeV) were used, and the scattering spectra were collected on an ADSC Quantum 4u CCD detector with an active area of 188 mm by 188 mm (2304 by 2304 pixels) and a dynamic range of 16 bit. The scattering profiles, after a 20 s collection time, were obtained by integrating the 2-D scattering pattern. GISAXS measurements were made on beamline 7.3.3 in ALS and beamline 8-ID-E at the Advanced Photon Source (APS) at the Argonne National Laboratory. X-ray wavelengths of 1.240 Å (ALS) and 1.687 Å (APS) were used. The scattering profiles were collected on an ADSC Quantum 4u CCD detector at ALS and a Mar-CCD at APS. Line-averaged intensities are reported as I vs. q, where $q = (4\pi/\lambda)*\sin(\theta/2)$, λ is the wavelength of incident x-rays and θ is the scattering angle.

2.4.5 Transmission Electron Microscopy (TEM)

The same samples used for SAXS was embedded in resin and cured at 60 °C overnight before being microtomed for TEM imaging. The thin sections of PS(40,000)-*b*-P4VP(5,600)(**4T**)$_r$ were exposed to iodine vapor for 10 minutes that selectively stains the P4VP(**4T**)$_r$ block to enhance the contrast. TEM images were collected on a FEI Tecnai 12 transmission electron microscope at an accelerating voltage of 120 kV.

2.4.6 Organic Field-Effect Transistor (OFET) Fabrication

The devices were fabricated on low resistivity n-type silicon wafers, using 1000 Å of thermally grown SiO_2 as the dielectric, in top contact geometry. Sample thin films were prepared as previously described. Gold contacts were patterned on top of the films, using various shadow masks, giving channel lengths from 5 to 40 μm and widths from 200 to 400 μm. All devices were tested as p-type OFETs in the accumulation regime and saturation mobilities were calculated using the equation, $\mu = g_m^2 / 2I_D C_{ox}(W/L)$, where g_m = transconductance, I_D = current measured at the drain electrode, C_{ox} = capacitance of the insulator, W = width of the electrodes, and L = channel length. The electrical measurements were performed in a nitrogen atmosphere using an Agilent 4156C Precision Semiconductor Parameter Analyzer.

Chapter 3
Assembly, Kinetics, and Thermoresponsive Properties of Oligothiophene-Based Supramolecules

Small organic molecules with strong intermolecular interactions have a wide range of desirable optical and electronic properties and rich phase behaviors. Incorporating them into block copolymer (BCP)-based supramolecules opens new routes to generate functional responsive materials. Using the oligothiophene-containing supramolecules that were introduced in the previous chapter, we present a systematic study of the critical thermodynamic parameters and kinetic pathways that govern the coassemblies of BCPs and strongly interacting small molecules. A number of potentially useful morphologies for optoelectronic materials, including a nanoscopic network of oligothiophene and nanoscopic crystalline lamellae, were obtained by varying the assembly pathway. Hierarchical coassemblies of oligothiophene and BCP, rather than macrophase separation, can be obtained. Crystallization of the oligothiophene not only induces chain stretching of the BCP block the oligothiophene is hydrogen-bonded to but also changes the conformation of the other BCP coil block. This leads to an over 70% change in the BCP periodicity (e.g. from 31 nm to 53 nm) as the oligothiophene changes from a melt to a crystalline state, which provides access to a large BCP periodicity using fairly low molecular weight BCP. The present studies have demonstrated the experimental feasibility of generating thermoresponsive materials that convert heat into mechanical energy. Incorporating strongly interacting small molecules into BCP supramolecules effectively increases the BCP periodicity and may also open new opportunities to tailor their optical properties without the need for high molecular weight BCP. This chapter was adapted with permission from Rancatore *et al. Macromolecules*, **2012**, 45, 8292. Copyright 2012 American Chemical Society.

§ 3.1 Introduction

Functional and stimuli-responsive polymer and supramolecular materials are in great demand for biomedical, sensing, and electronic applications.[1-3] Thermally reversible order–order transitions have been demonstrated in both block copolymer (BCP) and supramolecular systems.[2,4] Photoisomerizable liquid crystalline (LC) moieties in polymer networks have been shown to dramatically increase the large-scale shape changes induced by light.[1,3] LC-containing BCPs in which LC molecules are covalently attached to the side chains of one BCP block have been investigated, and the LC molecules can be used to macroscopically align BCP microdomains or to obtain morphological changes.[5-13]

Supramolecules are constructed through the noncovalent linking of small molecules to polymer side chains *via* hydrogen bonding, electrostatic interactions, or metal ligation.[2,14-26] Small molecules are among the most diverse building blocks in terms of structure and functionality. Supramolecular approaches provide access to a wide combination of small molecules and polymers by circumventing many of the synthetic challenges frequently faced in the synthesis of functional materials. They also allow significant tuning of the thermodynamics and kinetics of the self-assembly process. Attaching small molecules to the side chains of a polymer may increase the rigidity of the polymer and change its architecture, which ultimately affects the supramolecular phase behavior in bulk and in thin films.[27-31] The noncovalent linkage between a small molecule

and a polymer provides convenient access to responsive supramolecular materials.[2,25,26,32] Extensive studies have been carried out on supramolecules based on end-functionalized alkyls.[2,17,20,26-31] A variety of other small molecules, such as liquid crystals (LCs) and organic semiconductors, have much stronger intermolecular interactions, which lead to more interesting and complex molecular packing and phase behavior than observed for simple alkyl molecules.[33-35] Recently, we showed that oligothiophene-containing supramolecules can overcome the solution processability limitation of organic semiconductors and can be spin-casted into uniform films with low surface roughness without compromising charge mobility.[36] Supramolecules based on such functional small molecules provide opportunities toward functional material synthesis.

However, there have been limited studies on supramolecules containing small molecules that possess strong intermolecular interactions.[36-38] Small molecules may crystallize and macrophase separate from the BCP matrix.[38,39] This reduces the stoichiometry between the small molecule and polymer repeat unit, which changes the polymer chain conformation, the chain rigidity, the interaction parameters between the two blocks, and the volume fraction of the comb block. Kinetically, the chain architecture and mobility strongly depend on the molecular packing of the attached small molecules, and the hierarchical assemblies may also have pathway dependence. It is likely that multiple kinetically trapped states can be long-lived to capture nonequilibrium nanostructures.[27-29] The effect of the small molecule on the chain architecture and mobility can potentially amplify the thermal responsiveness of the material.

Here, we report the systematic study of oligothiophene-containing supramolecules to elucidate how the phase behavior and molecular packing of strongly crystalline small molecules affect the thermodynamics, kinetics, and thermal responsiveness of a supramolecule's assembly in bulk. Hierarchical assemblies where oligothiophenes are exclusively incorporated within BCP lamellae can be obtained even from macrophase-separated states. By tailoring the thermal annealing conditions, a number of different morphologies, including a nanoscopic network of oligothiophene and nanoscopic crystalline lamellae, can be achieved to potentially control the dimensionality of the electronic percolation pathway. Furthermore, the crystallization of the oligothiophene not only induces chain stretching of the hydrogen-bonded comb block but also changes the conformation of the BCP coil block. An over 70% increase in the BCP periodicity (from 31 to 53 nm), as opposed to ~10–20 % observed in prototype alkyl-containing supramolecules, can be achieved when the oligothiophene changes from a melt to a crystalline state. The structural change in microdomain size occurs rapidly (within minutes) and is fully reversible. This study provides insight into a modular method to generate thermoresponsive and electroactive materials and may open new possibilities to tailor the optical properties of block copolymers without requiring the synthesis of high molecular weight BCPs.

§ 3.2 Results

A quaterthiophene, 5'''-(3,7-dimethyloctyl)-5-(3-(3-hydroxyphenyl)propyl)-[2,2';5',2'';5'',2'''] (identified as "**4T**"), was synthesized using a previously reported procedure.[36]

4T forms a hydrogen bond with the 4-vinylpyridine repeat unit of a polystyrene(40 kDa)-*block*-poly(4-vinylpyridine)(5.6 kDa) (PS-*b*-P4VP) BCP to form a supramolecule, identified as PS-*b*-P4VP(**4T**)$_r$ (Figure 3.1). The ratio of **4T** to 4VP, *r*, is fixed at 1.5.

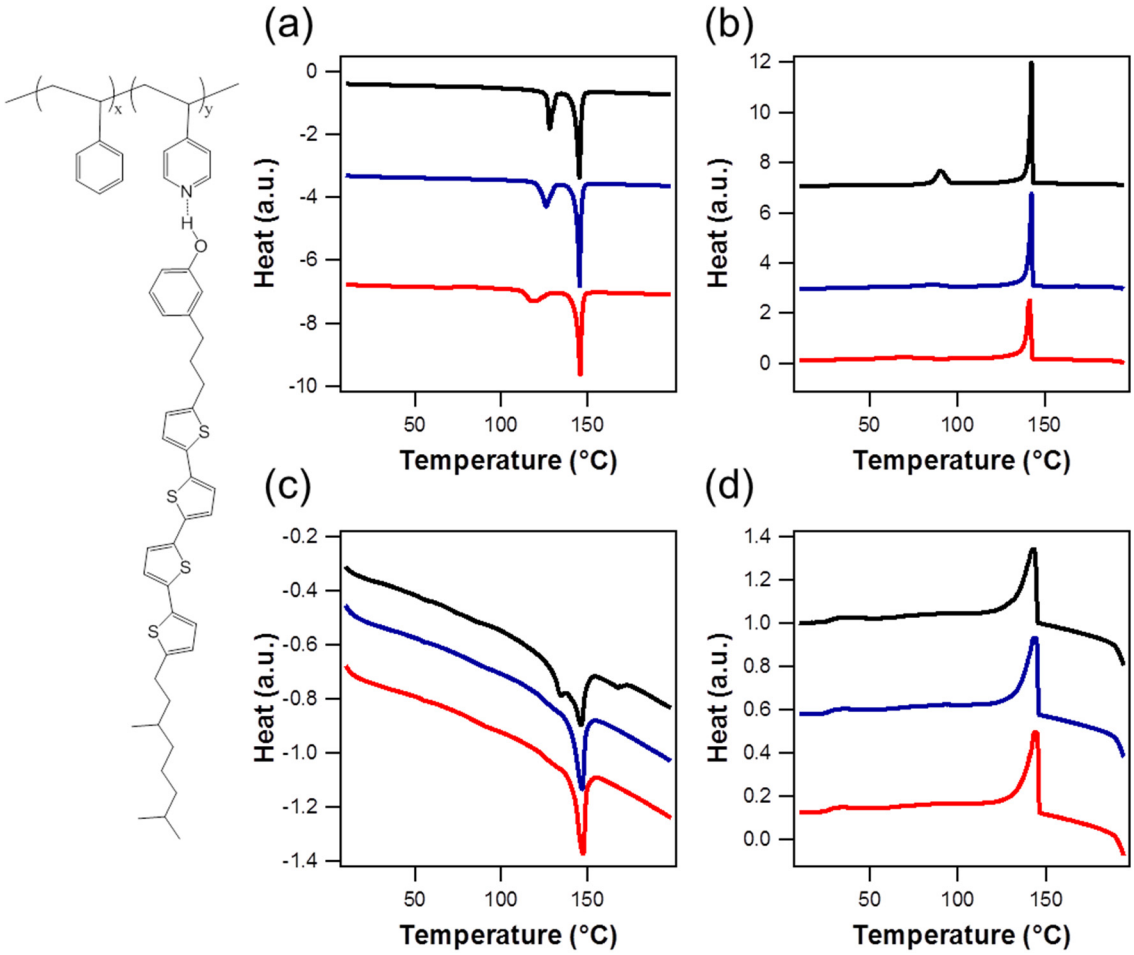

Figure 3.1. (left) Chemical structure of a PS-*b*-P4VP(**4T**)$_r$ supramolecule. DSC curves during three (a, c) heating and (b, d) cooling cycles of (a, b) **4T** and (c, d) PS-*b*-P4VP(**4T**)$_{1.5}$ supramolecules. The higher melting temperatures of **4T** alone and PS-*b*-P4VP(**4T**)$_r$ supramolecules are similar. The T_g of the amorphous block cannot be discerned based on the DSC profile. First (black/top), second (blue/middle), and third (red/bottom) cycles are displaced along the y-axis for clarity.

The crystallization of **4T** determines the chain rigidity, conformation, and mobility of the supramolecule and was first investigated using differential scanning calorimetry (DSC). Figure 3.1 shows the three consecutive DSC scans during the heating/cooling cycles for **4T** and PS-*b*-P4VP(**4T**)$_{1.5}$. Both samples were cast from chloroform, following the sample preparation

conditions used for subsequent structural studies. For pristine **4T**, two endothermal peaks are observed at 128 and 146 °C during the first heating cycle with a peak area ratio of 1:2.2. Two exothermal peaks are observed at 90 and 142 °C in the first cooling cycle. In the subsequent heating/cooling cycles, the peak at 146 °C remains the same, while the original peak at 128 °C is now observed at 120 °C. For PS-*b*-P4VP(**4T**)$_{1.5}$, a similar DSC curve is observed for the first cycle and two melting peaks are observed at 134 and 147 °C. The heat of crystallization decreases from approximately 44.0 kJ/mol for **4T** alone to 21.2 kJ/mol for **4T**s in the PS-*b*-P4VP(**4T**)$_{1.5}$ supramolecules (48% crystallinity). Additionally, in the second heating cycle, the peak at the lower melting temperature disappears, and only one endothermal peak at 148 °C remains. It is likely that BCP microdomains provide a nanoscopically confined environment that favors the molecular packing with a higher T_m. From the electronic property point of view, a higher T_m is more desirable to retain the charge mobility of the oligothiophene.

Small-angle X-ray scattering (SAXS) and wide-angle X-ray scattering (WAXS) were used to characterize the supramolecular assemblies and the molecular ordering of **4T**, respectively (Figure 3.2). All samples were annealed at 40 °C under vacuum for 8 h to remove residual solvents. The annealing temperatures were selected to be below, close to, or above the two melting temperatures observed in DSC thermograms and the supramolecules were then slowly cooled to room temperature over a few hours. For PS-*b*-P4VP(**4T**)$_{1.5}$ annealed at 40 °C, the SAXS profile is very broad in the low q regime (Figure 3.2a). Two fairly broad diffraction peaks are observed at q = 0.11 and 0.22 Å^{-1}, similar to that of **4T** alone (Figure 3.2b). For the 40 °C-annealed PS-*b*-P4VP(**4T**)$_{1.5}$, macrophase separation between the BCP and **4T** is observed. After annealing at 100°C, the low q scattering profile corresponding to the BCP assemblies becomes more pronounced. The peak at q = 0.11 Å^{-1} is split into two peaks with a periodicity of 6.3 and 5.5 nm. These two spacings coincide with the lamellae periodicity of the P4VP(**4T**)$_r$ comb block and **4T** alone, respectively. A similar set of diffraction peaks are observed after annealing at 120 °C while distinctive diffraction peaks at q = 0.012 and 0.037 Å^{-1} appear, indicating that PS-*b*-P4VP(**4T**)$_{1.5}$ forms a BCP lamellar morphology with a periodicity of 53 nm.

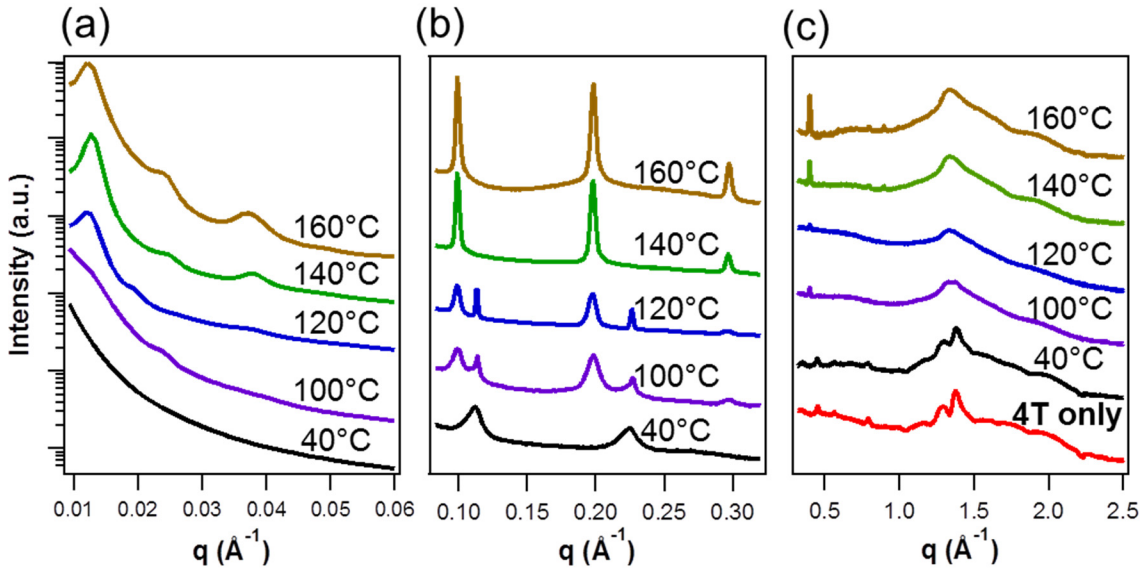

Figure 3.2. (a, b) SAXS and (c) WAXS profiles of PS-*b*-P4VP(**4T**)$_{1.5}$ supramolecules and **4T** annealed at selected temperatures. The macrophase-separated and BCP lamellae-incorporated **4Ts** have periodicities of ~5.5 and ~6.3 nm respectively. Thermal annealing at or above the melting point yields a complete incorporation and a significant increase in BCP periodicity (27 nm vs 52 nm). (c) WAXS curves show peaks corresponding to the molecular packing of **4T** with a periodicity of 4.6 - 4.9 Å.

For supramolecules annealed near and above the T_m of **4T**, SAXS profiles show hierarchical assemblies containing both BCP lamellae, ~52 nm in period, and the 6.3 nm lamellae from the P4VP(**4T**)$_r$ comb block.

For **4T** alone, two diffraction peaks at 1.29 and 1.38 Å^{-1} are observed in the WAXS profile, suggesting **4T** forms a herringbone structure as commonly observed with other oligothiophenes (Figure 3.2c).[40-42] A similar WAXS profile is observed for PS-*b*-P4VP(**4T**)$_{1.5}$ annealed at 40 °C. After annealing, these two peaks merge into a single, broader peak centered at q ~ 1.330 Å^{-1}. Qualitatively, the WAXS profiles for the annealed supramolecules with different treatments are very similar; however, there is a slight increase in the intensity of the peak at q = 1.330 Å^{-1} when the sample is annealed at or above the melting temperature of **4T**. It is possible that the molecular packing of **4T** may vary upon being sequestered within the BCP lamellae. However, since the **4T** crystals in the P4VP(**4T**) domains are small, it is also likely that the two peaks are broadened and thus appear to have merged. Nevertheless, the WAXS profile confirms the molecular packing of **4T** within the supramolecular assemblies, rather than being amorphous.

To enhance the contrast for TEM studies, the thin sections were stained with iodine that selectively localizes in the **4T**-rich region. As shown in the Appendix (A.1.1), iodine staining does not modify the supramolecular assemblies. Although there are structural inhomogeneities for the

PS-*b*-P4VP(**4T**)$_{1.5}$ annealed at temperatures below the T_m of **4T**, the TEM results shown are fairly representative in terms of the different assemblies which were observed experimentally. After annealing at 40 °C, macrophase separation occurs and mixtures of different features can be clearly seen in the low-magnification TEM images (Figure 3.3a). The dark regions, typically a few hundreds of nanometers in size, which correspond to the macrophase separated **4T**, are randomly distributed throughout the samples (Figure 3.3a, b). Based on the feed ratio of PS-*b*-P4VP(**4T**)$_{1.5}$, the volume fraction of P4VP(**4T**) is ~0.6. The macrophase separation and crystallization of **4T** reduce the local volume fraction of P4VP(**4T**)$_r$. A cylindrical morphology in which P4VP(**4T**)$_r$ cylinders are embedded in a PS matrix is observed.

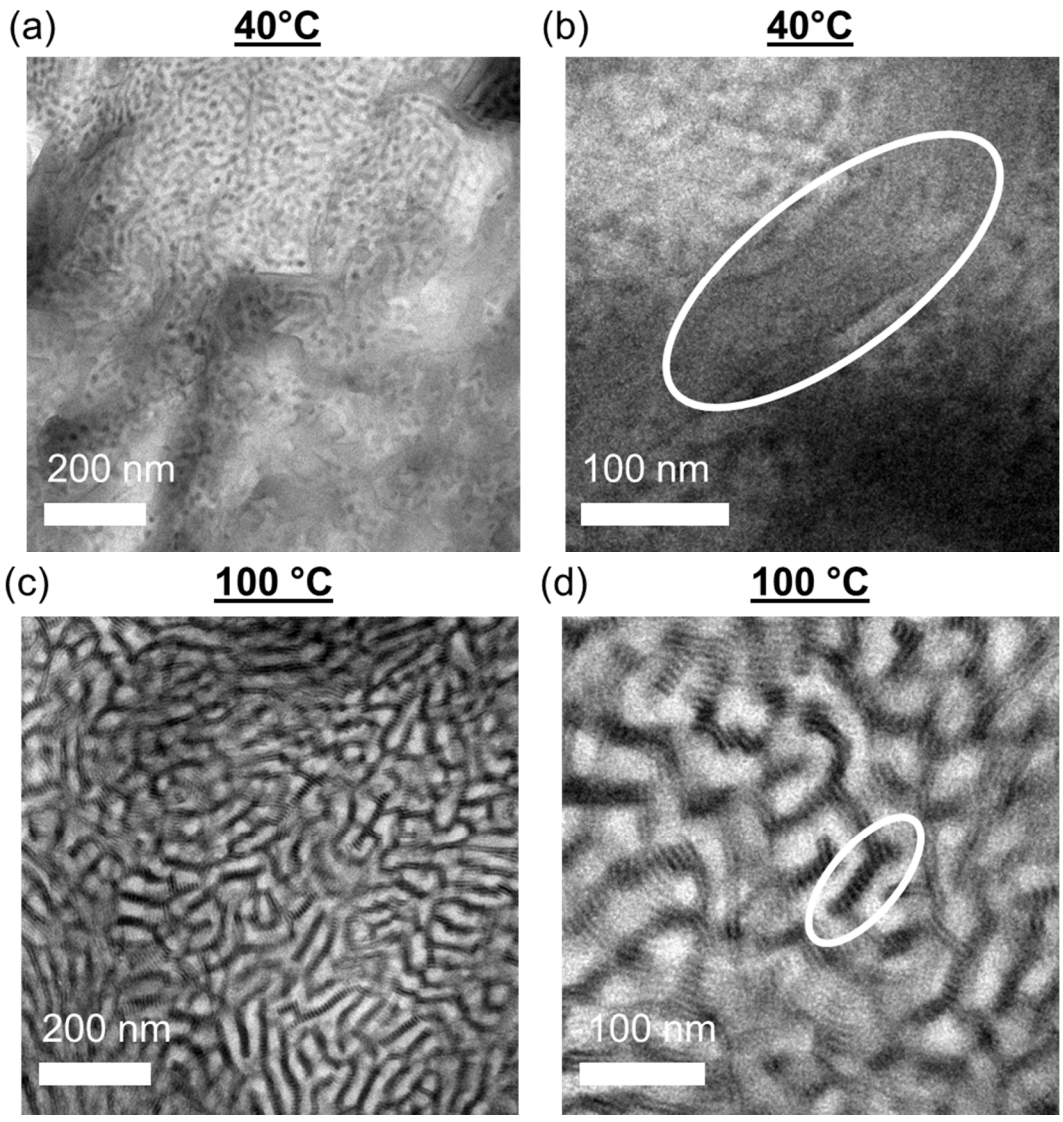

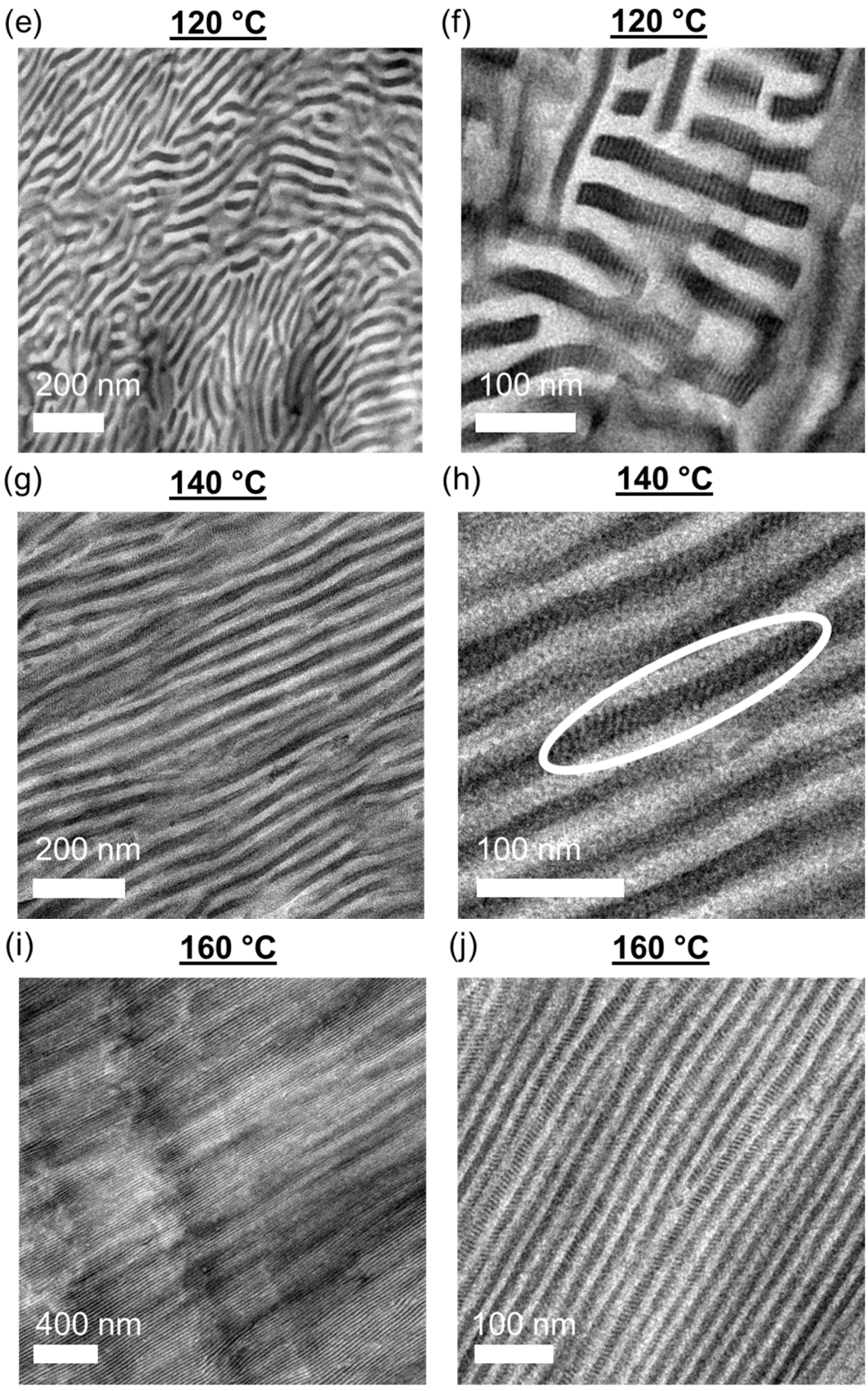
(e)
120 °C
200 nm
(f)
120 °C
100 nm
(g)
140 °C
200 nm
(h)
140 °C
100 nm
(i)
160 °C
400 nm
(j)
160 °C
100 nm

Figure 3.3. TEM images of PS-*b*-P4VP(**4T**)$_{1.5}$ supramolecules annealed at various temperatures. (a, b) The unannealed sample shows a mixture of morphologies. Regions of macrophase-separated **4T** are highlighted in the circled region in (b). (c, d) A network-like morphology is observed after thermal treatment at 100 °C. Nanoscopic features are connected with smaller lamellae with a ~6 nm periodicity (circled region). (e, f) Lamellar morphology with poor long-range order is obtained after thermal annealing at 120 °C. (g–j) Lamellae-within-lamellae morphology where the P4VP(**4T**)$_{1.5}$ comb block forms small lamellae with a ~6 nm periodicity are observed upon heating at temperatures close to or above the melting temperature of **4T**. Lamellae-within-lamellae hierarchical assemblies with large grain sizes are observed without applying external fields.

Figure 3.3c, d shows the TEM images of PS-*b*-P4VP(**4T**)$_{1.5}$ annealed at 100 °C, which is above the glass transition of PS block but below the T_m of **4T**. The hydrogen bonding between the **4T** and 4VP should be stable at this temperature.[43] No large regions containing macrophase-separated **4T** were observed for all the TEM thin sections prepared, and randomly distributed lamellae are observed in Figure 3.3c, d. Within the BCP lamellae, small features are also obvious and are assigned to the lamellae from the P4VP(**4T**)$_r$ comb block. Between the neighboring BCP lamellae, smaller lamellae are seen with the periodicity of ~6 nm. These features, expected to correspond mainly to **4T** molecules, contribute to the diffraction peaks observed at q = 0.114 and 0.227 Å^{-1}. The **4T** lamellae effectively bridge two BCP lamellae to provide a continuous electronic pathway, presumably similar to what was observed in our previous thin film OFET studies and will not be discussed in this contribution.[36]

Following annealing at 120 °C, the frequency of the small **4T** lamellar features that join two BCP lamellae is reduced substantially. The PS-*b*-P4VP(**4T**)$_{1.5}$ forms BCP lamellae with abundant defects and a nonuniform periodicity since there are still some **4T**-rich regions. After annealing at 140 °C, slightly below the T_m of **4T**, BCP lamellae with a larger grain size and a fairly uniform periodicity can be clearly seen and distinctive small lamellar features of the P4VP(**4T**) comb block are seen within the BCP lamellae. After annealing above the T_m of **4T** (160 °C), a lamellar morphology with very large grain sizes is observed. Although there are local defects, the BCP lamellae are macroscopically aligned over tens of micrometers without the need to apply an external field. We have never observed macrophase separation in any sample that has been thermally annealed above 140 °C. The **4T** are completely solubilized within the BCP lamellae even though the molar stoichiometry of **4T**:4VP is 1.5.

In situ SAXS studies were carried out to follow the self-assembly process of PS-*b*-P4VP(**4T**)$_{1.5}$ as a function of annealing temperature to elucidate the timescale and temperature range of the structural evolution of the material. Figure 3.4 shows the *in-situ* SAXS profiles where a 40 °C-annealed PS-*b*-P4VP(**4T**)$_{1.5}$ sample was heated from 30 °C to 150 °C, then cooled to 100 °C. The sample was annealed for 10 minutes at each temperature before the SAXS profile was collected and remained at that temperature for an additional 25 minutes. Overall, the structural evolution of PS-*b*-P4VP(**4T**)$_{1.5}$ is quite similar to that shown in the static studies and PS-*b*-P4VP(**4T**)$_{1.5}$ forms well-defined hierarchical assemblies when heated above the T_m of **4T**. Rather

surprisingly, changes in the scattering profile of PS-*b*-P4VP(**4T**)$_{1.5}$ starts quite early as the temperature reaches 70 °C.

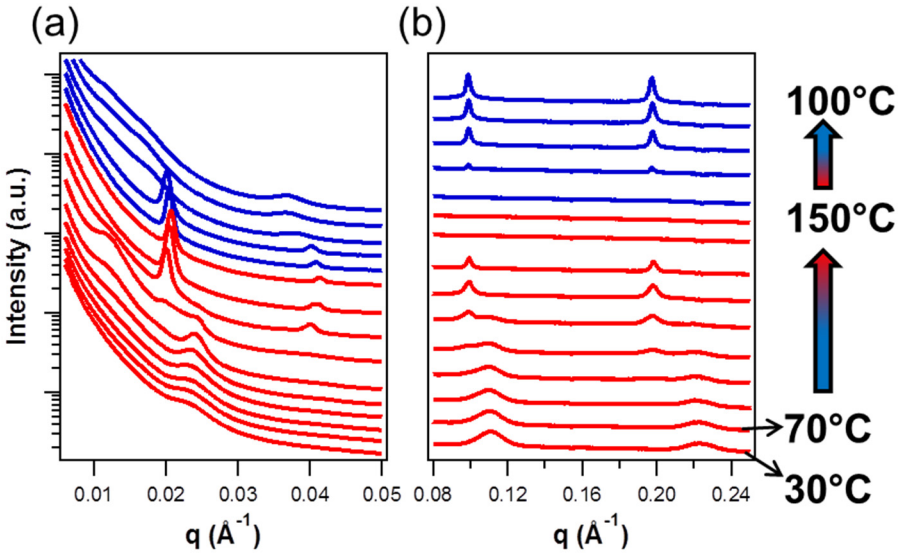

Figure 3.4. (a, b) In-situ SAXS measurements of unannealed PS-b-P4VP(**4T**)$_{1.5}$ supramolecules to monitor the structure evolution during thermal annealing. (a) There is an increase in the sharpness and intensity of the peaks related to the BCP morphology as the sample is heated. As the sample is cooled, there is a large change in the BCP periodicity. (b) The peaks corresponding to macrophase separated **4T** (5.5 nm) decrease as the sample is heated above 70 °C until they disappear at 120 °C. The peaks corresponding to P4VP(**4T**)$_r$ comb lamellae (6.4 nm) appear at 100 °C, disappear when **4T** melts, and reappear when the small molecules crystallize upon cooling.

Upon heating to 70 °C, the intensity of the diffraction peaks corresponding to macrophase-separated **4T** decreases, and the peak related to the BCP morphology (~27 nm) increases. Thus, the supramolecule clearly has mobility well below the T_m of **4T** and the glass transition temperature of pristine PS, suggesting that amorphous **4T** is solubilized in the PS microdomains after solvent casting. Additionally, the 6.4 nm periodicity peaks are no longer present at 140 and 150 °C, indicating that the P4VP(**4T**)$_r$ comb block has completely melted.

Once the incorporation of **4T** within the BCP lamellae was complete, we performed *in situ* SAXS to investigate the effect of crystallization and molecular packing of the oligothiophene on the supramolecular structures. Figure 3.5 shows the *in situ* SAXS profiles of a preannealed PS-*b*-P4VP(**4T**)$_{1.5}$ supramolecule upon heating from 30 to 195 °C and then cooling to 110 °C. Upon heating above 140 °C, **4T** melts and, simultaneously, the BCP lamellar periodicity is reduced to 31 nm. After cooling below the T_m of **4T**, the PS-*b*-P4VP(**4T**)$_{1.5}$ forms lamellae-within-lamellae hierarchical assemblies with a BCP lamellar periodicity of ~50 nm. The process occurs within minutes and is thermally reversible.

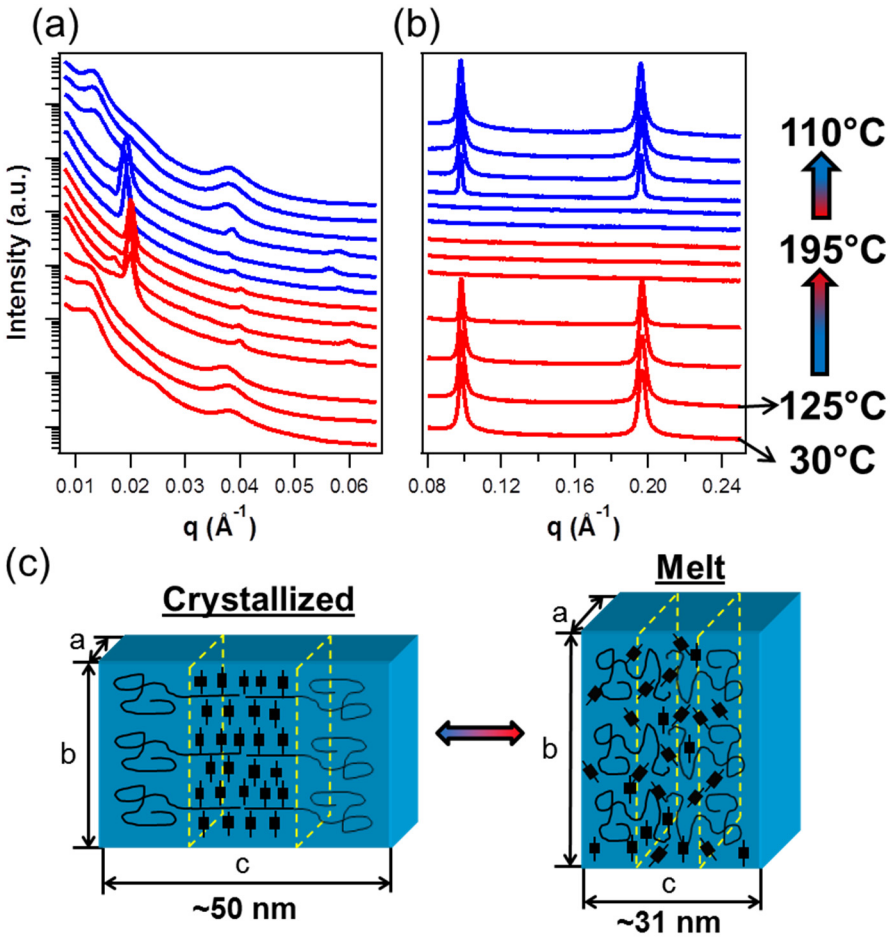

Figure 3.5. (a, b) In-situ SAXS measurements of preannealed PS-*b*-P4VP(**4T**)$_{1.5}$ to confirm the thermal reversibility of the structural changes. Upon heating above or cooling below the melting point of **4T**, the BCP lamellae periodicity changes from ~31 to ~50 nm, respectively. This process is thermally reversible. (c) Schematic drawing of the chain conformation above and below the melting point of **4T**. Because of strong intermolecular interactions between **4T** molecules, both the PS and P4VP blocks are significantly stretched, contributing to the >70% increase in the BCP periodicity.

§ 3.3 Discussion

Our findings show at least two unique aspects of supramolecules based on strongly interacting oligothiophenes. First, homogeneous supramolecular assemblies can be obtained from macrophase-separated blends. Upon thermal treatment, "loose" oligothiophenes (**4T**) can be selectively incorporated into BCP lamellar microdomains to form homogeneous hierarchical assemblies even though **4T** has a strong tendency to crystallize. Second, there is an unusually large change in the BCP periodicity induced by the crystallization of **4T**. The expansion and reduction

of the BCP periodicity exceeds 70%, a value which is much higher than previously observed in supramolecules based on less strongly interacting components, such as alkyl moieties in BCP systems.[2] An *in-situ* SAXS study of a pentadecylphenol-based (PDP) supramolecule, PS(40 kDa)-*b*-P4VP(5.6 kDa)$(PDP)_2$, in the Appendix (A.1.2) demonstrates a much smaller thermal response of the BCP periodicity (~20%). The observed dramatic structural changes opens interesting opportunities: one is to obtain BCP lamellae with high periodicity for optical devices while using fairly low molecular weight BCPs.[44] This is similar to what is observed with comb BCPs, but the supramolecular approach eliminates the synthetic requirements of comb BCP synthesis and should be applicable to a range of functional small molecules that cannot be readily incorporated into comb BCPs.[45] The other is to convert thermal energy to mechanical forces with potential control over the direction of the force vector for shear-aligned supramolecules.

Based on observed DSC measurements, scattering profiles, and TEM images, only a fraction of **4T** was hydrogen-bonded to the P4VP and macrophase separation occurs during the solvent evaporation process, presumably due to the limited solubility of **4T** in chloroform and its high tendency to crystallize. This reduces the volume fraction of the P4VP(**4T**)$_r$ block. It is worthwhile to note that at a low stoichiometry of **4T** to 4VP, the organic semiconductor-containing supramolecules can readily form morphologies similar to those of BCPs.[36] No large aggregates were observed in the TEM images (Figure 3.3a, b). The "loose" **4T** may form many small crystallites or remain amorphous and solubilized in the PS-rich microdomains. Although the temperature is well below the T_m of **4T**, these loose **4T** molecules gain sufficient mobility to enable their short-range diffusion to form the morphologies observed in Figure 3.3c–f upon heating. When the supramolecules are annealed near or above the T_m of **4T** (140–160 °C), there is sufficient mobility to form hierarchical assemblies. Interestingly, large grain sizes, as seen in Figure 3.3i, were observed without applying external field.

For small molecules with rather weak interactions, macrophase separation can be eliminated during the solution casting process and homogeneous hierarchical assemblies can be readily obtained upon solvent removal. However, for strongly interacting molecules that frequently possess unique material properties, macrophase separation has a much higher tendency to occur, making it challenging to obtain nanoscopic materials. Our findings are very encouraging and highlight the feasibility to synchronize the self-assembly processes of BCPs and small molecules.

Energetically, there are a few factors that determine the balance between macrophase separation and supramolecular assemblies. There are clear difficulties to quantify every energetic contribution to the supramolecular assembly process, and we will qualitatively discuss knowledge gained as a result of the present studies. The **4T**–4VP hydrogen bonding favors **4T** incorporation into BCP microdomains. However, the hydrogen bond weakens at elevated temperature and starts to break at 110 °C.[43] The stoichiometry between **4T** and 4VP exceeds 1, and there is a significant fraction of loose **4T**. Yet, the crystallization of **4T** remains confined within the BCP lamellae during the cooling process, forming nanoscopic **4T** crystals with macroscopic alignment relative to the BCP interface. Thus, a comb block with only a fraction of **4T** molecules hydrogen-bonded with the 4VPs is sufficient to solubilize all of the "loose" **4T**s. The interaction between PS and **4T** should also play a role in the assembly process. Repulsive PS–**4T** interactions favor the selective

incorporation of **4T** into the P4VP(**4T**)$_r$ block. In the meantime, the PS–**4T** interactions determine the activation energy barrier and the time scale of **4T** diffusion into the PS matrix to transform the system from a macrophase-separated state to hierarchical assemblies. On the basis of the *in situ* SAXS, the time scale to dissolve phase-separated **4T**s is in the range of a few minutes or less. Thus, the PS–**4T** interactions cannot be very strongly repulsive at elevated temperature since **4T** can diffuse through the PS matrix and selectively dissolve in the P4VP(**4T**) microdomains quickly. Rather, the intermolecular interactions between **4T**s should be the main driving force to selectively sequester **4T** within the P4VP block.

The supramolecular approach does compromise the crystallinity of **4T**, limiting it to approximately half of the original **4T**. Specifically, the heat of crystallization decreased from approximately 44.0 kJ/mol for **4T** alone to 21.2 kJ/mol for **4T**s in the PS-*b*-P4VP(**4T**)$_{1.5}$ supramolecules. Similar DSC experiments were performed for a homopolymer-based supramolecule, P4VP(**4T**)$_{1.5}$, and a similar heat of crystallization to that of **4T** alone was observed (see Appendix A.1.3). Both **4T** and P4VP(**4T**)$_{1.5}$ show multiple exothermal peaks during the first cooling cycle in contrast to only one peak observed for the PS-*b*-P4VP(**4T**)$_{1.5}$ supramolecule. On the basis of these results, we conclude that hydrogen-bonding **4T** to P4VP side chain is not sufficient to completely account for the reduction in the **4T** crystallinity. Rather, the DSC results provide some insights into the energetic competition between the crystallization and molecular packing of **4T** and the BCP phase behavior. This is best exemplified by the structural changes represented by the BCP lamellar periodicity during the heating/cooling cycle. TEM image analysis showed that the lamellar widths for both the P4VP(**4T**)$_r$ and PS microdomains remain symmetric after being cooled from 140 or 160°C. This is also reflected by the decrease in intensity of the second-order scattering peak shown in Figure 3.2. Thus, the width of a single lamellae, either PS or P4VP(**4T**)$_r$, increases from ~15 to 26 nm as **4T** crystalizes. For P4VP(**4T**), the increase is expected and can be attributed to the chain stretching led by crystallization of **4T**. This increase has previously been observed for alkyl-containing supramolecules but at a much smaller percentage (10–20%).[2] Although the change in the width of the comb block microdomain is large, the strong tendency of **4T** to crystallize may explain the difference and lead to a larger degree of chain extension. However, we are unaware of such a significant structural change in the BCP coil block, i.e. PS block, in other supramolecular systems. A significant deformation of the PS block is required to accommodate the increase in lamellar width and the mean-square end-to-end distance nearly doubled. The entropic penalty resulting from the stretching of the PS block has to be counterbalanced by the energy gained from the molecular packing of **4T**.

The supramolecular chain conformations upon heating and cooling are presented schematically in Figure 3.5c. The a-axis is defined as parallel to both the BCP lamellae and the comb lamellae, the b-axis is parallel to the BCP lamellae but perpendicular to the lamellae from the comb block, and the c-axis is perpendicular to the BCP lamellae but parallel to the comb lamellae. As the **4T** melts, the P4VP(**4T**)$_r$ block should take on a more bottle-brush-like conformation, and the P4VP and PS chains contract perpendicular to the BCP interface (c-axis). Based on the morphological evolution and the diffusion of loose **4T**, it is likely that some of the **4T**s become solubilized in the PS domain at elevated temperature. During the cooling process, the

4T crystallizes causing stretching of the P4VP chains. The WAXS profiles shown in Figure 3.2c clearly show that the small molecules remain crystalline in the supramolecular assemblies. The P4VP(**4T**)$_r$ chain has to adopt a flat comb block structure and becomes compressed along a- and b-axes to preserve the molecular packing of **4T** in the a-direction. To eliminate the cross-sectional area mismatch, the PS coil block has to be compressed along the same axes. The degree of chain deformation for the PS block reflects the competition between the entropy associated with PS compression along the a- and b-axes and the intermolecular interactions between **4T**. Clearly, the unusually high increase in the thickness of PS lamellae and the overall BCP periodicity showed that for strongly interacting small molecules, like oligothiophenes, it is more energetically favorable to compress the BCP coil block so as to satisfy the small molecule molecular packing.

§ 3.4 Conclusion

We have investigated supramolecules based on organic semiconducting small molecules and block copolymers and have illustrated the basic design parameters governing the phase behavior, self-assembly process, and thermal responsiveness of the supramolecules which are formed as a result of the presence of strongly interacting small molecules. The strong intermolecular interactions and high tendency to crystallize of the small molecules play a key role in the resulting overall supramolecular morphology. Hierarchical coassemblies of small molecules and BCP, rather than macrophase separation, can be obtained. The supramolecules demonstrate a dramatic thermal response, yielding a >70% change the in the BCP periodicity as the oligothiophenes melt and crystallize. This response is much larger than previously observed in other BCP-based supramolecular systems and could potentially lead to thermoresponsive systems that convert heat to mechanical energy. Additionally, using organic semiconductor-containing supramolecules, a wide range of potentially useful morphologies for electroactive materials can be accessed, and their formation directly depends on the annealing conditions. While the present studies have involved an oligothiophene and a lamellar morphology, there are many more opportunities to achieve supramolecular assemblies based on small molecules with different crystal structures and different BCP morphologies for functional processable materials.

§ 3.5 Experimental Section

3.5.1 Materials

PS(40000)-*b*-P4VP(5600) (PDI=1.09) was purchased from Polymer Source, Inc. Chloroform was purchased from Fisher and filtered through basic alumina. All other chemicals were purchased from Aldrich and used as received. The synthetic procedure to prepare **4T** is described in detail in a previous publication.[36]

3.5.2 Sample Preparation

The PS-*b*-P4VP was first dissolved in chloroform to form 1% (w/v) stock solutions. The desired amount of **4T** was dissolved in chloroform. The polymer solution was then added to the **4T** solution, followed by stirring overnight. **4T** is light and oxygen sensitive so cautions were paid to avoid light exposure during the sample preparation process. Solutions were then transferred into PTFE beakers under a covered dish, and solvent was allowed to slowly evaporate for 24 h. Samples were then placed in a vacuum oven at 40 °C for 8 h to remove residual solvent. Bulk samples were collected from the beakers, and portions were put into DSC pans, annealed at various temperatures in a vacuum oven overnight, and slowly cooled to room temperature.

3.5.3 Small and Wide-Angle X-ray Scattering (SAXS/WAXS)

The SAXS and WAXS data were collected on beamline 7.3.3 in the Advanced Light Source (ALS) at the Lawrence Berkeley National Laboratory. X-rays with a wavelength of 1.240 Å (10 keV) were used, and the scattering spectra were collected on a Pilatus 1M detector. The scattering profiles, after a 60 s collection time, were obtained by integrating the 2-D scattering pattern. Line-averaged intensities are reported as I vs. q, where $q = (4\pi/\lambda)\sin(\theta/2)$, λ is the wavelength of incident X-rays and θ is the scattering angle.

3.5.4 Transmission Electron Microscopy (TEM)

The same samples used for SAXS/WAXS were embedded in resin and cured at 60 °C overnight before being microtomed for TEM imaging. The thin sections of PS(40000)-*b*-P4VP(5600)(**4T**)$_r$ were exposed to iodine vapor for 10 min that selectively stains the P4VP(**4T**)$_r$ block to enhance the contrast. TEM images were collected on an FEI Tecnai 12 transmission electron microscope at an accelerating voltage of 120 kV.

3.5.5 Differential Scanning Calorimetry (DSC)

The **4T** and PS-*b*-P4VP(**4T**)$_{1.5}$ samples that were used in the DSC studies were previously annealed at 40 °C. Samples were heated and cooled from 0 °C–200 °C–0 °C for three cycles at a rate of 10 °C/min. DSC thermograms were collected on a TA Q200 DSC with an RCS 40 refrigeration unit.

Chapter 4
Effect of Small Molecule Crystallization and Molecular Packing in Functional Supramolecules

Small molecules (SMs) with unique optical or electronic properties provide an opportunity to incorporate functionality into block copolymer(BCP)-based supramolecules. However, the assembly of supramolecules based on these highly crystalline molecules differs from their less crystalline counterparts. The previous chapters investigated the assembly and electronic properties of a single oligothiophene SM. In this chapter, two families of organic semiconductor SMs are investigated, where the composition of the crystalline core, the location (side- vs. end-functionalization) of the alkyl solubilizing groups, and the constitution (branched vs. linear) of the alkyl groups are varied. With these SMs, we present a systematic study of how the phase behavior of the SMs affects the overall assembly of these organic semiconductor-based supramolecules. First, the incorporation of SMs has a large effect on the interfacial curvature between the microdomains in the overall supramolecular morphology. Second, different SMs can have different effects on the interfacial curvature between the two microdomains, morphology and packing of the supramolecules at equivalent weight fractions. Third, the crystal packing of the SM within the supramolecule doesn't necessarily lead to the assembly of the comb block within the BCP microdomains, as is normally observed for other supramolecules. Fourth, the incorporation of different SMs at similar weight fractions can cause significant differences in the overall periodicity of the supramolecules. An unusual lamellar morphology with a non-uniform interface between the microdomains is observed for supramolecules based on a particular SM and is attributed to changes in the packing structure of the supramolecule. Since the composition of the components of the SMs are modular, these studies provide useful guidance toward tailoring the assembly of optically active and semiconducting supramolecules.

§ 4.1 Introduction

Block copolymer(BCP)-based supramolecules can be constructed by attaching small molecules (SMs) to one or more blocks of a BCP by secondary interactions and can couple the self-assembly processes of BCPs and SMs.[1-13] These supramolecules assemble hierarchically on the order of tens of nanometers, similar to that of BCPs, and on the order of a few nanometers, similar to that of SMs. Extensive studies have been carried out on supramolecules based on end-functionalized alkyls that do not have inherent functionality.[4,6,9,12,13] These supramolecules can easily access large nanostructures which are difficult for BCPs alone[12] and have a number of order-order transitions upon heating.[4,12,13] Selective solvent removal of the SMs after casting can lead to mesoporous materials.[14-16] The use of SMs with optical or electronic properties can incorporate functionality into these supramolecules while taking advantage of the nanostructured assembly of the BCP and minimizing the synthetic effort. These SMs are generally more crystalline and have a much stronger tendency to aggregate than their non-functional counterparts. These characteristics may further complicate their phase behavior and the kinetic pathway of the assembly process. However, there have been relatively limited studies of BCP-based supramolecules based on these strongly interacting SMs, such as liquid crystals (LCs) and organic semiconductors.

LC SMs have demonstrated a number of interesting optical properties and phase transitions. By incorporating them into supramolecules, one can potentially control their orientation and macroscopic alignment and improve their processability. A number of different LC moieties have seen use in supramolecular systems, including (alkoxybenzoyloxy)benzoate,[1]

biphenyl,[17-19] cholesterol,[20-23] and azobenzene.[15,23-25] Non-linear shapes, such as wedges, have also been investigated.[26-28] These materials have demonstrated responsiveness to different stimuli including thermal,[17] electrical,[18] and magnetic[29] stimuli. Organic semiconductor-based supramolecules have also become a topic of interest in recent years. A supramolecular approach has been used to improve the solution processability of organic semiconductors without hindering their charge mobilities using oligothiophene[30] and perylene diimide-based[31] semiconductors. The strong crystallization of the oligothiophene was shown to have a large effect on the morphology and chain architecture of both BCP blocks and significantly enhance the thermal responsiveness of the supramolecule.[32] Conjugated[33,34] and non-conjugated[35-37] BCPs, where one block is designed to bind to fullerenes, were used to facilitate the assembly of donor-acceptor networks for organic photovoltaic (OPV) applications. Films of pyrenebutyric acid have also been investigated in supramolecular systems and were recently used as a fluorescent probe to study their packing in supramolecular thin films.[38,39] Magnetic fields were also used to macroscopically align BCP-based supramolecules with perylene diimide-based SMs, which could be potentially useful to align nanostructures in organic semiconductor devices.[40]

There are a number of competing processes in these systems, including the BCP microphase separation, the crystallization of the SM, the binding strength between the polymer and SM, and the entropic penalty for deforming the polymer chain. Thermodynamically, the formation of supramolecules has a number of effects on the BCP including modifying the chain architecture, stiffness, interaction parameter (χ), and spring constant. Similarly, the binding of the SM to the polymer may affect its crystal structure or its ability to crystallize. Consequently, the phase behavior of the SMs is of critical importance in its coassembly with the BCP.

BCPs with strongly interacting SMs that are covalently attached to one or more blocks of the BCP have been studied more extensively and utilized in a number of areas, including LC and organic semiconductor materials. Like supramolecules, when these SMs are attached to one or more blocks of a BCP, they organize hierarchically on the order of tens of nm and a few nm.[41-45] By attaching these LC SMs to a BCP, their unique optical and stimuli responsive properties can be incorporated into the BCP, and a similar array of structural motifs to those mentioned for supramolecules have been investigated.[46-55] Copolymers with azobenzene side chains have demonstrated a number of interesting optically responsive properties.[52,53,56,57] In LC-semicrystalline BCPs, the crystallinity of the semicrystalline block can be tailored by tuning the volume fraction of the LC block.[54] A number of wedge-like LC moieties have been investigated as side chains[55,58-60] and as a BCP block in wedge-coil BCPs.[61] Donor-acceptor BCPs have been shown to form controlled nanoscopic networks of donor and acceptor materials, which is potentially useful for OPV devices.[62-68] They have also been utilized as BCP compatibilizers to control the grain sizes and enhance the thermal stability of devices when blended with unattached donor and acceptor materials.[68] In many of the studies of LCBCPs and donor-acceptor BCPs, the ordering of the attached side chain SMs within the BCP microdomains has depended on the relative volume fraction of the LC or semiconducting block, and the variation in the molecular ordering of the attached SMs proved to be critical to the overall assembly and phase behavior of the BCP.

Compared to BCPs with covalently attached SMs, BCP-based supramolecules have a higher level of complexity. For example, the non-covalent attachment of SMs introduces a reversible, thermally responsive component to the system and readily allows for the loading of the SMs above and below a 1:1 stoichiometry of SMs to attachment sites. The SMs may also macrophase separate from the BCP or only incorporate partially, which can depend on the binding

strength of the secondary interaction used for attachment, the crystallinity of the SM, and the sample treatment conditions. Kinetically, the distribution and diffusion rate of the SMs can depend on the T_m of the SM and the relative χ between the SMs and each block of the BCP at a given annealing temperature.[12,13,69] While somewhat less complex than supramolecules, BCPs with covalently attached SMs can increase the steric hindrance, decrease the BCP chain mobility during annealing, and hinder the SM crystallization.[70]

Clearly the phase behavior of the SMs plays a key role in the assembly process of BCP-based supramolecules, however, our previous studies were limited to a single SM, and therefore, did not investigate the effect of organic semiconductors with different chemical functionalities and packing structures. Here, we systematically study the effects of the SM crystallization and molecular packing on the supramolecular phase behavior by examining supramolecules based on an array of SM organic semiconductors with different chemical structures and strengths of intermolecular interactions. Specifically, the composition of the crystalline core of the molecule, the placement of the alkyl solubilizing groups on the core (side vs. end functionalization), and the constitution of the alkyl groups (linear vs. branched) are varied to investigate the factors that affect the conformation of the polymer chain as well as the overall supramolecular morphology. Supramolecules based on more weakly interacting semiconductors more readily adopt morphologies with higher curvature, e.g. cylinders, than more crystalline molecules with comparable packing structures. Strongly interacting SMs are shown to have a large effect on the morphology as well as the BCP chain architecture and packing. Specifically, the crystallization of the SM can stretch and compress both BCP blocks, and the crystal packing of the SM can affect the natural packing structure of the BCP.

§ 4.2 Results

Organic semiconductors were designed to hydrogen bond with the 4-vinylpyridine repeat unit of a polystyrene(40 kDa)-*block*-poly(4-vinylpyridine)(5.6 kDa) (PS-*b*-P4VP) BCP to form a supramolecule, identified as PS-*b*-P4VP(**SM**)$_r$ (Figure 4.1). The ratio of SMs to 4VP groups is denoted as *r*. Four different SMs, with chemical structures shown in Figure 4.1, were used. Detailed syntheses of 3-(5'-(3-(4-hydroxyphenoxy)propyl)-[2,2'-bithiophen]-5-yl)-2,5-dioctyl-6-(thiophen-2-yl)-2,5-dihydropyrrolo[3,4-c]pyrrole-1,4-dione (**DOPH**), 2,5-bis(2-ethylhexyl)-3-(5'-(3-(4-hydroxyphenoxy)propyl)-[2,2'-bithiophen]-5-yl)-6-(thiophen-2-yl)-2,5-dihydropyrrolo[3,4-c]pyrrole-1,4-dione (**DEPH**), and 3-(3-(3’’’’’,4’’-dihexyl-[2,2’:5’,2’’:5’’,2’’’:5’’’,2’’’’:5’’’’,2’’’’’]-sexithiophen-5-yl)propoxy)phenol (**6T**) will be discussed in a future publication. 5'''-(3,7-Dimethyloctyl)-5-(3-(3-hydroxyphenyl)propyl)-[2,2’;5’,2’’;5’’,2’’’] quaterthiophene (**4T**) will be referenced in this work from our previous studies as control samples and was synthesized by a previously reported procedure.[30,32] **DOPH** and **DEPH** were synthesized by Dr. BongSoo Kim. **6T** and **4T** were synthesized by Dr. Clayton Mauldin.

All of the SMs are designed to have three main components, i.e. a phenolic moiety to construct the supramolecule, a crystalline semiconducting core, and alkyl groups to enhance their solubility. The strong crystallinity and packing of **4T** was shown to be critical to the overall assembly of the supramolecules.[30,32] The composition of the crystalline core as well as the placement (side vs. end) and constitution of the alkyl solubilizing groups (linear vs. branched) may also play a role in the overall assembly process. Changing these components can affect the

intermolecular strength, T_m, and packing in a crystalline state of a SM. For example, organic semiconductors with branched alkyl groups generally have weaker intermolecular interactions than their linear chain counterparts. **DOPH** and **DEPH** have a core containing a push-pull structural motif with diketopyrrolopyrrole and thiophene groups that give them a lower bandgap and broader absorbance spectrum compared to **4T** and **6T**. These structures have been utilized successfully in both SMs[71] and conjugated polymers[72] for OPV devices. This core favors a crystal packing structure different from that of oligothiophenes, such as the previously studied **4T**, which can have an effect on the overall assembly of supramolecule.[73,74] Both **DOPH** and **DEPH** have side-functionalized, instead of end-functionalized, alkyl solubilizing groups as well. The SMs are structurally identical except **DOPH** has linear octyl solubilizing groups and **DEPH** has branched 2-ethylhexyl groups. This would suggest that **DEPH** has relatively weaker intermolecular interactions than **DOPH**. **6T** contains a sexithiophene core (similar to **4T**) and has unevenly positioned solubilizing groups on the sides of the molecule. This may give it weaker intermolecular interactions or change its crystal packing compared to **4T** since **4T** has an end-functionalized alkyl group.

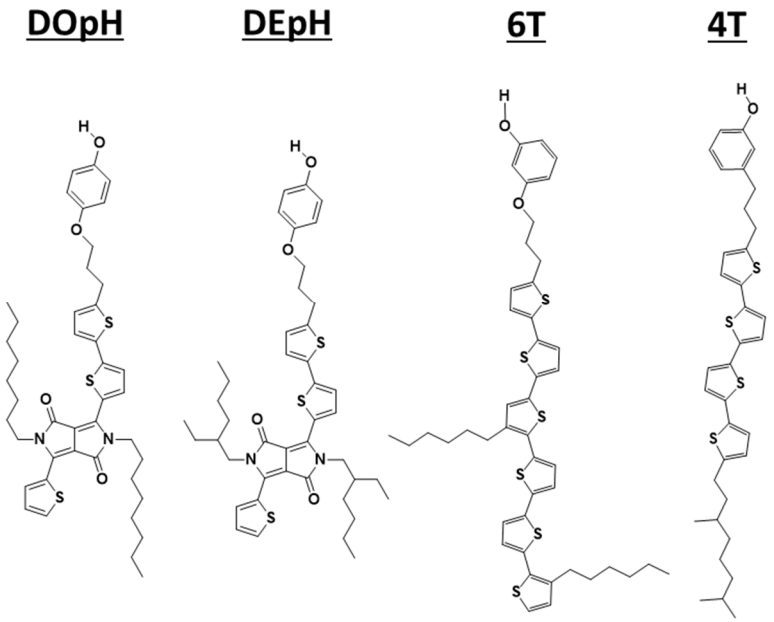

Figure 4.1. Molecular structures of **DOPH**, **DEPH**, **4T**, and **6T**. **DOPH** and **DEPH** have the same crystalline core, but **DOPH** has linear octyl solubilizing groups and **DEPH** has 2-ethylhexyl groups. **6T** has a different crystalline core compared to **DOPH**/**DEPH**. It is similar to the reference molecule, **4T**, but has side-functionalized alkyl groups instead of an end-functionalized group.

Figure 4.2 shows the differential scanning calorimetry (DSC) thermograms used to investigate the crystallinity and packing of the SMs alone. In the first heating cycle for **DOPH**, three endotherms at 138 °C, 144 °C, and 151 °C are observed, however, there is only one exotherm present at 119 °C in the first cooling cycle. In subsequent heating and cooling cycles only the peaks

at 138 °C during heating and 117 °C during cooling remain. This may suggest that the higher temperature peaks correspond to domains that contain solvent-assisted crystal structures or crystal structures that require a much slower cooing rate. The heat of crystallization of pristine **DOPH**, calculated from the integration of the exothermic crystallization peaks at the highest temperature during cooling, is 45.8 kJ/mol. While **DEPH** alone has one endotherm at 157 °C with a high heat of melting (-52.7 kJ/mol) during the first heating cycle, there are no exotherms present while cooling. Subsequent heating cycles show the addition of an exotherm at 76 °C and the return of the endotherm at 154 °C. This indicates that **DEPH** may crystallize very slowly during cooling, and there is molecular reorganization during the transition at 76 °C.

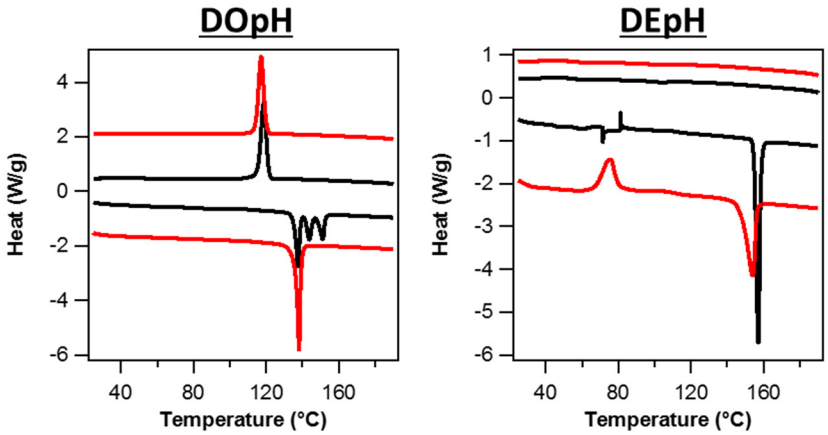

Figure 4.2. DSC curves of (left) **DOPH** and (right) **DEPH** SMs. The first heating/cooling cycles are black and the second are red.

Figure 4.3a, b shows representative transmission electron microscopy (TEM) images of PS-*b*-P4VP(**DOPH**)$_1$ and PS-*b*-P4VP(**DEPH**)$_1$, respectively. At this loading rate, the comb weight fraction (f_{comb}) is 53%. All samples were annealed at 160 °C, above the T_m of all of the components in the system, overnight and then slowly cooled to room temperature over several hours. Thin sections of the bulk samples were stained with iodine, which selectively interacts with the P4VP and SM microdomains and enhances the contrast. The TEM images of PS-*b*-P4VP(**DOPH**)$_1$ primarily show a lamellar morphology with a BCP periodicity of ~38-45 nm and relatively large grains of a single orientation, approximately one to a few microns in size (Figure 4.3a). The interface between the two microdomains undulates and is not as well-defined as is typically seen in lamellar BCPs. Though the periodicity is reasonably uniform, the undulating interface makes the thickness of each block somewhat varied throughout the sample. In addition, there are some domains with a smaller periodicity of ~28 nm where the P4VP(**DOPH**) block is significantly narrower. These areas are less abundant and tend to appear in small clusters. TEM images of PS-*b*-P4VP(**DEPH**)$_1$ show a relatively uniform lamellar morphology with a periodicity of ~30 nm (Figure 4.3b).

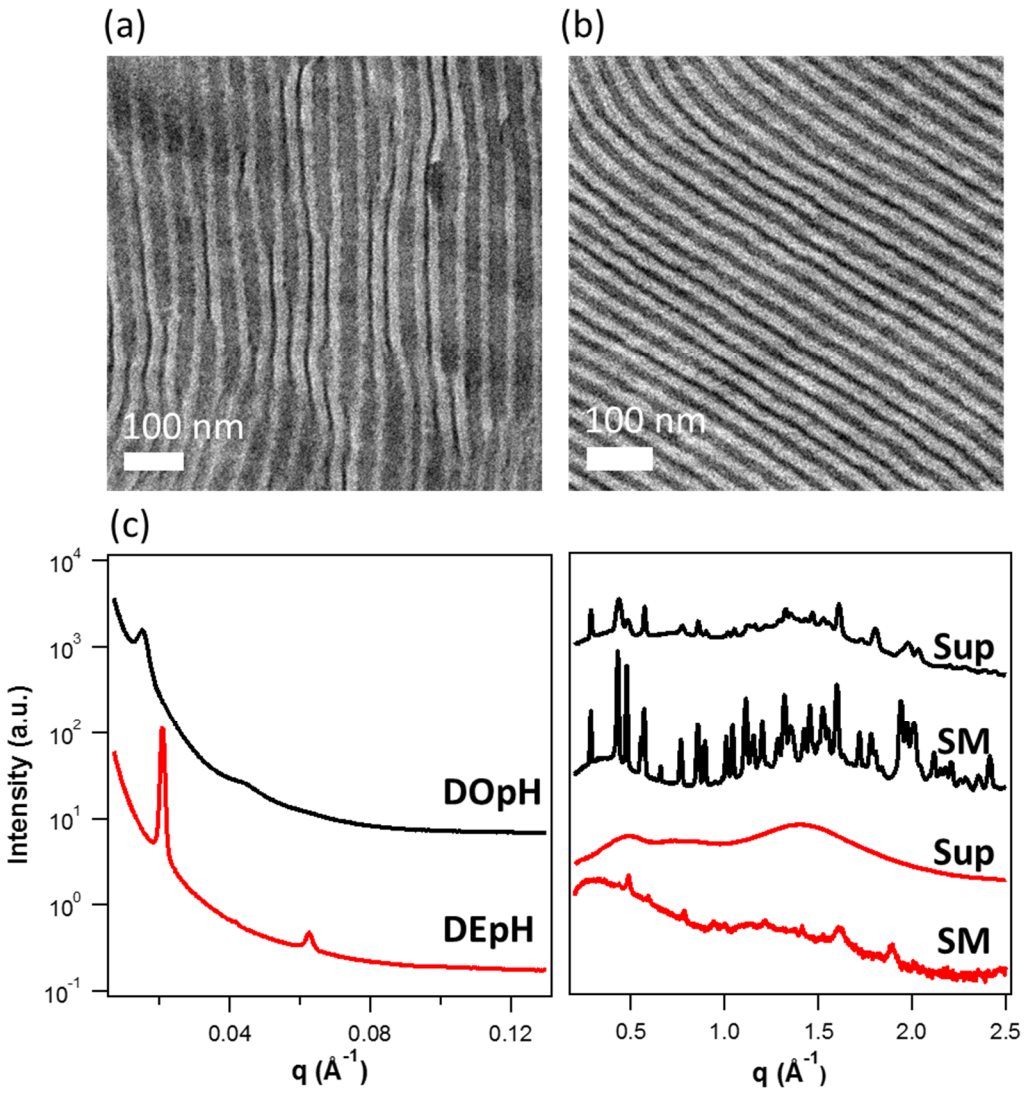

Figure 4.3. TEM images of (a) PS-*b*-P4VP(**DOPH**)$_1$ (f_{comb} = 53%) and (b) PS-*b*-P4VP(**DEPH**)$_1$ (f_{comb} = 53%) supramolecules. (c) (left) SAXS curves of PS-*b*-P4VP(**DOPH**)$_1$ (black) and PS-*b*-P4VP(**DEPH**)$_1$ (red) supramolecules. (c) (right) WAXS curves of PS-*b*-P4VP(**DOPH**)$_1$ (black, Sup), **DOPH** (black, SM), PS-*b*-P4VP(**DEPH**)$_1$ (red, Sup), and **DEPH** (red, SM).

In Figure 4.3c, the SAXS profile of PS-*b*-P4VP(**DOPH**)$_1$ shows a periodicity of ~41 nm, and a very broad 3*q** diffraction peak is present. This can be expected considering the bimodal distribution of the lamellar periodicity and the non-uniform interface between microdomains in the TEM image in Figure 4.3a. While the TEM data and this relatively large BCP periodicity indicate that the SMs have incorporated into the supramolecules, there are no peaks between 0.08-0.27 Å^{-1} corresponding to the comb lamellae that were commonly seen in alkyl SM- or **4T**-based supramolecules in previous works.[5,30] The WAXS curve of **DOPH** alone shows a series of intense peaks in the *q* range between 0.28–2.42 Å^{-1}, which suggests that **DOPH** is highly crystalline under

the current thermal treatment and is in good agreement with the DSC results. While the exact packing structure is not known since single crystals of the SM cannot be easily obtained, its WAXS scattering suggests that its packing is distinct from **4T**.[32,73,74] In PS-*b*-P4VP(**DOPH**)$_1$ supramolecules with the same thermal treatment, the WAXS peaks are still seen but are lower in intensity and broaden somewhat. It is likely that these peaks broaden due to the decreased crystal size of the **DOPH** when sequestered to within the lamellar microdomains.

The SAXS profile of PS-*b*-P4VP(**DEPH**)$_1$ supramolecules shows a periodicity of ~30 nm, and like **DOPH** supramolecules, no diffraction peaks are seen in the higher q range from 0.08–0.27 Å^{-1}, indicating a lack of internal structure of the comb block (Figure 4.3c). It also has a much sharper q^* peak, a suppressed $2q^*$ peak, and a well-defined $3q^*$ peak, indicating that the BCP forms a well-defined lamellar morphology. The WAXS profile of **DEPH** has a number of peaks in the high q range of 0.28–2.42 Å^{-1}, but the scattering is much weaker than for **DOPH**. This suggests that **DEPH** is relatively less crystalline, and the branched alkyl chains hinder the molecular packing of the core, consistent with the DSC results. In thermally-annealed PS-*b*-P4VP(**DEPH**)$_1$ supramolecules, these peaks disappear and only diffuse scattering is present, suggesting a significant reduction in crystallinity of the **DEPH** molecules in supramolecular domains. Since the only difference in the structure between **DOPH** and **DEPH** are the constitution of the solubilizing groups, i.e. **DOPH** has linear alkyl groups and **DEPH** has branched, the relatively weaker crystallinity of **DEPH** and the more typical assembly of PS-*b*-P4VP(**DEPH**)$_1$ are attributed to this.

To investigate if the morphological differences observed for PS-*b*-P4VP(**DOPH**)$_1$ and PS-*b*-P4VP(**DEPH**)$_1$ may be attributed to the phase behavior of the SMs, supramolecules of a higher SM loading rate, where r = 1.5 (f_{comb} = 62%), were investigated. Figure 4.4 shows the DSC thermograms of PS-*b*-P4VP(**DOPH**)$_{1.5}$ and PS-*b*-P4VP(**DEPH**)$_{1.5}$ supramolecules. In the heating and cooling cycles of PS-*b*-P4VP(**DOPH**)$_{1.5}$, only the lower temperature endotherm (138 °C) during heating and exotherm (108 °C) during cooling are present. The heat of crystallization of **DOPH** in PS-*b*-P4VP(**DOPH**)$_{1.5}$ is 35.3 kJ/mol, which corresponds to 77% crystallinity compared to the neat SM. Like **DEPH** alone, PS-*b*-P4VP(**DEPH**)$_{1.5}$ shows a strong melting peak at 154 °C during heating (-36.7 kJ/mol, 70% crystallinity) but doesn't have a crystallization peak during cooling. The second heating cycle shows an exotherm at 117 °C (higher than **DEPH** alone) and a return of the melt at 154 °C. To summarize, **DEPH** has a higher T_m than **DOPH** (154 vs. 138 °C) in supramolecular assemblies, however, like **DEPH** alone, PS-*b*-P4VP(**DEPH**)$_{1.5}$ has no observable heat of crystallization while PS-*b*-P4VP(**DOPH**)$_{1.5}$ retains 77% of the crystallinity of **DOPH**.

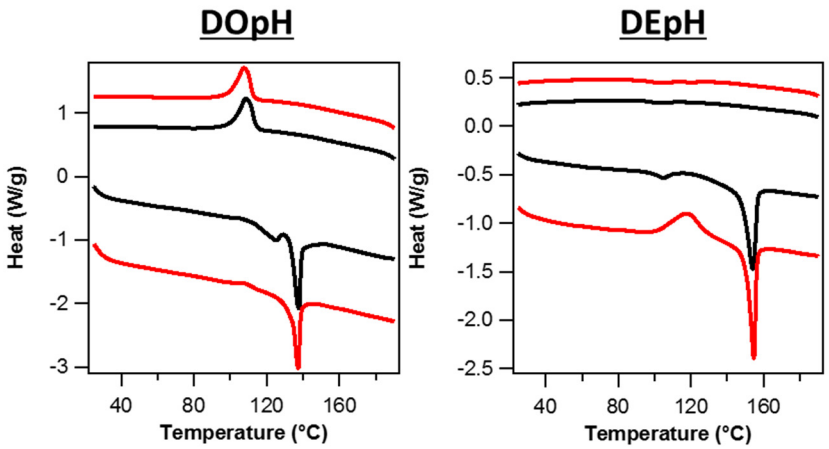

Figure 4.4. DSC curves of (left) PS-*b*-P4VP(**DOPH**)$_{1.5}$ and (right) PS-*b*-P4VP(**DEPH**)$_{1.5}$ supramolecules. The first heating/cooling cycles are black and the second are red.

Figure 4.5a, b shows representative TEM images of PS-*b*-P4VP(**DOPH**)$_{1.5}$ and PS-*b*-P4VP(**DEPH**)$_{1.5}$, respectively, after thermal treatment identical to that of supramolecules at r = 1. The SAXS profiles of PS-*b*-P4VP(**DOPH**)$_{1.5}$ and PS-*b*-P4VP(**DEPH**)$_{1.5}$ both show a slight increase in periodicity compared to their analogues at r = 1, which is unsurprising since the additional SMs can intercalate in between the hydrogen-bonded SMs and can stretch the polymer backbone to a larger extent (Figure 4.5c). PS-*b*-P4VP(**DOPH**)$_{1.5}$ primarily has a lamellar morphology with a ~44 nm periodicity (3 nm increase from r = 1) and large grains of a single orientation. The undulating interface between the two BCP blocks is even more apparent here compared to PS-*b*-P4VP(**DOPH**)$_1$ supramolecules, which indicates that these observations are related to the crystallization of **DOPH**. Despite the increase in **DOPH** loading, there are still some domains with a ~25 nm periodicity. PS-*b*-P4VP(**DEPH**)$_{1.5}$ forms a mixture of cylindrical and lamellar morphology with a ~34 nm periodicity (4 nm increase from r = 1), suggesting that PS-*b*-P4VP(**DEPH**)$_r$ supramolecules more readily adopt curved structures compared to PS-*b*-P4VP(**DOPH**)$_r$. The SAXS profile of PS-*b*-P4VP(**DEPH**)$_{1.5}$ has a much broader q^* peak compared to PS-*b*-P4VP(**DEPH**)$_1$ and no well-defined higher order peaks. This is likely a reflection of the mixture of lamellar and cylindrical morphologies observed for the r = 1.5 sample. The WAXS profiles of PS-*b*-P4VP(**DOPH**)$_{1.5}$ and PS-*b*-P4VP(**DEPH**)$_{1.5}$ are similar to their r = 1 counterparts but have higher intensity scattering peaks due to the higher fraction of SMs. It is likely that the difference between the morphologies observed in **DOPH-** and **DEPH**-based supramolecules is in part due to the stronger heat of crystallization during cooling of **DOPH** compared to **DEPH**. However, unlike previously studied BCPs and supramolecules, PS-*b*-P4VP(**DOPH**)$_r$ (r = 1, 1.5) has a non-uniform interface between the microdomains, and PS-*b*-P4VP(**DEPH**)$_{1.5}$ does not exhibit a uniformly cylindrical morphology. This indicates that the crystallinity and T_m of the SM may not offer a complete explanation for our observations.

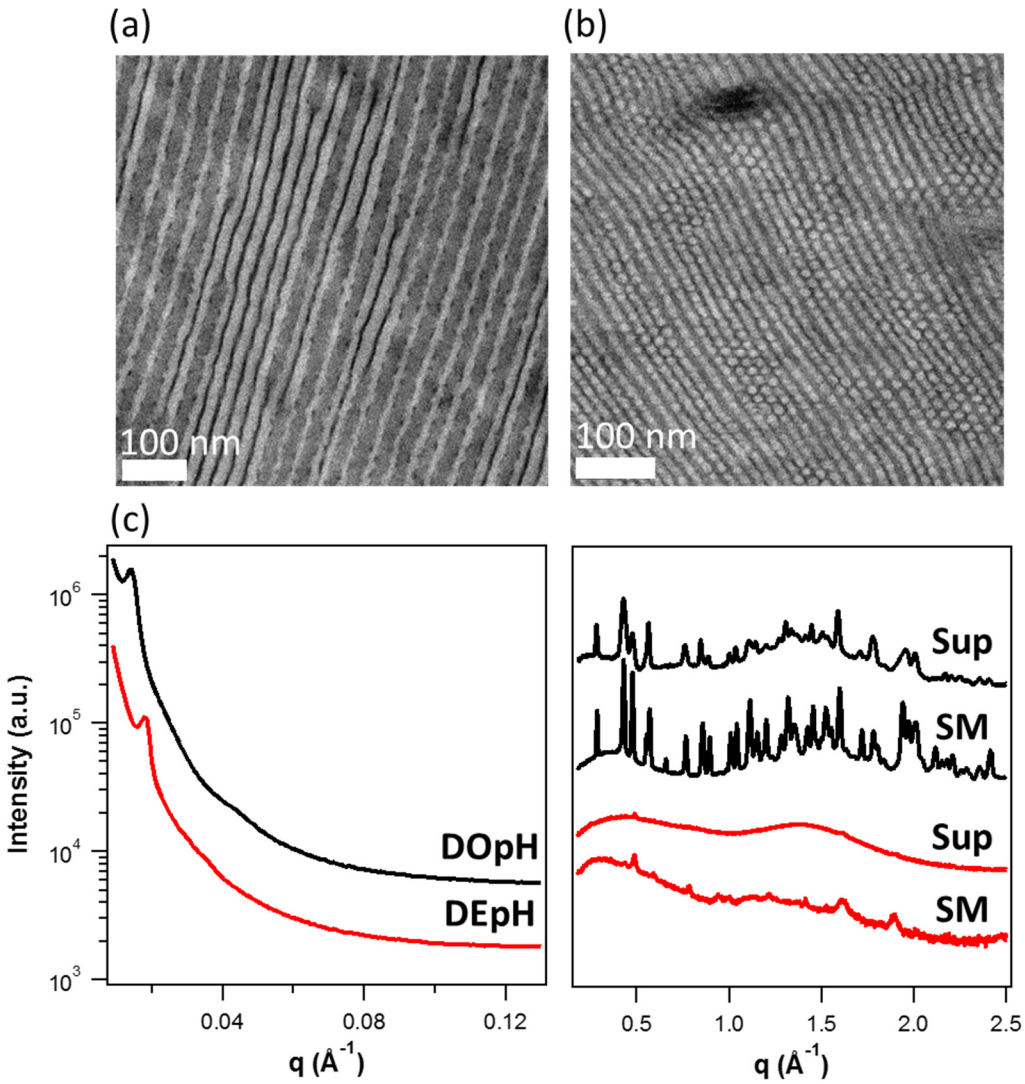

Figure 4.5. TEM images of (a) PS-*b*-P4VP(**DOPH**)$_{1.5}$ (f_{comb} = 62%) and (b) PS-*b*-P4VP(**DEPH**)$_{1.5}$ (f_{comb} = 62%). (c) (left) SAXS curves of PS-*b*-P4VP(**DOPH**)$_{1.5}$ (black) and PS-*b*-P4VP(**DEPH**)$_{1.5}$ (red) supramolecules. (right) WAXS curves of PS-*b*-P4VP(**DOPH**)$_{1.5}$ (black, Sup), **DOPH** (black, SM), PS-*b*-P4VP(**DEPH**)$_{1.5}$ (red, Sup), and **DEPH** (red, SM).

Thus, there are clear differences between the morphologies observed in **DOPH-** and **DEPH-**based supramolecules that are likely due to the relatively stronger intermolecular interactions of **DOPH** compared to **DEPH**. The phase behavior of the SMs is determined by the composition of the crystalline core, the placement of the alkyl solubilizing groups (side vs. end-functionalization), and the constitution (linear vs. branched) of the alkyl groups. Supramolecules based on **DEPH** more readily form morphologies with greater interfacial curvature between microdomains, such as cylinders, and with smaller periodicities relative to those based on **DOPH**. This is likely due to the relatively lower crystallinity of **DEPH** compared to **DOPH**. Since they

are otherwise structurally identical, this is attributed to the branched alkyl solubilizing groups of **DEPH**. However, this does not fully account for the non-uniform interface between the microdomains that are observed in the TEM images of PS-*b*-P4VP(**DOPH**)$_r$ supramolecules. These structures are most likely due to the molecular packing of **DOPH** and **DEPH**. While **DOPH** and **DEPH** vary in the constitution of their alkyl solubilizing groups and in the strength of their intermolecular interactions, their crystalline cores are identical and most likely have similar packing motifs. However, since **DEPH** molecules are not as strongly interacting as **DOPH**, these structures are not observed for PS-*b*-P4VP(**DEPH**)$_r$ supramolecules.

To investigate how the placement of the alkyl solubilizing groups (side- vs. end-functionalization) on the semiconducting core can affect the overall supramolecular assembly, studies were carried out on **6T**-based supramolecules (side-functionalized) and compared to our previous studies on **4T** (end-functionalized) (Figure 4.1).[30,32] Since **4T** and **6T** have similar crystalline cores, we expect that the placement of the solubilizing groups will have the dominant effect on any differences observed in the crystallinity of the SMs. Figure 4.6 shows the DSC thermograms of **6T** and PS-*b*-P4VP(**6T**)$_{1.5}$. During the first heating/cooling cycle of pristine **6T**, a pair of endotherms are observed at 90 °C and 98 °C during heating and an exotherm at 53 °C during cooling (Figure 4.6). Subsequent heating/cooling cycles show similar results. The heat of crystallization of **6T** alone is 27.6 kJ/mol. PS-*b*-P4VP(**6T**)$_{1.5}$ shows a very weak melting peak during heating, but doesn't have a crystallization peak during cooling. This indicates that the crystallization of **6T** is significantly disrupted upon supramolecule formation. In contrast, **4T** and PS-*b*-P4VP(**4T**)$_{1.5}$ have similar peak locations during heating and cooling in DSC.[32] The heat of crystallization of pristine **4T** based off the highest temperature cooling transition is calculated to be 31.8 kJ/mol, and the heat of crystallization of **4T** in PS-*b*-P4VP(**4T**)$_{1.5}$ supramolecules is 24.4 kJ/mol, which corresponds to 77 % crystallinity. Thus, the placement of the alkyl solubilizing groups on the sides of the molecule instead of the end likely disrupts the crystallinity of **6T** within supramolecular assemblies to a much larger extent than **4T**.

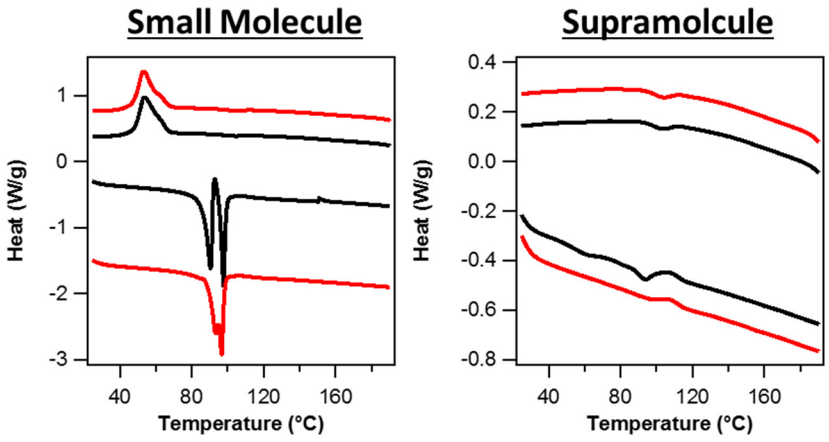

Figure 4.6. DSC curves of (left) **6T** alone and (right) PS-b-P4VP(**6T**)$_{1.5}$ supramolecules. The first heating/cooling cycles are black and the second are red.

TEM was used to investigate how the difference in the strength of intermolecular interactions between **4T** and **6T** affects the assembly of PS-*b*-P4VP(**4T**)$_{1.5}$ and PS-*b*-P4VP(**6T**)$_{1.5}$ supramolecules (Figure 4.7a). Samples were treated under identical conditions as **DOPH** and **DEPH** supramolecules. Figure 4.7a shows a representative TEM image of PS-*b*-P4VP(**6T**)$_{1.5,}$ showing a cylindrical morphology with a relatively small BCP periodicity and small grain sizes. However, TEM images of PS-*b*-P4VP(**4T**)$_{1.5}$ showed a lamellar morphology with a large periodicity and large oriented regions.[32] The weight fraction of the comb block in PS-*b*-P4VP(**6T**)$_{1.5}$ (f_{comb} = 64%) supramolecules is higher than that of PS-*b*-P4VP(**4T**)$_{1.5}$ (f_{comb} = 57%), which may potentially lead to a cylindrical morphology. However, PS-*b*-P4VP(**4T**)$_2$ (f_{comb} = 63%), which has an f_{comb} comparable to PS-*b*-P4VP(**6T**)$_{1.5}$, was prepared and forms a lamellar morphology (See Appendix A.2.1). Therefore, it is likely that the observed differences in morphology between **4T**- and **6T**-based supramolecules, i.e. lamellae for **4T** and cylinders for **6T**, is due to the relatively stronger intermolecular interactions of **4T** compared to **6T**.

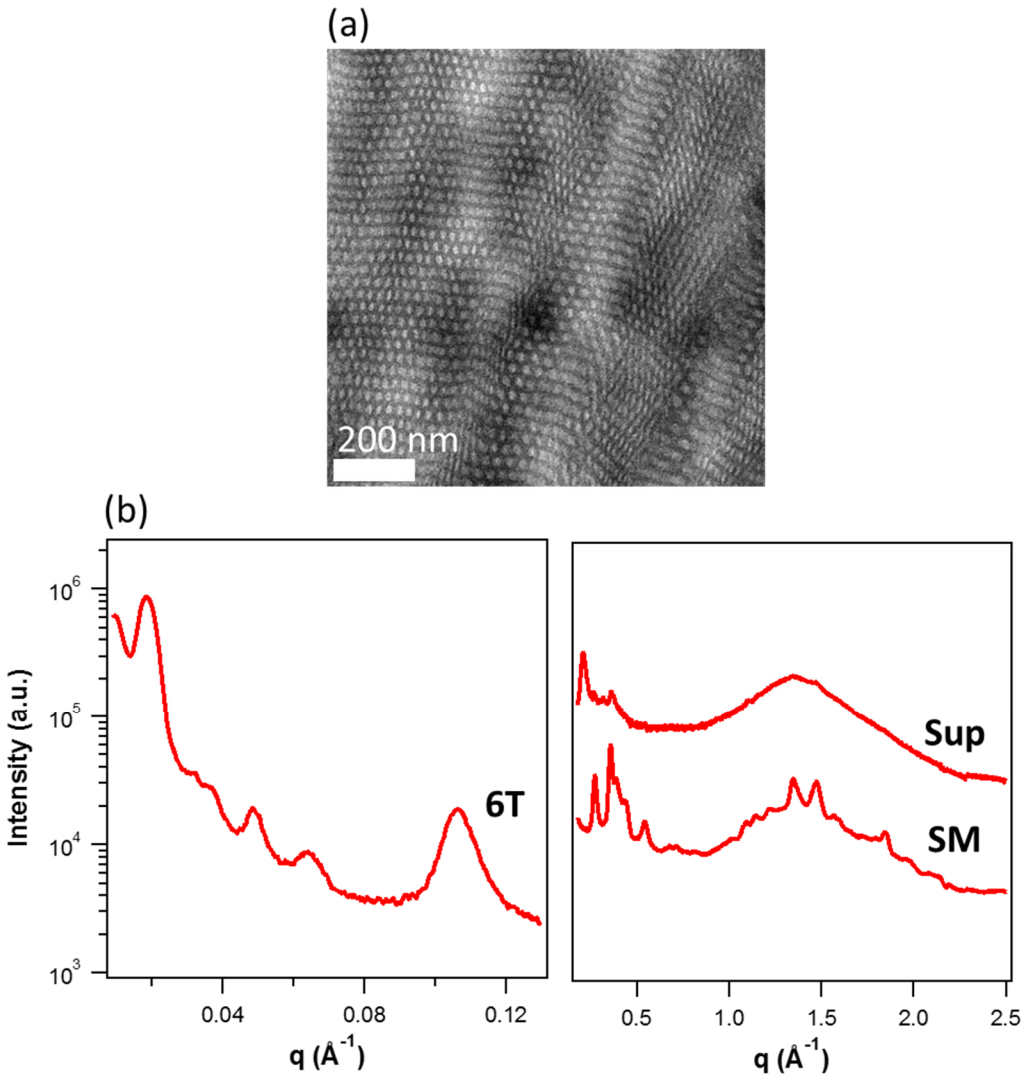

Figure 4.7. (a) TEM image of PS-*b*-P4VP(**6T**)$_{1.5}$ (f_{comb} = 64%) supramolecules. (c) (left) SAXS curves of PS-*b*-P4VP(**6T**)$_{1.5}$ supramolecules. (c) (right) WAXS curves of PS-*b*-P4VP(**6T**)$_{1.5}$ (Sup), and **6T** (SM).

The morphology and packing of these supramolecules and the crystallization of the SMs was further investigated by small-angle X-ray scattering (SAXS) and wide-angle X-ray scattering (WAXS) (Figure 4.7c). The SAXS curve of PS-*b*-P4VP(**6T**)$_{1.5}$ supramolecules has peaks at q = 0.0185, 0.0320, 0.0370, 0.0484, and 0.0644 Å^{-1}, which confirms a well-defined cylindrical morphology of the BCP with a periodicity of ~34 nm. SAXS curves from PS-*b*-P4VP(**4T**)$_{1.5}$ supramolecules showed peaks corresponding to a lamellar morphology with a much larger periodicity (~52 nm).[32] There is also a peak at q = 0.1060 Å^{-1} for PS-*b*-P4VP(**6T**)$_{1.5}$, which indicates a comb lamellae periodicity of ~5.9 nm. However, this peak is less intense and broader than its **4T** counterpart, indicating that the P4VP(**6T**) packing in the supramolecules is not as well-

defined.[32] The WAXS curve of **6T** alone shows a pair of peaks centered at q = 1.349 and 1.475 Å^{-1}, which suggests **6T** forms a herringbone structure. In thermally-annealed PS-*b*-P4VP(**6T**)$_{1.5}$ supramolecules, these peaks mostly disappear, which suggests a significant reduction in crystallinity of **6T** molecules in supramolecular domains, consistent with DSC results.

§ 4.3 Discussion

We have observed that a variety of organic semiconductor SMs can be readily incorporated into BCP-based supramolecules, and their phase behavior can have several effects on the assembly. 1) The incorporation of the SM has a large effect on the interfacial curvature between the two microdomains and consequently, the overall supramolecular morphology. 2) At equivalent weight fractions, the incorporation of different SMs can significantly affect the interfacial curvature between the two microdomains, the morphology, and the packing of the supramolecule. 3) The crystal packing of the SM doesn't necessarily lead to assembly of the comb block within the BCP microdomains. 4) The incorporation of different SMs at similar weight fractions can result in fairly large differences in the overall periodicity of the supramolecules. For example, **DEPH** and **6T** and more readily form morphologies with relatively smaller periodicities and stabilize morphologies with larger interfacial curvature, such as a cylindrical morphology, compared to **DOPH** and **4T**. Additionally, neither **DOPH** nor **DEPH** form well-defined lamellae from the comb block, as would normally be observed for **4T**-, **6T**-, and alkyl-based supramolecules, despite clearly incorporating into the supramolecule. When comparing the molecules investigated, there are a few factors differentiating them. First of all, the supramolecules based on oligothiophenes (**4T** and **6T**) have well-defined internal structure in the comb block. The comb lamellae are better defined for **4T**, which is more crystalline. However, this is not the case for **DOPH** and **DEPH** even though both molecules are crystalline and have much higher melting points than **6T**. For **DOPH** and **DEPH**, the only structural difference is the branched vs. linear alkyl chains. Both have fairly high melting points, but the DSC and WAXS results show substantial differences in crystallinity when incorporated into the supramolecules. We hypothesize that the exact nature of the supramolecular chain packing is critically dependent on the specific packing structure of the SM, which in turn depends on the composition of the crystalline core, the placement (side vs. end-functionalization) of the alkyl solubilizing groups, and constitution (linear vs. branched) of the alkyl groups.

When comparing the two families of supramolecules, we observed that a high crystallinity of the SM leads to straight interfaces between domains, and lamellar morphologies are observed. Whereas low crystallinity SM-based supramolecules show morphologies with curved interfaces. For example, a cylindrical morphology is observed for PS-*b*-P4VP(**6T**)$_r$ at f_{comb} = 64%, and a mixture of lamellae and cylinders are seen for PS-*b*-P4VP(**DEPH**)$_r$ at f_{comb} = 62%. This is supported by the DSC results where the heat of crystallization calculated from the highest temperature peak during cooling for **4T** and **DOPH** decrease by 23% upon forming supramolecules when compared to the neat SMs.[32] In contrast, neither **6T** nor **DEPH** exhibit crystallization peaks during cooling at all upon supramolecule formation. These observations confirm that even though the strength of the intermolecular interactions tend to be believed to be the dominant force toward molecular packing and the overall morphology of the supramolecules, the crystallinity is the key parameter. This is quite reasonable as how the SM packs will directly determine the shape, rigidity of the comb block, the cross-sectional area mismatch between the

comb and coil blocks, and the χ. Together, these parameters determine the phase diagram of the supramolecules. However, it is noted that the packing of the SM doesn't necessarily result in the formation of well-defined comb lamellae, as is evidenced by the absence of scattering peaks corresponding to the comb lamellae for **DOPH**- and **DEPH**-based supramolecules. It is likely that **6T** and **DEPH** are less strongly crystalline than **4T** and **DOPH** due to the placement (end vs. side functionalized) and constitution (linear vs. branched) of their alkyl solubilizing groups, respectively. This may potentially open a viable route to control supramolecular assemblies by controlling the crystallization kinetics during the sample treatment, though the SM organic semiconductors tend to have fast kinetics. Present studies show that the crystallinity of the SM can be modulated by its chemical structure.

However, the crystallinity alone does not fully explain the non-uniform interface between the lamellar blocks observed in PS-*b*-P4VP(**DOPH**)$_{1.5}$ and PS-*b*-P4VP(**DOPH**)$_1$ and the mixture of cylindrical and lamellar morphologies seen in PS-*b*-P4VP(**DEPH**)$_{1.5}$. In previous studies of PS-*b*-P4VP(**4T**)$_{1.5}$, the crystallization of **4T** led to a significant deformation of the PS coil block in addition to stretching the P4VP backbone that the SMs were directly attached to.[32] From detailed TEM image analyses of PS-*b*-P4VP(**DOPH**)$_{1.5}$ and PS-*b*-P4VP(**DOPH**)$_1$, we can clearly see that the **DOPH** distribution is not homogeneous, and there are two distinct regions with clear variations in the widths of the PS and P4VP(**DOPH**) blocks, referred to here as type 1 and 2 (Figure 4.8). Linecuts of the small (type 1) and large (type 2) periodicity domains of PS-*b*-P4VP(**DOPH**)$_{1.5}$ are shown in Figure 4.8a–d. In the type 1 domains (boxed region of Figure 4.8a), the PS blocks are relatively larger while the P4VP(**DOPH**) comb blocks are smaller, and the overall periodicity is smaller compared to the type 2 domains (boxed region of Figure 4.8c). The P4VP(**4T**) blocks contribute only ~29% of the overall periodicity in type 1 domains, while in type 2 domains, they contribute ~70%. The comb domains in type 2 are similar in length to twice the contour length of the 5600 Da P4VP chain (~27 nm), which indicates that the P4VP chains are fully or nearly fully stretched in these parts of the sample. In type 1 domains, the **DOPH** molecules are most likely less abundant and in an amorphous state and do not stretch the polymer chains along the c-axis or compress them along the a- and b-axes to a large extent (Figure 4.8e). In type 2 domains, the **DOPH** molecules are more abundant and crystalline and do stretch the polymer chains along the c-axis and compress them along the a- and b-axes. A similar analysis of PS-*b*-P4VP(**DOPH**)$_1$ TEM images supports these conclusions. It was found that the comb block constitutes a similar portion of the overall periodicity in the type 1 domains (~28% comb). However, in the type 2 areas of the sample, the PS domains are relatively larger, and the comb domains are smaller compared to PS-*b*-P4VP(**DOPH**)$_{1.5}$. In these regions, ~64% of the periodicity comes from the comb block, which is ~6% less compared to r = 1.5. Since the only difference between these two samples is the loading rate of SMs, we speculate that the expansion of the P4VP(**DOPH**) block and the decrease in size of the PS block is the result of the amount and molecular packing of **DOPH** molecules in the supramolecules.

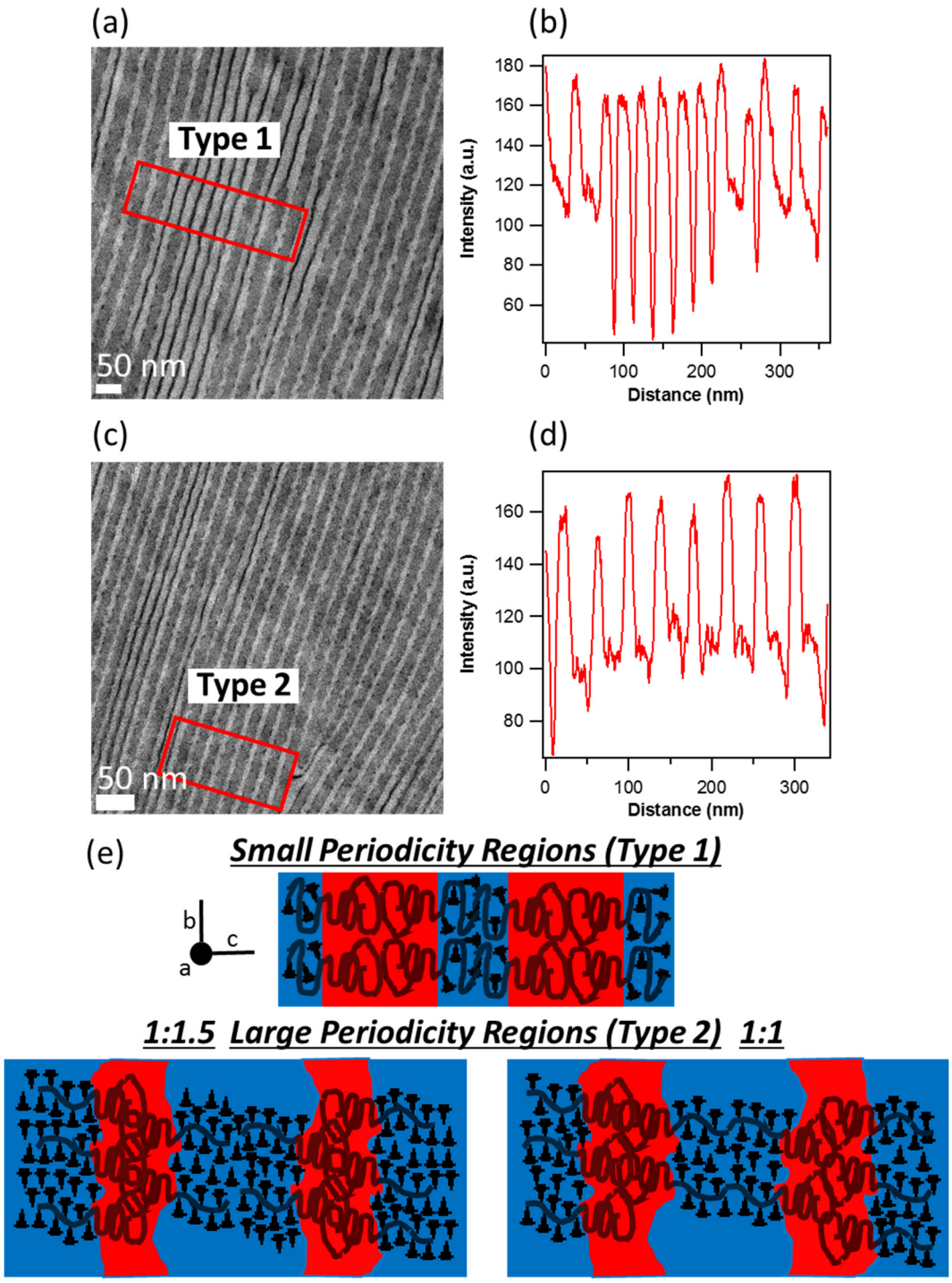

Figure 4.8. (a, c) TEM images and (b, d) linecuts of TEM images of PS-*b*-P4VP(**DOPH**)$_{1.5}$ supramolecules. The red boxes on the TEM images on the left show the location and bandwidth of the linecuts on the right and highlight a primarily (a) small periodicity region (type 1) and (c) a large periodicity region (type 2). (e) Schematic drawings of the proposed supramolecular packing structures in the small and large periodicity domains of PS-*b*-P4VP(**DOPH**)$_r$ (r = 1.5 and 1).

As discussed in our previous studies of PS-*b*-P4VP(**4T**)$_{1.5}$, the entropic cost for deforming the polymer chain is offset by the enthalpically favorable crystallization of the SM.[32] However, polymer chain stretching of this type does not account for the fact that the thickness of the PS blocks are smaller in the type 2 domains (~12 nm), which have a larger overall periodicity, compared to the type 1 areas (~18 nm). This is in contrast to the trend observed in **4T**-based supramolecules where the both the P4VP and PS blocks are expanded during crystallization along the c-axis.

To explain these observations in the type 2 domains, possible packing structures for PS-*b*-P4VP(**DOPH**)$_{1.5}$ and PS-*b*-P4VP(**4T**)$_1$ are proposed in Figure 4.8e. In these schematics, the PS coil blocks are interdigitated within their lamellar domains, and the comb block packing is irregular. The interdigitation of the PS blocks could account for the decreased size of the PS microdomains since the gaps it would form would most likely be filled with **DOPH** molecules, which would make these filled-in gaps appear darker in TEM images. This would also explain the observed fluctuations of the interface between the PS and comb blocks. This packing structure is mostly likely favored due to the cross-sectional area mismatch between the crystallized P4VP(**DOPH**)$_r$ blocks and the natural packing of the coil-like PS blocks. This effect is less pronounced for the r = 1 sample (Figure 4.8e). These supramolecules do not form regular, well-defined comb lamellae, as is suggested by the lack of peaks corresponding to these structures in the X-ray scattering studies. While the exact crystal structure of **DOPH** is not known, the fact that these structures have not been observed in **4T**-based supramolecules indicates that it is very likely that these effects are due to the molecular packing of **DOPH**.[73,74] This is corroborated by the fact that these supramolecular packing effects are less obvious for the r = 1 sample.

Since **DEPH** most likely adopts a similar packing structure as **DOPH**, it is possible that PS-*b*-P4VP(**DEPH**)$_{1.5}$ adopts a similar packing structure as discussed for PS-*b*-P4VP(**DOPH**)$_r$. However, since **DEPH** does not crystallize as strongly during cooling, the effects of the SM packing on PS-*b*-P4VP(**DEPH**)$_{1.5}$ are not as obvious as for PS-*b*-P4VP(**DOPH**)$_r$, and PS-*b*-P4VP(**DEPH**)$_{1.5}$ also more readily adopts complete cylindrical morphologies rather than lamellae with an undulating interface.

§ 4.4 Conclusion

In conclusion, we have demonstrated how the phase behavior of the SMs during cooling is critically important to the overall assembly of organic semiconductor-based supramolecules. First, the incorporation of SMs has a large effect on the interfacial curvature between the microdomains in the overall supramolecular morphology. Second, at equivalent weight fractions, the incorporation of different SMs can affect the interfacial curvature between the two microdomains, the overall morphology, and the packing of the supramolecule. Specifically, morphologies with a high degree of curvature, such as cylinders, are less favorable for supramolecules based on more crystalline SMs. Third, the crystal packing of the SM doesn't necessarily lead to the assembly of the comb block within the BCP microdomains, as is normally observed for other supramolecules. Fourth, the incorporation of different SMs at similar weight fractions can cause significant differences in the overall periodicity of the supramolecules. The crystallinity and packing of the SMs can be tailored by changing the crystalline core as well as the attachment site(s) (side- vs. end-functionalization) and the constitution (branched vs. linear) of the alkyl solubilizing group(s).

Since the composition of the components of the SMs are modular, these studies provide useful guidance toward tailoring the assembly of optically active and semiconducting supramolecules.

§ 4.5 Experimental section

4.5.1 Materials

PS(40,000 Da)-*b*-P4VP(5,600 Da) (PDI = 1.09) was purchased from Polymer Source, Inc. Chloroform was purchased from Fisher or Aldrich and filtered through basic alumina. All other chemicals were purchased from Aldrich and used as received. The synthetic procedures for **6T**, **DEpH**, and **DOpH** will be described in a future publication. The synthetic procedure to prepare **4T** is described in detail in a previous publication.[30]

4.5.2 Sample Preparation

The small molecules are light- and oxygen-sensitive so samples were either prepared in an argon glovebox or cautions were paid to avoid light exposure during the sample preparation process. The PS-*b*-P4VP was first dissolved in chloroform to form 1% (w/v) stock solutions. The desired amount of the small molecules was dissolved in chloroform. The polymer solution was then added to the organic semiconductor solution, followed by stirring overnight. Solutions were then transferred into PTFE beakers under a covered dish, and solvent was allowed to slowly evaporate for 24 h. Samples were then placed in a vacuum oven at room temperature for 8 h to remove residual solvent. Bulk samples were collected from the beakers, and portions were put into DSC pans, annealed at various temperatures in a vacuum oven overnight, and slowly cooled to room temperature.

4.5.3 Small-Angle and Wide-Angle X-ray Scattering (SAXS/WAXS)

The SAXS and WAXS data were collected on beamline 7.3.3 in the Advanced Light Source (ALS) at the Lawrence Berkeley National Laboratory and beamline 8-ID-E in the Advanced Photon Source (APS) at Argonne National Laboratory. X-rays, with a wavelength of 1.240 Å (10 KeV) and 1.712 Å (7.24 KeV) were used, and the scattering spectra were collected on a Pilatus 1M detector. The scattering profiles, after a 60 s collection time, were obtained by integrating the 2-D scattering pattern. Line-averaged intensities are reported as I vs. q, where $q = (4\pi/\lambda)*\sin(\theta/2)$, λ is the wavelength of incident x-rays and θ is the scattering angle. Data was analyzed with Nika 1 (http://usaxs.xray.aps.anl.gov/staff/ilavsky/nika.html),[75] an analysis program designed for Igor Pro (WaveMetrics, Lake Oswego, OR, USA).

4.5.4 Transmission Electron Microscopy (TEM)

The same samples used for SAXS/WAXS were embedded in resin and cured at 60 °C overnight before being microtomed for TEM imaging. The thin sections of PS-*b*-P4VP(**SM**)$_r$ were exposed to iodine vapor for 10 min that selectively stains the P4VP(**SM**)$_r$ block to enhance the contrast. TEM images were collected on an FEI Tecnai 12 transmission electron microscope at an accelerating voltage of 120 kV. Image analysis was performed using ImageJ (http://rsbweb.nih.gov/ij/).[76]

4.5.5 Differential Scanning Calorimetry (DSC)

The DSC thermograms were collected on a TA Q200 DSC with an RCS 40 refrigeration unit. The neat small molecule and supramolecule samples were heated and cooled from 0 °C – 200 °C – 0 °C for two cycles at a rate of 10 °C/min.

Chapter 5
Organic Semiconductor-Based Supramolecular Nanocomposites

Functional organic-inorganic nanocomposites have the potential to combine the advantages of both organic and inorganic materials, however, it is often necessary to precisely control their morphology and packing for their application in a number of devices. Non-functional block copolymers (BCP) and BCP-based supramolecules have been studied as structural frameworks for the assembly of inorganic nanoparticles (NPs), while comparatively less work has been done on highly crystalline, functional organic frameworks. In the previous chapters, we investigated how the crystallinity and packing of the small molecules (SMs) affects the assembly and properties of organic semiconductor-based supramolecules. Here, we investigate how the SM phase behavior as well as the loading rate and size of the NPs can affect their coassembly in supramolecular frameworks. The NPs can be incorporated into the supramolecular microdomains even from a macrophase-separated state. The strong crystallization of the SMs tends to force the NPs into less crystalline domains of the comb block, where the oligothiophenes are less abundant. The introduction of the NPs also decreases the BCP periodicity of the supramolecules. The larger NPs favor assembly in the center of the comb domains, parallel to the BCP lamellar axis, to minimize the entropic penalty of deforming the polymer chain, while the smaller particles assemble into rows in between the comb lamellae, perpendicular to the axis of the BCP lamellae. The assembly of nanocomposites based on highly crystalline SMs is found to be distinct from both supramolecular nanocomposites based on less crystalline SMs and supramolecules based on highly crystalline SMs without NPs. However, nanostructured arrays of organic and inorganic semiconductors can still be readily obtained. These studies present a versatile method for the coassembly of highly crystalline, functional SMs with NPs for the fabrication of nanocomposite devices.

§ 5.1 Introduction

Organic-inorganic nanocomposites can potentially combine the advantages of both organic and inorganic materials. Inorganic nanoparticles (NPs) can display size-dependent optical and electronic properties with high extinction coefficients and relatively high charge mobilities and have seen extensive use in photovoltaic (PV) and biomedical applications.[1,2] However, it is often desirable to interface these NPs with other materials and assemble them into well-defined arrays for some device applications.

Block copolymers (BCPs) assemble into an array nanostructured morphologies with features similar in size to NPs. Hybrid nanocomposites can be fabricated using BCPs as a nanoscopic template for the assembly of various NPs into well-defined arrays that are scalable and amenable to solution processing.[3] There have been extensive experimental and theoretical studies on the blends of BCPs and NPs, and a number of critical parameters have been identified that govern their assembly, including the enthalpic interactions between the NP ligands and each BCP microdomain and the entropic penalty for deforming the polymer chain when the NPs are incorporated.[4] The enthalpic interaction between the NPs and polymers can be tailored by exchanging the NP ligands.[3,5-7] By using polymeric ligands that match one block of the BCP, the assembly of the NPs can be selectively sequestered into that microdomain by favorable van der Waals interactions.[8-11] The use of stronger interactions, such as electrostatic interactions and hydrogen bonding, can enhance the solubility of the NPs in the polymer matrix and increase the maximum weight fraction of NPs before the onset of macrophase separation.[12,13] For neutral

ligands, NPs that are small relative to the domain size of the BCP have been shown to favor assembly at the interface between the two microdomains, while larger particles tend to assemble in the center of domains to minimize the entropic penalty for deforming the polymer chain.[14-19]

BCP-based supramolecules can be constructed by attaching small molecules (SMs) to one or more blocks of a BCP via secondary interactions, such as hydrogen bonding, electrostatic interactions, or metal ligation.[20-23] When SMs are attached to one block of coil-coil BCPs, they form coil-comblike supramolecules. By utilizing SMs that also have favorable interactions with the ligands on the NPs, the polymer-NP interactions can be tailored.[24] By this method, a variety of inorganic NP compositions (metallic, semiconducting, etc) and shapes (spheres, rods) have been assembled.[24-28] In coil-comblike supramolecules, the entropic penalty for deforming the comb block is higher compared to coil-coil BCPs, which can force the NPs to assemble into different localized regions of the comb block depending on the NP size and aspect ratio.[26,28] These supramolecular nanocomposites have also been used to form luminescent microspheres.[29] While some preliminary studies of supramolecular nanocomposites based on highly crystalline SMs, such as organic semiconductors, have been reported, a more thorough investigation is necessary to better understand how the phase behavior of the SM affects the NP assembly.[30]

Nanocomposites that contain a functional, highly crystalline organic component, such as conjugated polymers, have the potential to combine the advantages of functional organic and inorganic materials in a number of devices. In blends of conjugated polymers and NPs, nanostructures are typically formed by spontaneous phase separation of the two materials.[31] Since this technique does not form well-defined arrays of the organic and inorganic components, desirable for many applications, a number of techniques to optimize the morphology have been developed. One method is to use BCPs that contain a semiconducting block and another block that interacts favorably with NPs. To this end, a number of semiconducting moieties have seen use, including poly(fluorene)[32] and tetraphenylbenzidine side groups.[33] A number of NP binding blocks have also been used, including polydimethylaminoethyl methacrylate[32] and poly(4-vinylpyridine) (P4VP).[33] In one example, a rod-rod conjugated BCP, poly(3-hexylthiophene)(P3HT)-*block*-poly(3-hexylselenophene), was used to control the assembly of CdSe NPs by favorable interactions between the NPs and P3HT.[34] Another technique is to coassemble the NPs with conjugated polymer nanowires. Coassemblies of P3HT nanowires and CdSe dots have been fabricated from favorable interactions between the CdSe NPs and the sulfur atoms on P3HT.[35,36] One method to improve the electron coupling and interfaces among the different components in these systems is to directly attach SM organic semiconductors or conjugated polymers as NP ligands.[37-39] By combining the nanowire assembly and semiconducting ligand techniques, spherical and rodlike CdSe NPs functionalized with P3HT ligands were cocrystallized with P3HT nanowires to form hybrid nanowires.[40,41]

As mentioned, precisely-controlled arrays of NPs can be readily achieved using supramolecules based on BCPs and non-functional SMs, however the organic component only provides a structural framework for the NP assembly but not inherent functionality. While well-defined arrays of organic semiconductor SM-based supramolecules without NPs can also be fabricated, the crystallinity and packing of the SM plays a critical role in the assembly process and the resulting morphology.[42,43] Here, we synergize the self-assembly processes in a three component nanocomposite material that contains BCPs, highly crystalline SM organic semiconductors, and NPs. We blend oligothiophene semiconductor-based supramolecules with semiconducting NPs to investigate how the crystallinity of the SM and the size of the NPs affects

the thermodynamics and kinetics of the assembly process in bulk. After solvent casting, the SMs and NPs coassemble, but primarily macrophase separate from the BCP. After thermal annealing below the T_m of the SM, more of the SMs and NPs incorporate into the BCP microdomains, and when thermally annealed near or above the T_m of the SM, nanoscopic arrays of oligothiophenes and NPs are achieved. Structurally, these blends are distinct from organic semiconductor-based supramolecules alone and NP blends with less crystalline supramolecules. The assemblies contain two primary domains: one that contains less SMs but favors NP assembly and another that is SM-rich but tends to exclude the NPs. The assembly of the NPs also depends on the size of the NPs. Larger NPs (~6 nm) tend to assemble single file in the center of the of the comb domains, while smaller particles (~3 nm) favor assembly in rows intercalated between the supramolecular chains, perpendicular to the axis of the BCP microdomains.

§ 5.2 Results

5'''-(3,7-Dimethyloctyl)-5-(3-(3-hydroxyphenyl)propyl)-[2,2';5',2'';5'',2''']quaterthiophene, identified as "**4T**," was designed to hydrogen bond with the 4-vinylpyridine repeat units of a polystyrene(40 kDa)-*block*-poly(4-vinylpyridine)(5.6 kDa) (PS-*b*-P4VP) BCP to form a supramolecule, identified as PS-*b*-P4VP(**4T**)$_r$ (Figure 5.1). The ratio of SMs to 4VP groups is $r = 1.5$. **4T** was synthesized by Clayton Mauldin and David Hanifi, and its synthesis was reported in a previous publication.[42] PbS[44] (~6 nm) and CdSe[45] (~3 nm) NPs were synthesized by Peter Bai and Noah Bronstein using previously reported procedures and were passivated with oleylamine and trioctylphosphine ligands, respectively.

4T was designed with three primary components, i.e. a phenolic moiety to construct the supramolecule, a crystalline oligothiophene semiconducting core, and an alkyl group to enhance its solubility. This alkyl moiety also has favorable van der Waals interactions with the alkyl and alkenyl groups present in inorganic NP solubilizing ligands. Supramolecules based on alkyl-containing SMs have been used to take advantage of this favorable interaction and were shown to form well-ordered assemblies of NPs.[24] However, all of these supramolecules were based on SMs that have relatively weak intermolecular interactions and do not have inherent optical or electronic properties. For many device applications, such as organic PVs (OPVs) or light-emitting diodes (LEDs), it is desirable to interface complementary electronic materials into well-defined, nanostructured assemblies, and it is possible that blends of organic semiconductor-based supramolecules with NPs may be able to achieve these ideal nanostructured morphologies (Figure 5.1). However, recent publications have shown how the crystallinity and packing of the SM is critical to the overall assembly of the supramolecules.[43] Thus, it follows that their crystallinity will also play a large role in the assembly in their blends with NPs.

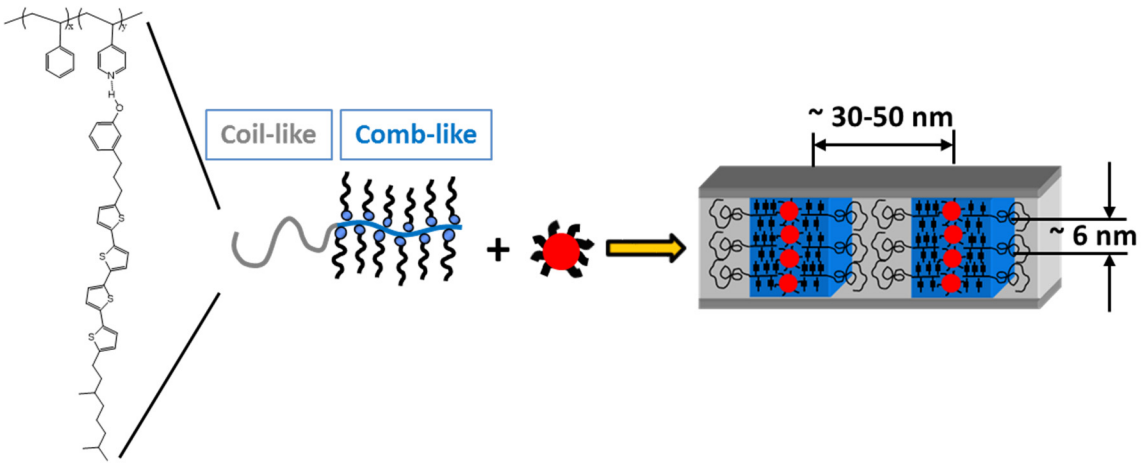

Figure 5.1. (left) Chemical structure of PS-b-P4VP(**4T**) supramolecules. (center, right) Idealized schematic drawing of supramolecules blended with NPs.

To understand the kinetics of the self-assembly process during annealing in bulk, PS-*b*-P4VP(**4T**)$_{1.5}$ supramolecules blended with 11 wt%, 6 nm PbS NPs (PbS-6nm11%) were annealed below, near, and above the T_m of **4T** and studied using transmission electron microscopy (TEM), small-angle X-ray scattering (SAXS), and wide-angle X-ray scattering (WAXS). The samples were all annealed overnight and then slowly cooled to room temperature over several hours. TEM images of these samples are shown in Figure 5.2a–d. The samples were not stained, but the more electron dense P4VP(**4T**) regions appear darker compared to the PS domains. The samples annealed below the T_m of **4T** (100–120 °C) show that the particles are dispersed (i.e. no large-scale macrophase separation) but are not well aligned within the supramolecular microdomains. In the sample annealed near the T_m of **4T** (140 °C), the particles have better alignment within the supramolecules, but are not very evenly distributed throughout the sample. When the blends are annealed above the T_m of **4T** (160 °C), the particles are fairly well aligned and more evenly distributed throughout the sample. Since the alkyl NP ligands have favorable interactions with the alkyl moieties of the SMs, and the distribution of the NPs is similar to the distribution of **4T** in PS-*b*-P4VP(**4T**)$_{1.5}$ supramolecules without NPs when annealed at the same temperatures,[43] it is highly probable that the NPs primarily coassemble with the **4T** molecules.

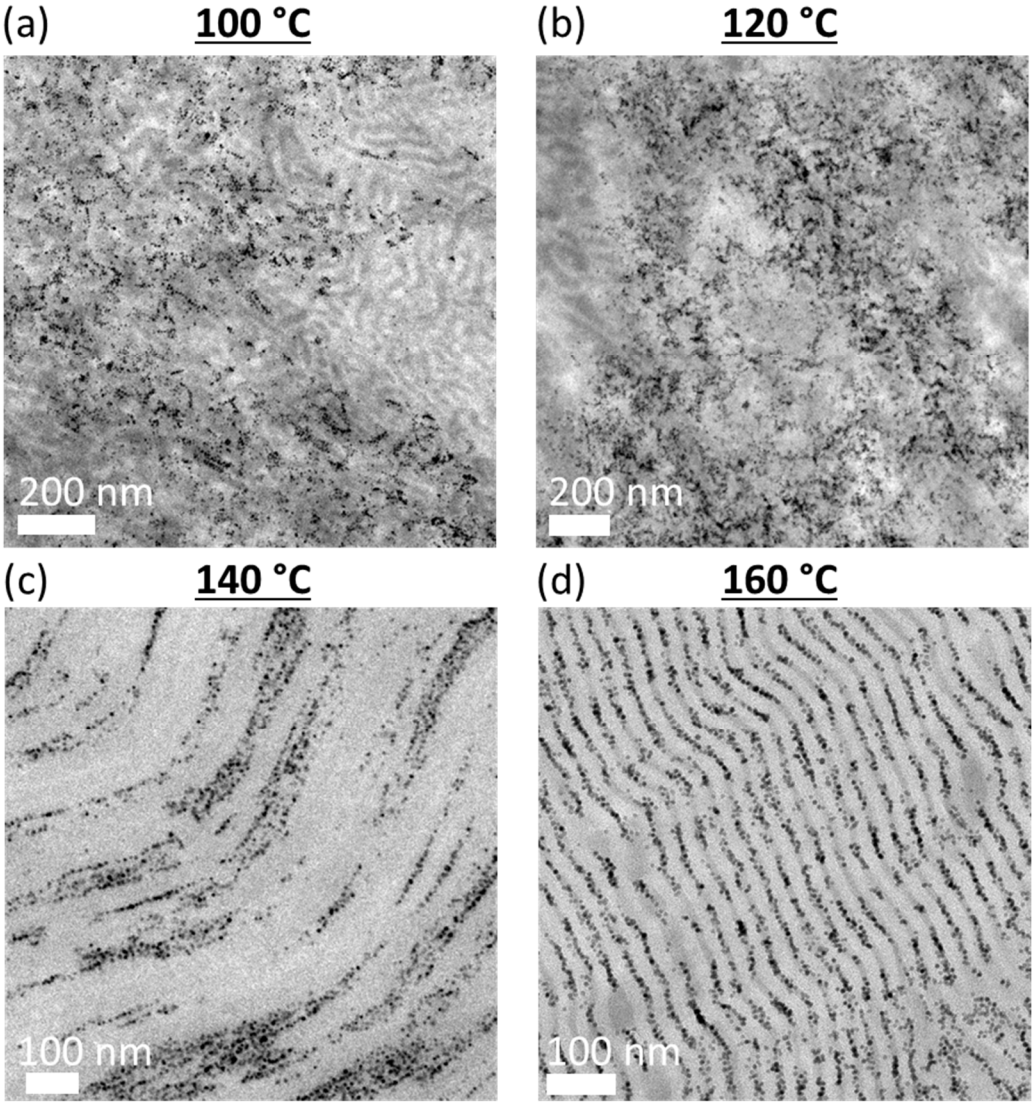

Figure 5.2. TEM images of PS-b-P4VP(**4T**)$_{1.5}$ supramolecules blended with PbS-6nm11% NPs annealed at various temperatures. It is likely that the NPs coassemble with the **4T** molecules. (a, b) The 100/120 °C samples show that the particles are dispersed (i.e. no large-scale macrophase separation) but not well aligned. (c) In the 140 °C sample, the particles are better aligned, but are not very evenly distributed throughout the sample. (d) In the 160 °C sample, the particles are fairly well aligned and more evenly distributed throughout the sample.

The SAXS and WAXS curves of PS-b-P4VP(**4T**)$_{1.5}$ supramolecules blended with PbS-6nm11% NPs after annealing at various temperatures are shown in Figure 5.3. In the 40 °C sample, the **4T** molecules are primarily macrophase separated from the polymer, much like PS-b-P4VP(**4T**)$_{1.5}$ supramolecules without NPs.[43] In its SAXS profile, peaks at $q \sim 0.02563$ and 0.07786 Å^{-1} indicate a BCP periodicity of ~25 nm and a interparticle spacing of 8.1 nm. A pair of diffraction

peaks at q ~ 0.1117 and 0.2229 indicates a lamellar periodicity of 5.6 nm, corresponding to macrophase separated **4T** molecules. When the sample is annealed at 100 °C, these peaks sharpen and peaks at q ~ 0.09913, 0.1988, and 0.2974 Å^{-1} appear, corresponding to **4T** molecules incorporated into the P4VP(**4T**) comb block with a lamellar periodicity of 6.3 nm. Samples annealed at or above 120 °C have a much larger BCP periodicity of ~47 nm, which is a result of most of the **4T** molecules incorporating into the supramolecules. The observed trend of the SMs partially incorporating into the comb block when annealed below the T_m of **4T** and mostly incorporating when annealed near or above the T_m is similar to supramolecules without particles.[43] The interparticle spacing also increases from ~8.1 nm to ~9.2 nm after annealing. In the WAXS profile of the 40 °C-annealed sample, there are peaks at q ~ 1.29 and 1.38 Å^{-1}, similar to that of **4T** alone. Upon annealing between 100–160 °C, these peaks broaden and converge into a single peak centered at q ~ 1.331 Å^{-1} (4.7 Å^{-1}). This broadening is most likely due to a decrease in **4T** crystal size upon incorporation into the supramolecule. Although this peak is present for all of the annealing conditions, it is higher in intensity for the sample annealed at 160 °C. The peaks observed at q ~ 1.827 and 2.116 Å^{-1} correspond to the (111) and (200) reflections of the PbS lattice.

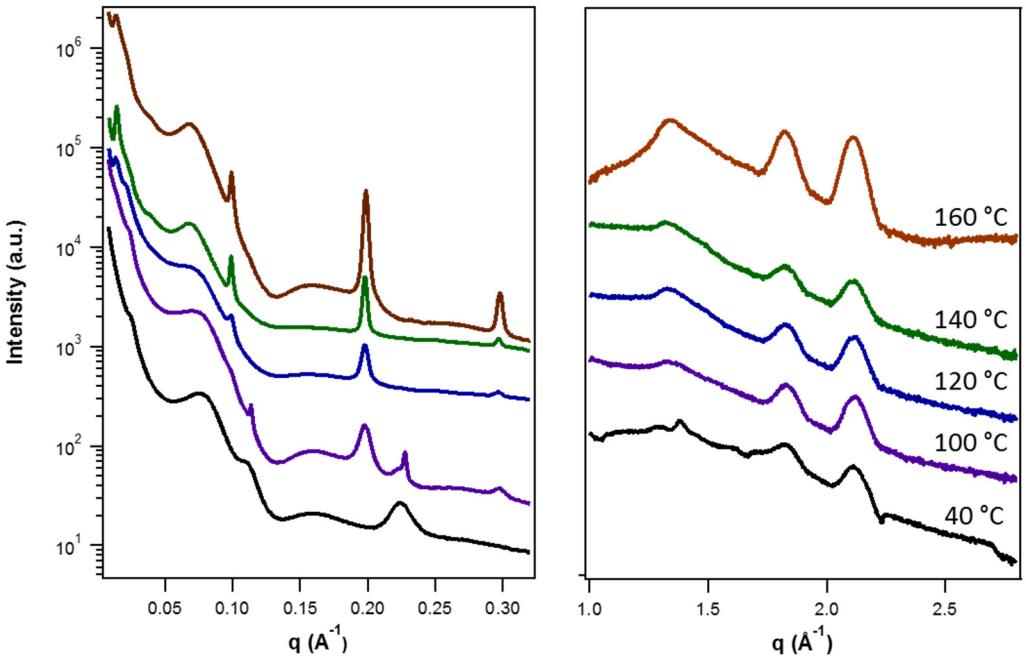

Figure 5.3. (left) SAXS and (left) WAXS curves of PS-b-P4VP(**4T**)$_{1.5}$ supramolecules blended with PbS-6nm11% NPs annealed at various temperatures. (left) Initially, the **4T** molecules primarily macrophase separate from the polymer. The SMs partially incorporate into the comb block when the samples are annealed below the T_m of **4T** and mostly incorporate when annealed near or above the T_m. The macrophase separated and incorporated **4T** molecules have periodicities of ~5.5 nm and ~6.3 nm, respectively. Samples annealed at or above 120 °C have a much larger BCP periodicity (~25 nm vs. ~47 nm). The interparticle spacing increases from ~8.1 nm to ~9.2 nm after annealing. (right) The WAXS curves show peaks corresponding to the molecular packing of **4T**, with a periodicity of ~4.7 Å, and the (111) and (200) lattice reflections from the PbS particles.

TEM was used to more closely investigate how the addition of PbS-6nm11% NPs affects the assembly of PS-*b*-P4VP(**4T**)$_{1.5}$ compared to the supramolecules alone (Figure 5.4). Both samples were annealed at 160 °C, which is above the T_m of all the components in the system. Thin sections of the supramolecule-only sample were stained with iodine, which selectively darkens the P4VP and **4T** domains, to enhance the contrast. Again, the NP-containing samples were not stained. The TEM image in Figure 5.4a shows PS-*b*-P4VP(**4T**)$_{1.5}$ supramolecules alone with a uniform lamellar morphology. While there are a number of local defects, the lamellar domains form large, oriented grains. The PS and P4VP(**4T**) microdomains are approximately equal in thickness (~25–26 nm) and are relatively uniform throughout the sample. However, this uniformity is not maintained for PS-*b*-P4VP(**4T**)$_{1.5}$ supramolecules when blended with PbS-6nm11% (Figure 5.4b). Two major regions are observed, one with thicker comb domains and one with thinner ones. The thicker comb domains (type 2) likely have larger P4VP(**4T**) crystals (~22–34 nm in periodicity), but tend to exclude NPs. The thinner domains (type 1) most likely have smaller P4VP(**4T**) crystals (~8–12 nm in periodicity), but favor NP assembly. However, some particles are observed in the thicker domains as well. In both cases, particles favor assembling in lines at the center of the P4VP(**4T**) domains. The periodicity of the PS domains are fairly uniform throughout the sample (~18–21 nm) and don't appear to depend on the thickness of the comb block. Since these effects are not observed for supramolecules alone, it is highly likely that they are due to the interactions between the supramolecules and the NPs. However, this sample only represents one NP size and loading rate, and previous work has demonstrated that both of these factors can play a role in the NP assembly in BCP-based supramolecules.[28]

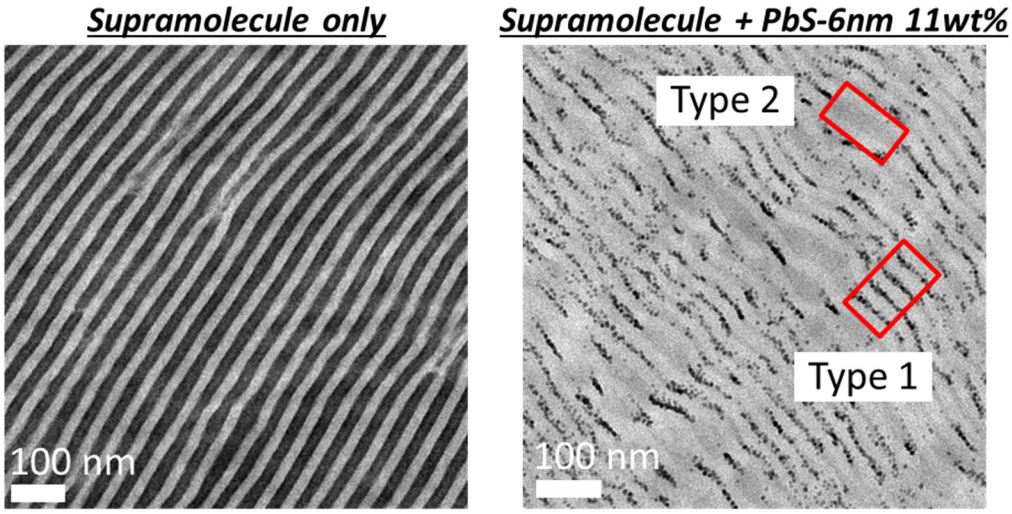

Figure 5.4. TEM images of PS-b-P4VP(**4T**)$_{1.5}$ supramolecules (a) alone and (b) in blends with PbS NPs annealed at 160 °C. The "thicker" (type 2) comb domains in (b) have large P4VP(**4T**) crystals (~22–34 nm in periodicity), but tend to exclude NPs. The "thinner" (type 1) domains have smaller P4VP(**4T**) crystals (~8–12 nm in periodicity), but favor NP assembly. In both cases, the PS domains are ~18–21 nm.

To investigate how the NP size and loading rate may affect the supramolecule and NP assembly in semiconducting supramolecules, PS-*b*-P4VP(**4T**)$_{1.5}$ was blended with PbS-6nm at 10 and 20 wt% as well as 3 nm CdSe at 8 and 16 wt% (CdSe-3nm8/16%). PbS-6nm10% and CdSe-3nm8% both correspond to ~1.4 vol% NP loading, and PbS-6nm20% and CdSe-3nm16% correspond to ~3.2 vol%. The samples were all annealed at 150 °C. Since the NPs are capped with similar alkyl ligands, the inorganic core materials used (CdSe vs PbS) should not have a significant effect on the assembly process.[24] The TEM images of PbS-6nm 10 and 20 wt% show morphologies similar to PbS-6nm11% (Figure 5.5a, b), where lines of NPs favor the smaller P4VP(**4T**) domains (type 1), and the comb domains without particles (type 2) tend to be larger. These morphologies are depicted in the schematic shown in Figure 5.5c. Increasing the NP loading from 10 to 20 wt% increases the density of NPs and qualitatively, the number of defects in the lamellar morphology. The TEM images of PS-*b*-P4VP(**4T**)$_{1.5}$ blended with CdSe-3nm show that the NP assembly is distinct from PbS-6nm-based composites (Figure 5.5d, e). While PbS-6nm NPs tend assemble at the center of the P4VP(**4T**) domains, CdSe-3nm tends to assemble in between the comb lamellae (Figure 5.5c, f). However, much like PbS-6nm samples, the NPs tend to assemble into the narrower comb domains. For CdSe-3nm8%, the thinner regions are ~11–15 nm, which is in a similar range as PbS-6nm samples (8–16 nm). Also like PbS-6nm samples, the thicker comb domains are ~20–24 nm, and the PS domains are ~16–23 nm in both regions. The morphologies observed for CdSe-3nm16% are similar to 8%, however, there are very few thicker comb regions. Almost all of the comb domains are smaller (~12–15 nm) even when NPs are not present in a particular area. The PS domains are also smaller (~12–17 nm) throughout most of the sample.

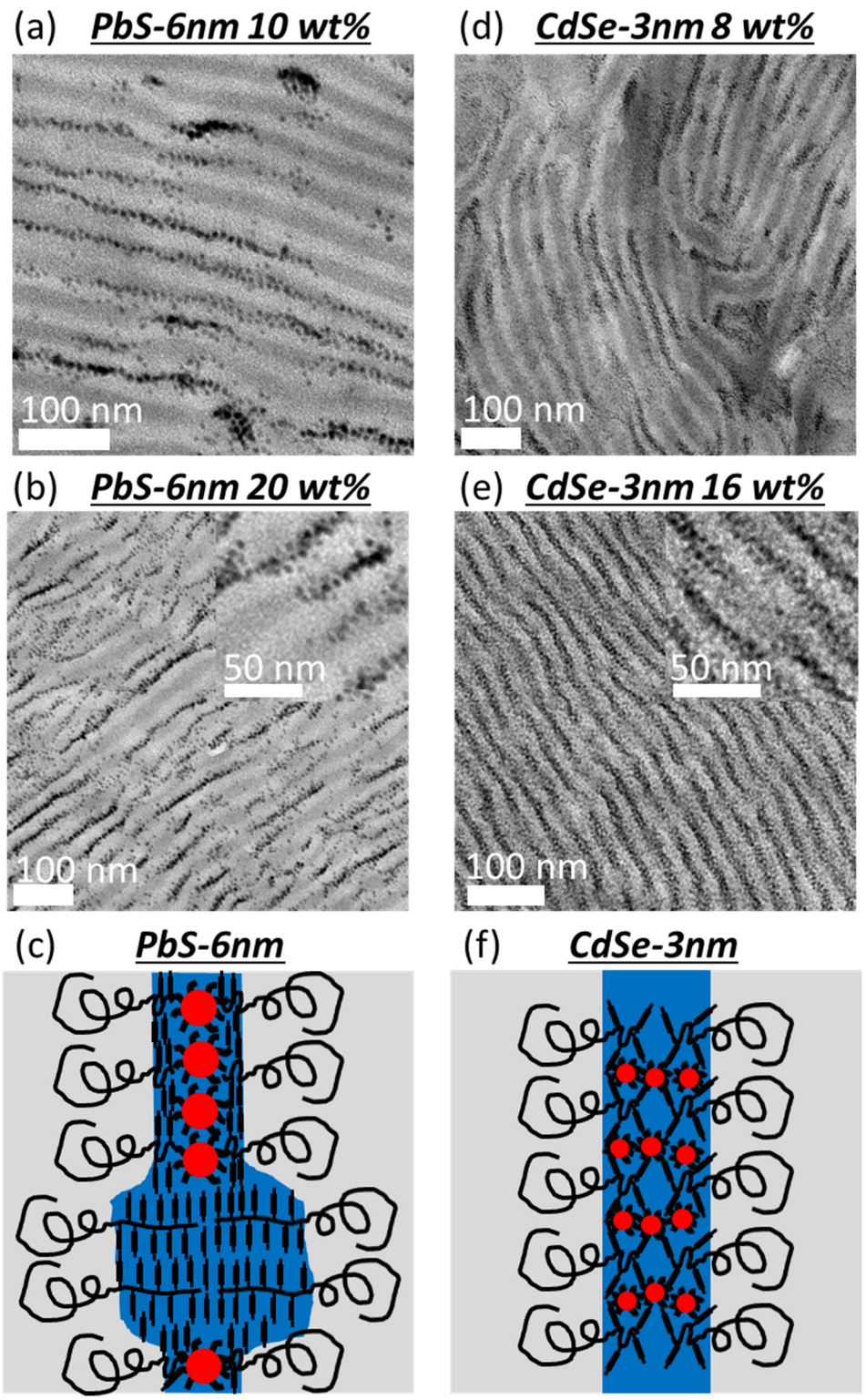

Figure 5.5. NP size and loading rate dependence for samples annealed at 150 °C. TEM images of PS-b-P4VP(**4T**)$_{1.5}$ supramolecules in blends with (a) 10 and (b) 20 wt% PbS-6nm NPs. TEM

images of PS-b-P4VP(**4T**)$_{1.5}$ supramolecules in blends with (d) 8 and (e) 16 wt% CdSe-3nm NPs. (c, f) Schematic cartoons illustrating the two main domains observed in the comb block that are observed in the TEM images of samples annealed at 150–160 °C. The "thicker" comb domains (type 2) have large P4VP(**4T)** crystals, but tend to exclude NPs. The "thinner" domains (type 1) have smaller P4VP(**4T**) crystals, but favor NP assembly. (c) The larger (PbS-6nm) NPs favor assembly in the center of the comb block, but (f) the smaller (CdSe-3nm) NPs tend to assemble in between the comb lamellae.

SAXS and WAXS were used to probe the structure and packing of the supramolecular nanocomposites (Figure 5.6). Since there is a greater electron density difference between PbS/CdSe and PS-*b*-P4VP(**4T**) than between PS and P4VP(**4T**), the peaks in the low q range that would normally correspond to the periodicity of the BCP microdomains likely reflect the spatial distribution of the NPs. In previous studies, PS-*b*-P4VP(**4T**)$_{1.5}$ supramolecules without NPs annealed at 140–160 °C formed lamellae-within-lamellae morphologies with a BCP periodicity of ~52 nm and a comb lamellae periodicity of 6.3 nm.[43] This large BCP periodicity was attributed to the strong crystallization of the **4T** molecules, which induced polymer chain stretching in both BCP blocks. All of the NP blends show a reduction in the BCP periodicity at low loading (8/10 wt%) and an even further reduction at high loading (16/20 wt%) compared to the neat supramolecules. This reduction in periodicity suggests that the NPs disrupt the crystallization of **4T** in the comb domains to some extent. All of these blends show peaks at q ~ 0.099 and 0.198 Å^{-1} that correspond to the P4VP(**4T**) comb block with a lamellar periodicity of ~6.3 nm. For PbS-6nm samples, the BCP period is 47 nm for 10 wt% and 44 nm for 20 wt%. The SAXS curve for PbS-6nm10% has a peak at q ~ 0.110 Å^{-1} (5.7 nm), which corresponds to **4T** alone. Interestingly, there is a peak at q ~ 0.140 Å^{-1} (4.5 nm) for PbS-6nm20%, which has not been observed for **4T**-based supramolecules or **4T** alone. However, it is still most likely due to phase-separated **4T** molecules since the peak corresponds to a relatively small periodicity, and some phase-separated **4T** is already present at the lower loading rate. The BCP periodicity is 44 nm for CdSe-3nm8% and 33 nm for CdSe-3nm16%, which are both smaller compared to PbS-6nm samples at similar loading rates. The SAXS profiles also contain a pair of peaks at q ~ 0.113 and 0.226 Å^{-1}, which correspond to a 5.6 nm lamellar periodicity of **4T** alone. While there are scattering peaks present in all of these samples that correspond to phase-separated **4T** molecules, large aggregates were not observed in TEM, so the size of these domains are most likely fairly small and dispersed among the supramolecules.

A single broad diffraction peak at q ~ 1.331 Å^{-1} from the crystallization of **4T** is present in the WAXS profile of both PbS-6nm samples. The peaks corresponding to the (111) and (200) reflections in the PbS lattice are also present. The WAXS profile of the CdSe-3nm samples contain two broadly defined peaks centered at q ~ 1.29 and 1.38 Å^{-1} from **4T** crystallization. The WAXS profiles of both of the CdSe-3nm samples contain broad diffraction peaks between q ~ 1.6–2.0 Å^{-1}, which most likely corresponds to the CdSe lattice reflections. While the scattering results indicate that not all of the **4T** molecules are completely incorporated into the supramolecules upon addition of NPs, they do indicate that a significant fraction of them are incorporated and crystalline.

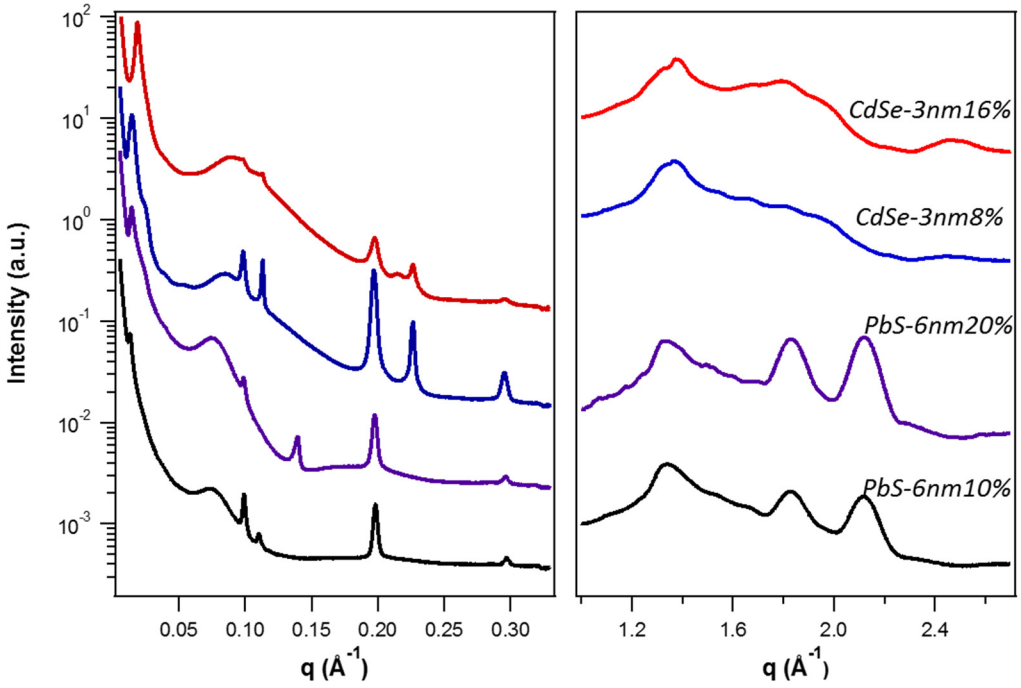

Figure 5.6. (left) SAXS and (right) WAXS profiles of PS-b-P4VP(**4T**)$_{1.5}$ supramolecules blended with (black) PbS-6nm10%, (purple) PbS-6nm20%, (blue) CdSe-3nm8%, or (red) CdSe-3nm16% NPs. The addition of NPs reduces the BCP periodicity at low loading rates (8/10 wt%) and more so at higher loading rates (16/20 wt%). This effect is greater for the smaller NPs (CdSe-3nm). Not all of the SMs incorporate into the supramolecules, however, a significant fraction of **4T** does incorporate and is crystalline.

§ 5.3 Discussion

Our results demonstrate the supramolecular coassembly of SM organic semiconductors and semiconducting NPs using a BCP as a local structure framework and give insights into the thermodynamics and kinetics of this system. In previous studies of directed assemblies of NPs with supramolecules based on less crystalline SMs, well-ordered arrays of NPs can be readily obtained.[24] Well-ordered morphologies of supramolecules based on highly crystalline SMs can also be obtained without the presence of NPs (Figure 5.4a).[42] Kinetically, in **4T**-based supramolecules without NPs, the **4T** molecules have been shown to incorporate into the P4VP microdomains after annealing near or above the T_m of the SM, even when starting from a macrophase separated state.[43] In PS-*b*-P4VP(**4T**)$_{1.5}$/NP blends, the NPs appear to segregate with the **4T** after solvent casting and incorporate into the P4VP(**4T**) microdomains after annealing near or above the T_m of the SM. However, the addition of NPs to organic semiconductor-based supramolecules has a few effects on the overall assembly. 1) The crystallization of **4T** tends to force the NPs to assemble into thinner P4VP(**4T**) domains (type 1), which likely contain fewer **4T** molecules that are less crystalline. This increases the number of defects and reduces the long-range order of the supramolecules. 2) How the NPs assemble within the P4VP(**4T**) domains depends on

the size of the NPs. For example, CdSe-3nm NPs favor assembly in between the comb lamellae into rows perpendicular to the axis of the BCP lamellae, while the PbS-6nm particles tend to assemble into single file sheets parallel to the BCP axis. While our present studies indicate that the assembly of nanocomposites based on highly crystalline SMs is distinct from both nanocomposites based on less crystalline SMs and supramolecules based on highly crystalline SMs without NPs, we have clearly demonstrated nanostructured arrays of organic and inorganic semiconductors. Since the organic semiconductors and NPs are readily interchangeable for other materials, we have developed a modular, supramolecular method for the fabrication of nanocomposites based on highly crystalline, functional SMs and inorganic NPs.

Previous studies of **4T**-based supramolecules showed that only a fraction of the SMs are hydrogen-bonded to the P4VP chains, and a majority of the SMs are macrophase separated from the supramolecules after solvent casting.[43] Based on the scattering profiles and TEM images of the temperature-dependent studies of PS-*b*-P4VP(**4T**)$_{1.5}$ with PbS-6nm11%, the NPs appear to coassemble with the **4T** molecules and separate into small clusters during the solvent drying process. It is likely that **4T** separates due to its high crystallinity and limited solubility in chloroform, and the NPs tend to segregate with the SMs due to the favorable interactions between the alkyl NP ligands and the alkyl moieties in **4T**. As the nanocomposites are annealed below the T_m of **4T** (100–120 °C), the NPs partially incorporate into the supramolecules, along with the **4T** molecules, during annealing. At annealing temperatures where more SMs become incorporated into the supramolecules, more NPs move into the comb domains. When samples are annealed near or above the melting temperature of **4T** (140–160 °C), the NPs form ordered arrays within the supramolecular framework. However, the particles are more evenly dispersed throughout the sample when annealed at 150–160 °C. This is likely due to the fact that the higher temperature affords the particles greater mobility to diffuse through the sample.

From the TEM images of nanocomposites annealed above the T_m of **4T** (150–160 °C) in Figure 5.2d, Figure 5.4b, and Figure 5.5, we can clearly see that the NPs are more abundant in the thinner regions (type 1) of the comb domains and less abundant in the thicker ones (type 2). The thicker domains most likely contain a higher concentration of more crystalline **4T** molecules that can induce stretching of the P4VP(**4T**) block to a greater degree, thus increasing the overall BCP periodicity.[43] Since both BCP blocks were found to stretch due to the crystallization of **4T** in PS-*b*-P4VP(**4T**)$_{1.5}$ supramolecules without NPs, it is somewhat surprising that the PS domains are relatively uniform in thickness for the NP blend samples despite variations in the P4VP(**4T**) domain periodicity. One possible explanation is that the PS chains do in fact stretch in the larger comb (type 2) domains but adopt an interdigitated PS coil structure to maintain a uniform domain size. The use of a more crystalline molecule in BCP-based supramolecules, such as **4T**, most likely increases the entropic penalty for deforming the comb block compared to supramolecules based on less crystalline SMs. Since the incorporation of the NPs deforms the comb block of the supramolecule and hampers the crystallization of **4T** to some degree, it is reasonable that the particles would favor the areas of the P4VP(**4T**) block that are less crystalline or contain less **4T** (Figure 5.5c). Thus, the crystallization of **4T** in SM-rich regions effectively force the NPs to assemble into the less crystalline areas. However, the thinner domains still likely contain a significant amount of the SMs since the favorable enthalpic interaction between **4T** and the NP ligands is the primary driving force for directing their assembly.

Based on the TEM images and scattering profiles from the NP size-dependent studies (Figure 5.5), the larger (PbS-6nm) particles tend to assemble parallel to the BCP lamellae in the

middle of the P4VP(**4T**) domains, and the smaller (CdSe-3nm) particles tend to assemble in rows perpendicular to the BCP lamellae (Figure 5.5). This is likely due to the fact that the entropic penalty for deforming the polymer chain from smaller particles is lower compared to larger ones.[3] This high penalty for larger particles forces them to assemble in the middle of the P4VP(**4T**) domains to minimize the deformation of the supramolecular chain. Our observations here and in previous studies suggest that SMs with a high degree of crystallinity within the comb block can induce a high degree of polymer chain stretching which leads to large supramolecular periodicities.[43] Since the addition of CdSe-3nm decreases this periodicity to a larger extent than PbS-6nm at comparable volume fractions, it is likely that the CdSe-3nm assembly between the comb blocks more greatly disrupts the packing of **4T** within the supramolecules compared to PbS-6nm.

§ 5.4 Conclusion

In summary, we have demonstrated the coassembly of an oligothiophene organic semiconductor-based supramolecule with semiconducting NPs of different sizes and at different loading rates in bulk. The NPs could be incorporated into the supramolecular microdomains during annealing, even when starting from a macrophase-separated state. The crystallinity of the oligothiophene as well as the loading rate and size of the NPs were found to significantly affect the phase behavior of the nanocomposites. The strong crystallization of the SMs tends to force the NPs into less crystalline domains of the comb block, where the oligothiophenes are likely to be less abundant. The introduction of the NPs decreases the BCP periodicity of the supramolecules, and is further reduced at higher loading rates. Larger (6 nm) NPs tend to assemble in rows parallel to the BCP lamellar axis in the center of the comb domains to minimize the entropic penalty of deforming the polymer chain. The smaller (3 nm) particles assemble into rows perpendicular to the axis of the BCP lamellae in between the comb lamellae. While these results indicate that the assembly of supramolecular nanocomposites based on highly crystalline SMs is distinct from both nanocomposites with less crystalline SMs and supramolecules based on highly crystalline SMs without NPs, nanostructured arrays of organic and inorganic semiconductors can be readily obtained. Despite the complexities of this system, these studies present a versatile method for the coassembly of highly crystalline, functional SMs with inorganic NPs for the fabrication of nanocomposite devices.

§ 5.5 Experimental section

5.5.1 Materials

PS(40,000)-*b*-P4VP(5,600) (PDI=1.09), were purchased from Polymer Source, Inc. Chloroform was purchased from Fisher and filtered through basic alumina. Trioctylphosphine oxide (99%), trioctylphosphine (97%), and selenium (99.99%) were purchased from Strem Chemicals. Octadecylphosphonic acid (99%) was purchased from Polycarbon Industries. Cadmium oxide (99.5%), lead chloride, and oleylamine were purchased from Sigma-Aldrich. All other chemicals were purchased from Aldrich and used as received. **4T** was synthesized by Clayton

Mauldin and David Hanifi, and the synthetic procedure to prepare **4T** is described in detail in a previous publication.[42] PbS[44] and CdSe[45] NPs were synthesized by modified versions of previously reported procedures by Peter Bai and Noah Bronstein.

5.5.2 Sample Preparation

4T is light and oxygen sensitive so samples were either prepared in an argon glovebox or cautions were paid to avoid light exposure during the sample preparation process. The PS-*b*-P4VP was first dissolved in chloroform to form 1% (wt/v) stock solutions. The desired amount of **4T** was dissolved in chloroform. The polymer solution was then added to the **4T** solution, followed by stirring overnight. NP solutions were added to the supramolecules and stirred for 20–30 min. Solutions were then transferred into PTFE beakers under a covered dish, and solvent was allowed to slowly evaporate for 24 hours. Samples were then placed in a vacuum oven at RT or 40 °C for 8 h to remove residual solvent. Bulk sample was collected from the beakers, and portions were put into DSC pans, annealed at various temperatures in a vacuum oven overnight, and slowly cooled to room temperature.

5.5.3 Small-Angle and Wide-Angle X-ray Scattering (SAXS/WAXS)

The SAXS and WAXS data were collected on beamline 7.3.3 in the Advanced Light Source (ALS) at the Lawrence Berkeley National Laboratory. X-rays with a wavelength of 1.240 Å (10 KeV) were used, and the scattering spectra were collected on a Pilatus 1M detector. The scattering profiles, after a 60 s collection time, were obtained by integrating the 2-D scattering pattern. Line-averaged intensities are reported as I vs. q, where $q = (4\pi/\lambda)*\sin(\theta/2)$, λ is the wavelength of incident x-rays and θ is the scattering angle. Data was analyzed with Nika 1 (http://usaxs.xray.aps.anl.gov/staff/ilavsky/nika.html),[46] an analysis module designed for Igor Pro (WaveMetrics, Lake Oswego, OR, USA).

5.5.4 Transmission Electron Microscopy (TEM)

The bulk samples were embedded in resin and cured at 60 °C overnight before being microtomed for TEM imaging. The thin sections of PS(40,000)-*b*-P4VP(5,600)(**4T**)$_{1.5}$ supramolecules were exposed to iodine vapor for 10 minutes that selectively stains the P4VP(**4T**)$_r$ block to enhance the contrast. The NP-blended samples were not stained. TEM images were collected on an FEI Tecnai 12 transmission electron microscope at an accelerating voltage of 120 kV. Image analysis was performed using ImageJ (http://rsbweb.nih.gov/ij/).[47]

Afterword

Highly crystalline, functional small molecule(SM)-based supramolecules and their nanocomposites have great potential for the fabrication of low-cost and flexible optical, electronic, and stimuli-responsive devices. Combining functional SMs, polymers, and inorganic nanoparticles (NPs) can potentially take the advantages of all three classes of materials. However, a fundamental understanding and control of the self-assembly and optoelectronic properties of these components is necessary to reach their full potential in optical and electronic devices. For many applications, it is necessary to control the domain size and orientation as well as the molecular and interparticle packing to enhance the performance of the materials. This requires a delicate balance of the assembly of each component as well as the interactions among all of the building blocks. In terms of SMs, this can be tailored by tuning the composition of the crystalline functional core, the location of the alkyl solubilizing groups (side- vs. end-functionalization), and the constitution of the alkyl groups (branched vs. linear).

Since block copolymer-based supramolecules can effectively organize semiconductor NPs into ordered arrays, this may provide a viable and effective means to control their alignment in electronic devices, such as photovoltaics (PVs) and light-emitting diodes (LEDs). Nanocomposites of organic semiconductor-based supramolecules could lead to organic-inorganic hybrid PV and LED devices with well-controlled nanostructures and interparticle ordering. However, in order to effectively interface the organic and inorganic semiconductor materials into well-defined arrays, a greater understanding of the self-assembly of supramolecular nanocomposites based on highly crystalline, functional SMs is required.

One area in need of optimization is improving the electronic coupling between NPs and the interface between the NPs and SMs. One potential strategy is the use of semiconducting ligands, which may simultaneously lower the barrier for charge transport and improve the interface between the organic and inorganic materials. With the optimization of the coupling between NPs and between the NP and SM building blocks, functional SM-based supramolecular nanocomposites that have well-aligned organic/inorganic assemblies with good electronic coupling can potentially be realized.

To summarize, improvements in devices based on these materials will likely come from the optimization of the morphology, packing, interface between the materials, electronic properties, optical properties, and electronic coupling between the SMs and NPs. Significant advances in this field will require collaboration between experts in synthetic chemistry, self-assembly, structural characterization, and device physics. Although there are still many challenges, recent progress paints a bright future for these versatile materials.

References

Chapter 1

(1) Valkama, S.; Kosonen, H.; Ruokolainen, J.; Haatainen, T.; Torkkeli, M.; Serimaa, R.; Ten Brinke, G.; Ikkala, O. *Nat. Mater.* **2004**, *3*, 872.

(2) Valkama, S.; Ruotsalainen, T.; Nykänen, A.; Laiho, A.; Kosonen, H.; ten Brinke, G.; Ikkala, O.; Ruokolainen, J. *Macromolecules* **2006**, *39*, 9327.

(3) Zhao, Y.; Thorkelsson, K.; Mastroianni, A. J.; Schilling, T.; Luther, J. M.; Rancatore, B. J.; Matsunaga, K.; Jinnai, H.; Wu, Y.; Poulsen, D.; Fréchet, J. M. J.; Paul Alivisatos, A.; Xu, T. *Nat. Mater.* **2009**, *8*, 979.

(4) Brabec, C. J.; Cravino, a.; Meissner, D.; Sariciftci, N. S.; Fromherz, T.; Rispens, M. T.; Sanchez, L.; Hummelen, J. C. *Adv. Funct. Mater.* **2001**, *11*, 374.

(5) Li, G.; Shrotriya, V.; Huang, J.; Yao, Y.; Moriarty, T.; Emery, K.; Yang, Y. *Nat. Mater.* **2005**, *4*, 864.

(6) Kim, J. Y.; Lee, K.; Coates, N. E.; Moses, D.; Nguyen, T.-Q.; Dante, M.; Heeger, A. J. *Science* **2007**, *317*, 222.

(7) Sirringhaus, H.; Brown, P. J.; Friend, R. H.; Nielsen, M. M.; Bechgaard, K.; Langeveld-Voss, B. M. W.; Spiering, A. J. H.; Janssen, R. A. J.; Meijer, E. W.; Herwig, P.; de Leeuw, D. M. *Nature* **1999**, *401*, 685.

(8) Kline, R. J.; McGehee, M. D.; Kadnikova, E. N.; Liu, J.; Fréchet, J. M. J. *Adv. Mater.* **2003**, *15*, 1519.

(9) Peumans, P.; Yakimov, A.; Forrest, S. R. *J. Appl. Phys.* **2003**, *93*, 3693.

(10) Katz, H. E.; Bao, Z.; Gilat, S. L. *Acc. Chem. Res.* **2001**, *34*, 359.

(11) Rand, B. P.; Xue, J.; Yang, F.; Forrest, S. R. *Appl. Phys. Lett.* **2005**, *87*, 233508.

(12) Peumans, P.; Uchida, S.; Forrest, S. R. *Nature* **2003**, *425*, 158.

(13) Matsuo, Y.; Sato, Y.; Niinomi, T.; Soga, I.; Tanaka, H.; Nakamura, E. *J. Am. Chem. Soc.* **2009**, *131*, 16048.

(14) Roncali, J. *Acc. Chem. Res.* **2009**, *42*, 1719.

(15) Tamayo, A. B.; Dang, X.-D.; Walker, B.; Seo, J.; Kent, T.; Nguyen, T.-Q. *Appl. Phys. Lett.* **2009**, *94*, 103301.

(16) Riede, M.; Mueller, T.; Tress, W.; Schueppel, R.; Leo, K. *Nanotechnology* **2008**, *19*, 424001.
(17) Ma, B.; Woo, C. H.; Miyamoto, Y.; Fréchet, J. M. J. *Chem. Mater.* **2009**, *21*, 1413.
(18) Nelson, J. *Science* **2001**, *293*, 1059.
(19) Coakley, K. M.; McGehee, M. D. *Chem. Mater.* **2004**, *16*, 4533.
(20) Sun, Y.; Welch, G. C.; Leong, W. L.; Takacs, C. J.; Bazan, G. C.; Heeger, A. J. *Nat. Mater.* **2012**, *11*, 44.
(21) Park, S. H.; Roy, A.; Beaupré, S.; Cho, S.; Coates, N.; Moon, J. S.; Moses, D.; Leclerc, M.; Lee, K.; Heeger, A. J. *Nat. Photonics* **2009**, *3*, 297.
(22) Liang, Y.; Xu, Z.; Xia, J.; Tsai, S.-T.; Wu, Y.; Li, G.; Ray, C.; Yu, L. *Adv. Mater.* **2010**, *22*, E135.
(23) Peet, J.; Heeger, A. J.; Bazan, G. C. *Acc. Chem. Res.* **2009**, *42*, 1700.
(24) Ma, W.; Yang, C.; Gong, X.; Lee, K.; Heeger, a. J. *Adv. Funct. Mater.* **2005**, *15*, 1617.
(25) Reyes-Reyes, M.; Kim, K.; Carroll, D. L. *Appl. Phys. Lett.* **2005**, *87*, 083506.
(26) Peet, J.; Soci, C.; Coffin, R. C.; Nguyen, T. Q.; Mikhailovsky, A.; Moses, D.; Bazan, G. C. *Appl. Phys. Lett.* **2006**, *89*, 252105.
(27) Peet, J.; Kim, J. Y.; Coates, N. E.; Ma, W. L.; Moses, D.; Heeger, A. J.; Bazan, G. C. *Nat. Mater.* **2007**, *6*, 497.
(28) Adams, J.; Gronski, W. *Makromol. Chem., Rapid Commun.* **1989**, *10*, 553.
(29) Gallot, B. *Prog. Polym. Sci.* **1996**, *21*, 1035.
(30) Walther, M.; Finkelmann, H. *Prog. Polym. Sci.* **1996**, *21*, 951.
(31) Mao, G.; Ober, C. K. *Acta Polym.* **1997**, *48*, 405.
(32) Yu, H.; Kobayashi, T.; Yang, H. *Adv. Mater.* **2011**, *23*, 3337.
(33) Yamada, M.; Hirao, A.; Nakahama, S.; Iguchi, T.; Watanabe, J. *Macromolecules* **1995**, *28*, 50.
(34) Mao, G.; Wang, J.; Clingman, S. R.; Ober, C. K.; Chen, J. T.; Thomas, E. L. *Macromolecules* **1997**, *30*, 2556.
(35) Osuji, C.; Ferreira, P. J.; Mao, G.; Ober, C. K.; Vander Sande, J. B.; Thomas, E. L. *Macromolecules* **2004**, *37*, 9903.
(36) Zheng, W. Y.; Hammond, P. T. *Macromolecules* **1998**, *31*, 711.
(37) Anthamatten, M.; Zheng, W. Y.; Hammond, P. T. *Macromolecules* **1999**, *32*, 4838.
(38) Busch, P.; Krishnan, S.; Paik, M.; Toombes, G. E. S.; Smilgies, D.-M.; Gruner, S. M.; Ober, C. K. *Macromolecules* **2007**, *40*, 81.
(39) Morikawa, Y.; Nagano, S.; Watanabe, K.; Kamata, K.; Iyoda, T.; Seki, T. *Adv. Mater.* **2006**, *18*, 883.
(40) Yu, H.; Asaoka, S.; Shishido, A.; Iyoda, T.; Ikeda, T. *Small* **2007**, *3*, 768.
(41) Zhou, Y.; Ahn, S.-K.; Lakhman, R. K.; Gopinadhan, M.; Osuji, C. O.; Kasi, R. M. *Macromolecules* **2011**, *44*, 3924.
(42) Shi, L.-Y.; Zhou, Y.; Fan, X.-H.; Shen, Z. *Macromolecules* **2013**, *46*, 5308.
(43) Stalmach, U.; de Boer, B.; Videlot, C.; van Hutten, P. F.; Hadziioannou, G. *J. Am. Chem. Soc.* **2000**, *122*, 5464.

(44) de Boer, B.; Stalmach, U.; van Hutten, P. F.; Melzer, C.; Krasnikov, V. V.; Hadziioannou, G. *Polymer* **2001**, *42*, 9097.
(45) Schenning, A. P. H. J.; Fransen, M.; van Duren, J. K. J.; van Hal, P. A.; Janssen, R. A. J.; Meijer, E. W. *Macromol. Rapid Commun.* **2002**, *23*, 271.
(46) Lindner, S. M.; Thelakkat, M. *Macromolecules* **2004**, *37*, 8832.
(47) Sommer, M.; Lindner, S. M.; Thelakkat, M. *Adv. Funct. Mater.* **2007**, *17*, 1493.
(48) Sommer, M.; Lang, A. S.; Thelakkat, M. *Angew. Chem., Int. Ed.* **2008**, *47*, 7901.
(49) Sivula, K.; Ball, Z. T.; Watanabe, N.; Fréchet, J. M. J. *Adv. Mater.* **2006**, *18*, 206.
(50) van der Veen, M. H.; de Boer, B.; Stalmach, U.; van de Wetering, K. I.; Hadziioannou, G. *Macromolecules* **2004**, *37*, 3673.
(51) Olsen, B. D.; Segalman, R. A. *Macromolecules* **2005**, *38*, 10127.
(52) Sary, N.; Mezzenga, R.; Brochon, C.; Hadziioannou, G.; Ruokolainen, J. *Macromolecules* **2007**, *40*, 3277.
(53) Sary, N.; Rubatat, L.; Brochon, C.; Hadziioannou, G.; Ruokolainen, J.; Mezzenga, R. *Macromolecules* **2007**, *40*, 6990.
(54) Kato, T.; Fréchet, J. M. J. *Macromolecules* **1989**, *22*, 3818.
(55) Ikkala, O. T.; Laakso, J.; Vakiparta, K.; Virtanen, E.; Ruohonen, H.; Jarvinen, H.; Taka, T.; Passiniemi, P.; Osterholm, J. E.; Cao, Y.; Andreatta, A.; Smith, P.; Heeger, A. J. *Synth. Met.* **1995**, *69*, 97.
(56) Ikkala, O. T.; Pietila, L. O.; Passiniemi, P.; Vikki, T.; Osterholm, H.; Ahjopalo, L.; Osterholm, J. E. *Synth. Met.* **1997**, *84*, 55.
(57) Ruokolainen, J.; Mäkinen, R.; Torkkeli, M.; Mäkelä, T.; Serimaa, R.; ten Brinke, G.; Ikkala, O. *Science* **1998**, *280*, 557.
(58) Ruokolainen, J.; Saariaho, M.; Ikkala, O.; ten Brinke, G.; Thomas, E. L.; Torkkeli, M.; Serimaa, R. *Macromolecules* **1999**, *32*, 1152.
(59) Ikkala, O.; ten Brinke, G. *Chem. Commun.* **2004**, 2131.
(60) Würthner, F.; Chen, Z.; Hoeben, F. J. M.; Osswald, P.; You, C.-C.; Jonkheijm, P.; Herrikhuyzen, J. V.; Schenning, A. P. H. J.; van der Schoot, P. P. A. M.; Meijer, E. W.; Beckers, E. H. A.; Meskers, S. C. J.; Janssen, R. A. J. *J. Am. Chem. Soc.* **2004**, *126*, 10611.
(61) Tang, C.; Lennon, E. M.; Fredrickson, G. H.; Kramer, E. J.; Hawker, C. J. *Science* **2008**, *322*, 429.
(62) Antonietti, M.; Conrad, J. *Angew. Chem., Int. Ed.* **1994**, *33*, 1869.
(63) Fyfe, M. C. T.; Stoddart, J. F. *Acc. Chem. Res.* **1997**, *30*, 393.
(64) Stewart, D.; Imrie, C. T. *Macromolecules* **1997**, *30*, 877.
(65) Mäki-Ontto, R.; de Moel, K.; de Odorico, W.; Ruokolainen, J.; Stamm, M.; ten Brinke, G.; Ikkala, O. *Adv. Mater.* **2001**, *13*, 117.
(66) Sidorenko, A.; Tokarev, I.; Minko, S.; Stamm, M. *J. Am. Chem. Soc.* **2003**, *125*, 12211.
(67) Tung, S.-H.; Xu, T. *Macromolecules* **2009**, *42*, 5761.
(68) Osuji, C.; Chao, C.-Y.; Bita, I.; Ober, C. K.; Thomas, E. L. *Adv. Funct. Mater.* **2002**, *12*, 753.
(69) Chao, C.-Y.; Li, X.; Ober, C. K.; Osuji, C.; Thomas, E. L. *Adv. Funct. Mater.* **2004**, *14*, 364.

(70) Osuji, C. O.; Chao, C.-Y.; Ober, C. K.; Thomas, E. L. *Macromolecules* **2006**, *39*, 3114.
(71) Korhonen, J. T.; Verho, T.; Rannou, P.; Ikkala, O. *Macromolecules* **2010**, *43*, 1507.
(72) Soininen, A. J.; Tanionou, I.; ten Brummelhuis, N.; Schlaad, H.; Hadjichristidis, N.; Ikkala, O.; Raula, J.; Mezzenga, R.; Ruokolainen, J. *Macromolecules* **2012**, *45*, 7091.
(73) Bai, P.; Kim, M. I.; Xu, T. *Macromolecules* **2013**, *46*, 5531.
(74) Gohy, J.-F.; Antoun, S.; Sobry, R.; Van den Bossche, G.; Jérôme, R. *Macromol. Chem. Phys.* **2000**, *201*, 31.
(75) de Wit, J.; van Ekenstein, G. A.; Polushkin, E.; Kvashnina, K.; Bras, W.; Ikkala, O.; ten Brinke, G. *Macromolecules* **2008**, *41*, 4200.
(76) Wu, S.; Bubeck, C. *Macromolecules* **2013**, *46*, 3512.
(77) Gopinadhan, M.; Beach, E. S.; Anastas, P. T.; Osuji, C. O. *Macromolecules* **2010**, *43*, 6646.
(78) Tenneti, K. K.; Chen, X.; Li, C. Y.; Wan, X.; Fan, X.; Zhou, Q.-F.; Rong, L.; Hsiao, B. S. *Macromolecules* **2007**, *40*, 5095.
(79) Albrecht, K.; Mourran, A.; Zhu, X.; Markkula, T.; Groll, J.; Beginn, U.; de Jeu, W. H.; Moeller, M. *Macromolecules* **2008**, *41*, 1728.
(80) Wang, J.; Odarchenko, Y. I.; Defaux, M.; Lejnieks, J.; Ahokhin, D. V.; Keul, H.; Ivanov, D. A.; Möller, M.; Mourran, A. *Macromolecules* **2013**, *46*, 6159.
(81) Babu, S. S.; Möhwald, H.; Nakanishi, T. *Chem. Soc. Rev.* **2010**, *39*, 4021.
(82) Badamshina, E.; Gafurova, M. *J. Mater. Chem.* **2012**, *22*, 9427.
(83) Lu, Z.; Goh, S. H.; Lee, S. Y. *Macromol. Chem. Phys.* **1999**, *200*, 1515.
(84) Huang, X.-D.; Goh, S. H.; Lee, S. Y.; Huan, C. H. A. *Macromol. Chem. Phys.* **2000**, *201*, 281.
(85) Fujita, N.; Yamashita, T.; Asai, M.; Shinkai, S. *Angew. Chem., Int. Ed.* **2005**, *44*, 1257.
(86) Laiho, A.; Ras, R. H. A.; Valkama, S.; Ruokolainen, J.; Österbacka, R.; Ikkala, O. *Macromolecules* **2006**, *39*, 7648.
(87) Sary, N.; Rubatat, L.; Brochon, C.; Hadziioannou, G.; Mezzenga, R. *Macromol. Symp.* **2008**, *268*, 28.
(88) Sary, N.; Richard, F.; Brochon, C.; Leclerc, N.; Lévêque, P.; Audinot, J.-N.; Berson, S.; Heiser, T.; Hadziioannou, G.; Mezzenga, R. *Adv. Mater.* **2010**, *22*, 763.
(89) Gernigon, V.; Lévêque, P.; Richard, F.; Leclerc, N.; Brochon, C.; Braun, C. H.; Ludwigs, S.; Anokhin, D. V.; Ivanov, D. A.; Hadziioannou, G.; Heiser, T. *Macromolecules* **2013**, *46*, 8824.
(90) Lai, Y.-C.; Ohshimizu, K.; Takahashi, A.; Hsu, J.-C.; Higashihara, T.; Ueda, M.; Chen, W.-C. *J. Polym. Sci. Part A: Polym. Chem.* **2011**, *49*, 2577.
(91) Yao, K.; Chen, L.; Li, F.; Wang, P.; Chen, Y. *J. Phys. Chem. C* **2012**, *116*, 714.
(92) Hsu, J.-C.; Liu, C.-L.; Chen, W.-C.; Sugiyama, K.; Hirao, A. *Macromol. Rapid Commun.* **2011**, *32*, 528.
(93) Hsu, J.-C.; Li, C.; Sugiyama, K.; Mezzenga, R.; Hirao, A.; Chen, W.-C. *Soft Matter* **2011**, *7*, 8440.
(94) Lian, S.-L.; Liu, C.-L.; Chen, W.-C. *ACS Appl. Mater. Interfaces* **2011**, *3*, 4504.
(95) Chen, J.-C.; Liu, C.-L.; Sun, Y.-S.; Tung, S.-H.; Chen, W.-C. *Soft Matter* **2012**, *8*, 526.

(96) Li, C.; Hsu, J.-C.; Sugiyama, K.; Hirao, A.; Chen, W.-C.; Mezzenga, R. *Macromolecules* **2009**, *42*, 5793.
(97) Kang, J.; Shin, N.; Jang, D. Y.; Prabhu, V. M.; Yoon, D. Y. *J. Am. Chem. Soc.* **2008**, *130*, 12273.
(98) Rancatore, B. J.; Mauldin, C. E.; Tung, S.-H.; Wang, C.; Hexemer, A.; Strzalka, J.; Fréchet, J. M. J.; Xu, T. *ACS Nano* **2010**, *4*, 2721.
(99) Narayan, R.; Kumar, P.; Narayan, K. S.; Asha, S. K. *Adv. Funct. Mater.* **2013**, *23*, 2033.
(100) Rancatore, B. J.; Mauldin, C. E.; Fréchet, J. M. J.; Xu, T. *Macromolecules* **2012**, *45*, 8292.
(101) Tran, H.; Gopinadhan, M.; Majewski, P. W.; Shade, R.; Steffes, V.; Osuji, C. O.; Campos, L. M. *ACS Nano* **2013**, *7*, 5514.
(102) Kuila, B. K.; Gowd, E. B.; Stamm, M. *Macromolecules* **2010**, *43*, 7713.
(103) Kuila, B. K.; Chakraborty, C.; Malik, S. *Macromolecules* **2013**, *46*, 484.
(104) Balazs, A. C.; Emrick, T.; Russell, T. P. *Science* **2006**, *314*, 1107.
(105) Fogg, D. E.; Radzilowski, L. H.; Blanski, R.; Schrock, R. R.; Thomas, E. L. *Macromolecules* **1997**, *30*, 417.
(106) Shenhar, R.; Norsten, T. B.; Rotello, V. M. *Adv. Mater.* **2005**, *17*, 657.
(107) Bockstaller, M. R.; Mickiewicz, R. A.; Thomas, E. L. *Adv. Mater.* **2005**, *17*, 1331.
(108) Haryono, A.; Binder, W. H. *Small* **2006**, *2*, 600.
(109) Chiu, J. J.; Kim, B. J.; Kramer, E. J.; Pine, D. J. *J. Am. Chem. Soc.* **2005**, *127*, 5036.
(110) Kim, B. J.; Chiu, J. J.; Yi, G.-R.; Pine, D. J.; Kramer, E. J. *Adv. Mater.* **2005**, *17*, 2618.
(111) Kim, B. J.; Bang, J.; Hawker, C. J.; Kramer, E. J. *Macromolecules* **2006**, *39*, 4108.
(112) Kim, B. J.; Bang, J.; Hawker, C. J.; Chiu, J. J.; Pine, D. J.; Jang, S. G.; Yang, S.-M.; Kramer, E. J. *Langmuir* **2007**, *23*, 12693.
(113) Warren, S. C.; Disalvo, F. J.; Wiesner, U. *Nat. Mater.* **2007**, *6*, 156.
(114) Warren, S. C.; Messina, L. C.; Slaughter, L. S.; Kamperman, M.; Zhou, Q.; Gruner, S. M.; DiSalvo, F. J.; Wiesner, U. *Science* **2008**, *320*, 1748.
(115) Lauter-Pasyuk, V.; Lauter, H. J.; Ausserre, D.; Gallot, Y.; Cabuil, V.; Hamdoun, B.; Kornilov, E. I. *Physica B* **1998**, *248*, 243.
(116) Lauter-Pasyuk, V.; Lauter, H. J.; Ausserre, D.; Gallot, Y.; Cabuil, V.; Kornilov, E. I.; Hamdoun, B. *Physica B* **1997**, *241-243*, 1092.
(117) Bockstaller, M. R.; Lapetnikov, Y.; Margel, S.; Thomas, E. L. *J. Am. Chem. Soc.* **2003**, *125*, 5276.
(118) Thompson, R. B.; Ginzburg, V. V.; Matsen, M. W.; Balazs, A. C. *Science* **2001**, *292*, 2469.
(119) Lee, J.; Shou, Z.; Balazs, A. C. *Phys. Rev. Lett.* **2003**, *91*, 136103.
(120) Lee, J. Y.; Shou, Z.; Balazs, A. C. *Macromolecules* **2003**, *36*, 7730.
(121) Kao, J.; Bai, P.; Chuang, V. P.; Jiang, Z.; Ercius, P.; Xu, T. *Nano Lett.* **2012**, *12*, 2610.
(122) Kao, J.; Bai, P.; Lucas, J. M.; Alivisatos, A. P.; Xu, T. *J. Am. Chem. Soc.* **2013**, *135*, 1680.
(123) Kao, J.; Thorkelsson, K.; Bai, P.; Rancatore, B. J.; Xu, T. *Chem. Soc. Rev.* **2013**.
(124) Thorkelsson, K.; Mastroianni, A. J.; Ercius, P.; Xu, T. *Nano Lett.* **2012**, *12*, 498.
(125) Thorkelsson, K.; Nelson, J. H.; Alivisatos, a. P.; Xu, T. *Nano Lett.* **2013**, *13*, 4908.

(126) Thorkelsson, K.; Rancatore, B. J.; Mauldin, C. E.; Luther, J. M.; Poulsen, D.; Fréchet, M. J.; Alivisatos, A. P.; Xu, T. *10th IEEE International Conference on Nanotechnology* **2010**, 51.

(127) Li, W.; Zhang, P.; Dai, M.; He, J.; Babu, T.; Xu, Y.-L.; Deng, R.; Liang, R.; Lu, M.-H.; Nie, Z.; Zhu, J. *Macromolecules* **2013**, *46*, 2241.

(128) Ku, K. H.; Kim, M. P.; Paek, K.; Shin, J. M.; Chung, S.; Jang, S. G.; Chae, W.-S.; Yi, G.-R.; Kim, B. J. *Small* **2013**, *9*, 2667.

(129) Huynh, W. U.; Dittmer, J. J.; Alivisatos, A. P. *Science* **2002**, *295*, 2425.

(130) Fang, C.; Qi, X.-Y.; Fan, Q.-L.; Wang, L.-H.; Huang, W. *Nanotechnology* **2007**, *18*, 035704.

(131) Maria, S.; Susha, A. S.; Sommer, M.; Talapin, D. V.; Rogach, A. L.; Thelakkat, M. *Macromolecules* **2008**, *41*, 6081.

(132) Li, L.; Hollinger, J.; Coombs, N.; Petrov, S.; Seferos, D. S. *Angew. Chem., Int. Ed.* **2011**, *50*, 8148.

(133) Xu, J.; Hu, J.; Liu, X.; Qiu, X.; Wei, Z. *Macromol. Rapid Commun.* **2009**, *30*, 1419.

(134) Ren, S.; Chang, L.-Y.; Lim, S.-K.; Zhao, J.; Smith, M.; Zhao, N.; Bulović, V.; Bawendi, M.; Gradecak, S. *Nano Lett.* **2011**, *11*, 3998.

(135) Liu, Y.; Gibbs, M.; Puthussery, J.; Gaik, S.; Ihly, R.; Hillhouse, H. W.; Law, M. *Nano Lett.* **2010**, *10*, 1960.

(136) Milliron, D. J.; Alivisatos, A. P.; Pitois, C.; Edder, C.; Fréchet, J. M. J. *Adv. Mater.* **2003**, *15*, 58.

(137) Liu, J.; Tanaka, T.; Sivula, K.; Alivisatos, a. P.; Fréchet, J. M. J. *J. Am. Chem. Soc.* **2004**, *126*, 6550.

(138) Skaff, H.; Sill, K.; Emrick, T. *J. Am. Chem. Soc.* **2004**, *126*, 11322.

(139) Bokel, F. A.; Sudeep, P. K.; Pentzer, E.; Emrick, T.; Hayward, R. C. *Macromolecules* **2011**, *44*, 1768.

(140) Pentzer, E. B.; Bokel, F. a.; Hayward, R. C.; Emrick, T. *Adv. Mater.* **2012**, *24*, 2254.

(141) Sun, B.; Marx, E.; Greenham, N. C. *Nano Lett.* **2003**, *3*, 961.

(142) Gur, I.; Fromer, N. A.; Chen, C.-P.; Kanaras, A. G.; Alivisatos, A. P. *Nano Lett.* **2007**, *7*, 409.

Chapter 2

(1) Peumans, P.; Yakimov, A.; Forrest, S. R. *J. Appl. Phys.* **2003**, *93*, 3693.

(2) Katz, H. E.; Bao, Z.; Gilat, S. L. *Acc. Chem. Res.* **2001**, *34*, 359.

(3) Rand, B. P.; Xue, J. G.; Yang, F.; Forrest, S. R. *Appl. Phys. Lett.* **2005**, *87*, 200508.

(4) Peumans, P.; Uchida, S.; Forrest, S. R. *Nature* **2003**, *425*, 158.

(5) Riede, M.; Mueller, T.; Tress, W.; Schueppel, R.; Leo, K. *Nanotechnology* **2008**, *19*.

(6) Matsuo, Y.; Sato, Y.; Niinomi, T.; Soga, I.; Tanaka, H.; Nakamura, E. *J. Am. Chem. Soc.* **2009**, *131*, 16048.

(7) Roncali, J. *Acc. Chem. Res.* **2009**, *42*, 1719.

(8) Tamayo, A. B.; Dang, X.-D.; Walker, B.; Seo, J.; Kent, T.; Nguyen, T.-Q. *Appl. Phys. Lett.* **2009**, *94*, 103301.
(9) Ma, B. W.; Woo, C. H.; Miyamoto, Y.; Frechet, J. M. J. *Chem. Mater.* **2009**, *21*, 1413.
(10) Nelson, J. *Science* **2001**, *293*, 1059.
(11) Coakley, K. M.; McGehee, M. D. *Chem. Mater.* **2004**, *16*, 4533.
(12) Brabec, C. J.; Sariciftci, N. S.; Hummelen, J. C. *Adv. Funct. Mater.* **2001**, *11*, 15.
(13) Li, G.; Shrotriya, V.; Huang, J. S.; Yao, Y.; Moriarty, T.; Emery, K.; Yang, Y. *Nat. Mater.* **2005**, *4*, 864.
(14) Kim, J. Y.; Lee, K.; Coates, N. E.; Moses, D.; Nguyen, T. Q.; Dante, M.; Heeger, A. J. *Science* **2007**, *317*, 222.
(15) Sirringhaus, H.; Brown, P. J.; Friend, R. H.; Nielsen, M. M.; Bechgaard, K.; Langeveld-Voss, B. M. W.; Spiering, A. J. H.; Janssen, R. A. J.; Meijer, E. W.; Herwig, P.; de Leeuw, D. M. *Nature* **1999**, *401*, 685.
(16) Peet, J.; Heeger, A. J.; Bazan, G. C. *Acc. Chem. Res.* **2009**, *42*, 1700.
(17) Ma, W. L.; Yang, C. Y.; Gong, X.; Lee, K.; Heeger, A. J. *Adv. Funct. Mater.* **2005**, *15*, 1617.
(18) Reyes-Reyes, M.; Kim, K.; Carroll, D. L. *Appl. Phys. Lett.* **2005**, *87*.
(19) Huang, E.; Rockford, L.; Russell, T. P.; Hawker, C. J. *Nature* **1998**, *395*, 757.
(20) Kim, S. H.; Misner, M. J.; Xu, T.; Kimura, M.; Russell, T. P. *Adv. Mater.* **2004**, *16*, 226.
(21) Thurn-Albrecht, T.; Schotter, J.; Kastle, C. A.; Emley, N.; Shibauchi, T.; Krusin-Elbaum, L.; Guarini, K.; Black, C. T.; Tuominen, M. T.; Russell, T. P. *Science* **2000**, *290*, 2126.
(22) van der Veen, M. H.; de Boer, B.; Stalmach, U.; van de Wetering, K. I.; Hadziioannou, G. *Macromolecules* **2004**, *37*, 3673.
(23) Olsen, B. D.; Segalman, R. A. *Macromolecules* **2005**, *38*, 10127.
(24) Zhu, Z.; Waller, D.; Gaudiana, R.; Morana, M.; Mühlbacher, D.; Scharber, M.; Brabec, C. *Macromolecules* **2007**, *40*, 1981.
(25) Sommer, M.; Lang, A. S.; Thelakkat, M. *Angew. Chem., Int. Ed.* **2008**, *47*, 7901.
(26) Sary, N.; Mezzenga, R.; Brochon, C.; Hadziioannou, G.; Ruokolainen, J. *Macromolecules* **2007**, *40*, 3277.
(27) Sary, N.; Rubatat, L.; Brochon, C.; Hadziioannou, G.; Ruokolainen, J.; Mezzenga, R. *Macromolecules* **2007**, *40*, 6990.
(28) Sivula, K.; Ball, Z. T.; Watanabe, N.; Fréchet, J. M. J. *Adv. Mater.* **2006**, *18*, 206.
(29) Kato, T.; Fréchet, J. M. J. *Macromolecules* **1989**, *22*, 3818.
(30) Ikkala, O. T.; Laakso, J.; Vakiparta, K.; Virtanen, E.; Ruohonen, H.; Jarvinen, H.; Taka, T.; Passiniemi, P.; Osterholm, J. E.; Cao, Y.; Andreatta, A.; Smith, P.; Heeger, A. J. *Synth. Met.* **1995**, *69*, 97.
(31) Ikkala, O. T.; Pietila, L. O.; Passiniemi, P.; Vikki, T.; Osterholm, H.; Ahjopalo, L.; Osterholm, J. E. *Synth. Met.* **1997**, *84*, 55.
(32) Ikkala, O.; ten Brinke, G. *Chem. Commun.* **2004**, 2131.
(33) Wurthner, F.; Chen, Z. J.; Hoeben, F. J. M.; Osswald, P.; You, C. C.; Jonkheijm, P.; von Herrikhuyzen, J.; Schenning, A. P. H. J.; van der Schoot, P. P. A. M.; Meijer, E. W.; Beckers, E. H. A.; Meskers, S. C. J.; Janssen, R. A. J. *J. Am. Chem. Soc.* **2004**, *126*, 10611.

(34) van Zoelen, W.; Asumaa, T.; Ruokolainen, J.; Ikkala, O.; ten Brinke, G. *Macromolecules* **2008**, *41*, 3199.
(35) van Zoelen, W.; Polushkin, E.; ten Brinke, G. *Macromolecules* **2008**, *41*, 8807.
(36) Tung, S. H.; Kalarickal, N. C.; Mays, J. W.; Xu, T. *Macromolecules* **2008**, *41*, 6453.
(37) Tokarev, I.; Krenek, R.; Burkov, Y.; Schmeisser, D.; Sidorenko, A.; Minko, S.; Stamm, M. *Macromolecules* **2005**, *38*, 507.
(38) Albrecht, K.; Mourran, A.; Zhu, X. M.; Markkula, T.; Groll, J.; Beginn, U.; de Jeu, W. H.; Moeller, M. *Macromolecules* **2008**, *41*, 1728.
(39) Kang, J.; Shin, N.; Jang, D. Y.; Prabhu, V. M.; Yoon, D. Y. *J. Am. Chem. Soc.* **2008**, *130*, 12273.
(40) Sary, N.; Richard, F.; Brochon, C.; Leclerc, N.; Lévêque, P.; Audinot, J.-N.; Berson, S.; Heiser, T.; Hadziioannou, G.; Mezzenga, R. *Adv. Mater.* **2010**, *22*, 763.
(41) Rancatore, B. J.; Mauldin, C. E.; Tung, S.-H.; Wang, C.; Hexemer, A.; Strzalka, J.; Frechet, J. M. J.; Xu, T. *ACS Nano* **2010**, *4*, 2721.
(42) Ruokolainen, J.; Saariaho, M.; Ikkala, O.; ten Brinke, G.; Thomas, E. L.; Torkkeli, M.; Serimaa, R. *Macromolecules* **1999**, *32*, 1152.
(43) Burgaz, E.; Gido, S. P. *Macromolecules* **2000**, *33*, 8739.
(44) Mauldin, C. E.; Puntambekar, K.; Murphy, A. R.; Liao, F.; Subramanian, V.; Frechet, J. M. J.; DeLongchamp, D. M.; Fischer, D. A.; Toney, M. F. *Chem. Mater.* **2009**, *21*, 1927.
(45) Kline, R. J.; McGehee, M. D.; Kadnikova, E. N.; Liu, J.; Fréchet, J. M. J. *Adv. Mater.* **2003**, *15*, 1519.
(46) Yu, G.; Gao, J.; Hummelen, J. C.; Wudl, F.; Heeger, A. J. *Science* **1995**, *270*, 1789.
(47) Blom, P. W. M.; Jong, M. J. M. d.; Vleggaar, J. J. M. *Appl. Phys. Lett.* **1996**, *68*, 3308.
(48) Geens, W.; Shaheen, S. E.; Wessling, B.; Brabec, C. J.; Poortmans, J.; Serdar Sariciftci, N. *Org. Electron.* **2002**, *3*, 105.
(49) Salleo, A.; Street, R. A. *J. Appl. Phys.* **2003**, *94*, 471.
(50) Gomes, H. L.; Stallinga, P.; Dinelli, F.; Murgia, M.; Biscarini, F.; Leeuw, D. M. d.; Muck, T.; Geurts, J.; Molenkamp, L. W.; Wagner, V. *Appl. Phys. Lett.* **2004**, *84*, 3184.
(51) Torres, I.; Taylor, D. M.; Itoh, E. *Appl. Phys. Lett.* **2004**, *85*, 314.
(52) Chang, J. B.; Subramanian, V. *Appl. Phys. Lett.* **2006**, *88*, 233513.
(53) Dodabalapur, A.; Torsi, L.; Katz, H. E. *Science* **1995**, *268*, 270.
(54) Dinelli, F.; Murgia, M.; Levy, P.; Cavallini, M.; Biscarini, F.; de Leeuw, D. M. *Phys. Rev. Lett.* **2004**, *92*, 116802.
(55) Friend, R. H.; Gymer, R. W.; Holmes, A. B.; Burroughes, J. H.; Marks, R. N.; Taliani, C.; Bradley, D. D. C.; Santos, D. A. D.; Bredas, J. L.; Logdlund, M.; Salaneck, W. R. *Nature* **1999**, *397*, 121.
(56) Zhao, Y.; Thorkelsson, K.; Mastroianni, A. J.; Schilling, T.; Luther, J. M.; Rancatore, B. J.; Matsunaga, K.; Jinnai, H.; Wu, Y.; Poulsen, D.; Frechet, J. M. J.; Paul Alivisatos, A.; Xu, T. *Nat. Mater.* **2009**, *8*, 979.

Chapter 3

(1) White, T. J.; Serak, S. V.; Tabiryan, N. V.; Vaia, R. A.; Bunning, T. J. *J. Mater. Chem.* **2009**, *19*, 1080.

(2) Valkama, S.; Ruotsalainen, T.; Nykänen, A.; Laiho, A.; Kosonen, H.; ten Brinke, G.; Ikkala, O.; Ruokolainen, J. *Macromolecules* **2006**, *39*, 9327.
(3) Finkelmann, H.; Nishikawa, E.; Pereira, G.; Warner, M. *Phys. Rev. Lett.* **2001**, *87*, 015501.
(4) Sakurai, S.; Kawada, H.; Hashimoto, T.; Fetters, L. J. *Macromolecules* **1993**, *26*, 5796.
(5) Yu, H.; Kobayashi, T.; Yang, H. *Adv. Mater.* **2011**, *23*, 3337.
(6) Gallot, B. *Prog. Polym. Sci.* **1996**, *21*, 1035.
(7) Walther, M. *Prog. Polym. Sci.* **1996**, *21*, 951.
(8) Adams, J.; Gronski, W. *Makromol. Chem., Rapid Commun.* **1989**, *10*, 553.
(9) Mao, G.; Ober, C. K. *Acta Polym.* **1997**, *48*, 405.
(10) Mao, G.; Wang, J.; Clingman, S. R.; Ober, C. K.; Chen, J. T.; Thomas, E. L. *Macromolecules* **1997**, *30*, 2556.
(11) Osuji, C.; Ferreira, P. J.; Mao, G.; Ober, C. K.; Vander Sande, J. B.; Thomas, E. L. *Macromolecules* **2004**, *37*, 9903.
(12) Yamada, M.; Hirao, A.; Nakahama, S.; Iguchi, T.; Watanabe, J. *Macromolecules* **1995**, *28*, 50.
(13) Anthamatten, M.; Hammond, P. T. *Macromolecules* **1999**, *32*, 8066.
(14) Kato, T.; Fréchet, J. M. J. *Macromolecules* **1989**, *22*, 3818.
(15) Ikkala, O. T.; Laakso, J.; Vakiparta, K.; Virtanen, E.; Ruohonen, H.; Jarvinen, H.; Taka, T.; Passiniemi, P.; Osterholm, J. E.; Cao, Y.; Andreatta, A.; Smith, P.; Heeger, A. J. *Synth. Met.* **1995**, *69*, 97.
(16) Ikkala, O. T.; Pietila, L. O.; Passiniemi, P.; Vikki, T.; Osterholm, H.; Ahjopalo, L.; Osterholm, J. E. *Synth. Met.* **1997**, *84*, 55.
(17) Ikkala, O.; ten Brinke, G. *Chem. Commun.* **2004**, 2131.
(18) Würthner, F.; Chen, Z.; Hoeben, F. J. M.; Osswald, P.; You, C.-C.; Jonkheijm, P.; Herrikhuyzen, J. V.; Schenning, A. P. H. J.; van der Schoot, P. P. A. M.; Meijer, E. W.; Beckers, E. H. A.; Meskers, S. C. J.; Janssen, R. A. J. *J. Am. Chem. Soc.* **2004**, *126*, 10611.
(19) Tang, C.; Lennon, E. M.; Fredrickson, G. H.; Kramer, E. J.; Hawker, C. J. *Science* **2008**, *322*, 429.
(20) Antonietti, M.; Conrad, J. *Angew. Chem., Int. Ed.* **1994**, *33*, 1869.
(21) Fyfe, M. C. T.; Stoddart, J. F. *Acc. Chem. Res.* **1997**, *30*, 393.
(22) Sary, N.; Richard, F.; Brochon, C.; Leclerc, N.; Lévêque, P.; Audinot, J.-N.; Berson, S.; Heiser, T.; Hadziioannou, G.; Mezzenga, R. *Adv. Mater.* **2010**, *22*, 763.
(23) Yao, K.; Chen, L.; Li, F.; Wang, P.; Chen, Y. *J. Phys. Chem. C* **2012**, *116*, 714.
(24) Chao, C.-Y.; Li, X.; Ober, C. K.; Osuji, C.; Thomas, E. L. *Adv. Funct. Mater.* **2004**, *14*, 364.
(25) Stewart, D.; Imrie, C. T. *Macromolecules* **1997**, *30*, 877.
(26) Ruokolainen, J.; Mäkinen, R.; Torkkeli, M.; Mäkelä, T.; Serimaa, R.; ten Brinke, G.; Ikkala, O. *Science* **1998**, *280*, 557.
(27) Tung, S.-H.; Kalarickal, N. C.; Mays, J. W.; Xu, T. *Macromolecules* **2008**, *41*, 6453.
(28) Tung, S.-H.; Xu, T. *Macromolecules* **2009**, *42*, 5761.
(29) Kao, J.; Tingsanchali, J.; Xu, T. *Macromolecules* **2011**, *44*, 4392.

(30) van Zoelen, W.; Asumaa, T.; Ruokolainen, J.; Ikkala, O.; ten Brinke, G. *Macromolecules* **2008**, *41*, 3199.
(31) van Zoelen, W.; Polushkin, E.; ten Brinke, G. *Macromolecules* **2008**, *41*, 8807.
(32) Zhao, Y.; Thorkelsson, K.; Mastroianni, A. J.; Schilling, T.; Luther, J. M.; Rancatore, B. J.; Matsunaga, K.; Jinnai, H.; Wu, Y.; Poulsen, D.; Fréchet, J. M. J.; Paul Alivisatos, A.; Xu, T. *Nat. Mater.* **2009**, *8*, 979.
(33) Kumar, U.; Kato, T.; Fréchet, J. M. J. *J. Am. Chem. Soc.* **1992**, *114*, 6630.
(34) Katz, H. E.; Bao, Z.; Gilat, S. L. *Acc. Chem. Res.* **2001**, *34*, 359.
(35) Ma, B.; Woo, C. H.; Miyamoto, Y.; Fréchet, J. M. J. *Chem. Mater.* **2009**, *21*, 1413.
(36) Rancatore, B. J.; Mauldin, C. E.; Tung, S.-H.; Wang, C.; Hexemer, A.; Strzalka, J.; Fréchet, J. M. J.; Xu, T. *ACS Nano* **2010**, *4*, 2721.
(37) Gohy, J.-F.; Antoun, S.; Sobry, R.; Van den Bossche, G.; Jérôme, R. *Macromol. Chem. Phys.* **2000**, *201*, 31.
(38) Korhonen, J. T.; Verho, T.; Rannou, P.; Ikkala, O. *Macromolecules* **2010**, *43*, 1507.
(39) ten Brinke, G.; Ruokolainen, J.; Ikkala, O. *Adv. Polym. Sci.* **2007**, *207*, 113.
(40) Fichou, D. *Handbook of Oligo- and Polythiophenes*; Wiley-VCH, 1999.
(41) Smits, E. C. P.; Mathijssen, S. G. J.; van Hal, P. A.; Setayesh, S.; Geuns, T. C. T.; Mutsaers, K. A. H. A.; Cantatore, E.; Wondergem, H. J.; Werzer, O.; Resel, R.; Kemerink, M.; Kirchmeyer, S.; Muzafarov, A. M.; Ponomarenko, S. A.; de Boer, B.; Blom, P. W. M.; de Leeuw, D. M. *Nature* **2008**, *455*, 956.
(42) Hendriksen, B. L. M.; Martin, F.; Qi, Y.; Mauldin, C.; Vukmirovic, N.; Ren, J.; Wormeester, H.; Katan, A. J.; Altoe, V.; Aloni, S.; Fréchet, J. M. J.; Wang, L.-W.; Salmeron, M. *Nano Lett.* **2011**, *11*, 4107.
(43) Ruokolainen, J.; Saariaho, M.; Ikkala, O.; ten Brinke, G.; Thomas, E. L.; Torkkeli, M.; Serimaa, R. *Macromolecules* **1999**, *32*, 1152.
(44) Edrington, a. C.; Urbas, a. M.; DeRege, P.; Chen, C. X.; Swager, T. M.; Hadjichristidis, N.; Xenidou, M.; Fetters, L. J.; Joannopoulos, J. D.; Fink, Y.; Thomas, E. L. *Adv. Mater.* **2001**, *13*, 421.
(45) Runge, M. B.; Bowden, N. B. *J. Am. Chem. Soc.* **2007**, *129*, 10551.

Chapter 4

(1) Kato, T.; Fréchet, J. M. J. *Macromolecules* **1989**, *22*, 3818.
(2) Ikkala, O. T.; Laakso, J.; Vakiparta, K.; Virtanen, E.; Ruohonen, H.; Jarvinen, H.; Taka, T.; Passiniemi, P.; Osterholm, J. E.; Cao, Y.; Andreatta, A.; Smith, P.; Heeger, A. J. *Synth. Met.* **1995**, *69*, 97.
(3) Ikkala, O. T.; Pietila, L. O.; Passiniemi, P.; Vikki, T.; Osterholm, H.; Ahjopalo, L.; Osterholm, J. E. *Synth. Met.* **1997**, *84*, 55.
(4) Ruokolainen, J.; Mäkinen, R.; Torkkeli, M.; Mäkelä, T.; Serimaa, R.; ten Brinke, G.; Ikkala, O. *Science* **1998**, *280*, 557.
(5) Ruokolainen, J.; Saariaho, M.; Ikkala, O.; ten Brinke, G.; Thomas, E. L.; Torkkeli, M.; Serimaa, R. *Macromolecules* **1999**, *32*, 1152.
(6) Ikkala, O.; ten Brinke, G. *Chem. Commun.* **2004**, 2131.

(7) Würthner, F.; Chen, Z.; Hoeben, F. J. M.; Osswald, P.; You, C.-C.; Jonkheijm, P.; Herrikhuyzen, J. V.; Schenning, A. P. H. J.; van der Schoot, P. P. a. M.; Meijer, E. W.; Beckers, E. H. a.; Meskers, S. C. J.; Janssen, R. A. J. *J. Am. Chem. Soc.* **2004**, *126*, 10611.

(8) Tang, C.; Lennon, E. M.; Fredrickson, G. H.; Kramer, E. J.; Hawker, C. J. *Science* **2008**, *322*, 429.

(9) Antonietti, M.; Conrad, J. *Angew. Chem., Int. Ed.* **1994**, *33*, 1869.

(10) Fyfe, M. C. T.; Stoddart, J. F. *Acc. Chem. Res.* **1997**, *30*, 393.

(11) Stewart, D.; Imrie, C. T. *Macromolecules* **1997**, *30*, 877.

(12) Valkama, S.; Kosonen, H.; Ruokolainen, J.; Haatainen, T.; Torkkeli, M.; Serimaa, R.; ten Brinke, G.; Ikkala, O. *Nat. Mater.* **2004**, *3*, 872.

(13) Valkama, S.; Ruotsalainen, T.; Nykänen, A.; Laiho, A.; Kosonen, H.; ten Brinke, G.; Ikkala, O.; Ruokolainen, J. *Macromolecules* **2006**, *39*, 9327.

(14) Mäki-Ontto, R.; de Moel, K.; de Odorico, W.; Ruokolainen, J.; Stamm, M.; ten Brinke, G.; Ikkala, O. *Adv. Mater.* **2001**, *13*, 117.

(15) Sidorenko, A.; Tokarev, I.; Minko, S.; Stamm, M. *J. Am. Chem. Soc.* **2003**, *125*, 12211.

(16) Tung, S.-H.; Xu, T. *Macromolecules* **2009**, *42*, 5761.

(17) Osuji, C.; Chao, C.-Y.; Bita, I.; Ober, C. K.; Thomas, E. L. *Adv. Funct. Mater.* **2002**, *12*, 753.

(18) Chao, C.-Y.; Li, X.; Ober, C. K.; Osuji, C.; Thomas, E. L. *Adv. Funct. Mater.* **2004**, *14*, 364.

(19) Osuji, C. O.; Chao, C.-Y.; Ober, C. K.; Thomas, E. L. *Macromolecules* **2006**, *39*, 3114.

(20) Korhonen, J. T.; Verho, T.; Rannou, P.; Ikkala, O. *Macromolecules* **2010**, *43*, 1507.

(21) Soininen, A. J.; Tanionou, I.; ten Brummelhuis, N.; Schlaad, H.; Hadjichristidis, N.; Ikkala, O.; Raula, J.; Mezzenga, R.; Ruokolainen, J. *Macromolecules* **2012**, *45*, 7091.

(22) Bai, P.; Kim, M. I.; Xu, T. *Macromolecules* **2013**, *46*, 5531.

(23) Gohy, J.-F.; Antoun, S.; Sobry, R.; Van den Bossche, G.; Jérôme, R. *Macromol. Chem. Phys.* **2000**, *201*, 31.

(24) de Wit, J.; van Ekenstein, G. A.; Polushkin, E.; Kvashnina, K.; Bras, W.; Ikkala, O.; ten Brinke, G. *Macromolecules* **2008**, *41*, 4200.

(25) Wu, S.; Bubeck, C. *Macromolecules* **2013**, *46*, 3512.

(26) Tenneti, K. K.; Chen, X.; Li, C. Y.; Wan, X.; Fan, X.; Zhou, Q.-F.; Rong, L.; Hsiao, B. S. *Macromolecules* **2007**, *40*, 5095.

(27) Albrecht, K.; Mourran, A.; Zhu, X.; Markkula, T.; Groll, J.; Beginn, U.; de Jeu, W. H.; Moeller, M. *Macromolecules* **2008**, *41*, 1728.

(28) Wang, J.; Odarchenko, Y. I.; Defaux, M.; Lejnieks, J.; Ahokhin, D. V.; Keul, H.; Ivanov, D. A.; Möller, M.; Mourran, A. *Macromolecules* **2013**, *46*, 6159.

(29) Gopinadhan, M.; Beach, E. S.; Anastas, P. T.; Osuji, C. O. *Macromolecules* **2010**, *43*, 6646.

(30) Rancatore, B. J.; Mauldin, C. E.; Tung, S.-H.; Wang, C.; Hexemer, A.; Strzalka, J.; Fréchet, J. M. J.; Xu, T. *ACS Nano* **2010**, *4*, 2721.

(31) Narayan, R.; Kumar, P.; Narayan, K. S.; Asha, S. K. *Adv. Funct. Mater.* **2013**, *23*, 2033.

(32) Rancatore, B. J.; Mauldin, C. E.; Fréchet, J. M. J.; Xu, T. *Macromolecules* **2012**, *45*, 8292.

(33) Sary, N.; Richard, F.; Brochon, C.; Leclerc, N.; Lévêque, P.; Audinot, J.-N.; Berson, S.; Heiser, T.; Hadziioannou, G.; Mezzenga, R. *Adv. Mater.* **2010**, *22*, 763.
(34) Yao, K.; Chen, L.; Li, F.; Wang, P.; Chen, Y. *J. Phys. Chem. C* **2012**, *116*, 714.
(35) Huang, X.-D.; Goh, S. H.; Lee, S. Y.; Huan, C. H. A. *Macromol. Chem. Phys.* **2000**, *201*, 281.
(36) Fujita, N.; Yamashita, T.; Asai, M.; Shinkai, S. *Angew. Chem., Int. Ed.* **2005**, *44*, 1257.
(37) Laiho, A.; Ras, R. H. A.; Valkama, S.; Ruokolainen, J.; Österbacka, R.; Ikkala, O. *Macromolecules* **2006**, *39*, 7648.
(38) Kuila, B. K.; Gowd, E. B.; Stamm, M. *Macromolecules* **2010**, *43*, 7713.
(39) Kuila, B. K.; Chakraborty, C.; Malik, S. *Macromolecules* **2013**, *46*, 484.
(40) Tran, H.; Gopinadhan, M.; Majewski, P. W.; Shade, R.; Steffes, V.; Osuji, C. O.; Campos, L. M. *ACS Nano* **2013**, *7*, 5514.
(41) Adams, J.; Gronski, W. *Makromol. Chem., Rapid Commun.* **1989**, *10*, 553.
(42) Gallot, B. *Prog. Polym. Sci.* **1996**, *21*, 1035.
(43) Walther, M.; Finkelmann, H. *Prog. Polym. Sci.* **1996**, *21*, 951.
(44) Mao, G.; Ober, C. K. *Acta Polym.* **1997**, *48*, 405.
(45) Yu, H.; Kobayashi, T.; Yang, H. *Adv. Mater.* **2011**, *23*, 3337.
(46) Yamada, M.; Hirao, A.; Nakahama, S.; Iguchi, T.; Watanabe, J. *Macromolecules* **1995**, *28*, 50.
(47) Mao, G.; Wang, J.; Clingman, S. R.; Ober, C. K.; Chen, J. T.; Thomas, E. L. *Macromolecules* **1997**, *30*, 2556.
(48) Osuji, C.; Ferreira, P. J.; Mao, G.; Ober, C. K.; Vander Sande, J. B.; Thomas, E. L. *Macromolecules* **2004**, *37*, 9903.
(49) Zheng, W. Y.; Hammond, P. T. *Macromolecules* **1998**, *31*, 711.
(50) Anthamatten, M.; Zheng, W. Y.; Hammond, P. T. *Macromolecules* **1999**, *32*, 4838.
(51) Busch, P.; Krishnan, S.; Paik, M.; Toombes, G. E. S.; Smilgies, D.-M.; Gruner, S. M.; Ober, C. K. *Macromolecules* **2007**, *40*, 81.
(52) Morikawa, Y.; Nagano, S.; Watanabe, K.; Kamata, K.; Iyoda, T.; Seki, T. *Adv. Mater.* **2006**, *18*, 883.
(53) Yu, H.; Asaoka, S.; Shishido, A.; Iyoda, T.; Ikeda, T. *Small* **2007**, *3*, 768.
(54) Zhou, Y.; Ahn, S.-k.; Lakhman, R. K.; Gopinadhan, M.; Osuji, C. O.; Kasi, R. M. *Macromolecules* **2011**, *44*, 3924.
(55) Shi, L.-Y.; Zhou, Y.; Fan, X.-H.; Shen, Z. *Macromolecules* **2013**, *46*, 5308.
(56) Finkelmann, H.; Nishikawa, E.; Pereira, G.; Warner, M. *Phys. Rev. Lett.* **2001**, *87*, 015501.
(57) White, T. J.; Serak, S. V.; Tabiryan, N. V.; Vaia, R. A.; Bunning, T. J. *J. Mater. Chem.* **2009**, *19*, 1080.
(58) Li, C. Y.; Tenneti, K. K.; Zhang, D.; Zhang, H.; Wan, X.; Chen, E.-Q.; Zhou, Q.-F.; Carlos, A.-O.; Igos, S.; Hsiao, B. S. *Macromolecules* **2004**, *37*, 2854.
(59) Tenneti, K. K.; Chen, X.; Li, C. Y.; Shen, Z.; Wan, X.; Fan, X.; Zhou, Q.-F.; Rong, L.; Hsiao, B. S. *Macromolecules* **2009**, *42*, 3510.

(60) Wen, G.-H.; Zhang, B.; Xie, H.-L.; Liu, X.; Zhong, G.-Q.; Zhang, H.-L.; Chen, E.-Q. *Macromolecules* **2013**, *46*, 5249.
(61) Bae, J.; Kim, J.-K.; Oh, N.-k.; Lee, M. *Macromolecules* **2005**, *38*, 4226.
(62) Stalmach, U.; de Boer, B.; Videlot, C.; van Hutten, P. F.; Hadziioannou, G. *J. Am. Chem. Soc.* **2000**, *122*, 5464.
(63) de Boer, B.; Stalmach, U.; van Hutten, P. F.; Melzer, C.; Krasnikov, V. V.; Hadziioannou, G. *Polymer* **2001**, *42*, 9097.
(64) Schenning, A. P. H. J.; Fransen, M.; van Duren, J. K. J.; van Hal, P. A.; Janssen, R. A. J.; Meijer, E. W. *Macromol. Rapid Commun.* **2002**, *23*, 271.
(65) Lindner, S. M.; Thelakkat, M. *Macromolecules* **2004**, *37*, 8832.
(66) Sommer, M.; Lindner, S. M.; Thelakkat, M. *Adv. Funct. Mater.* **2007**, *17*, 1493.
(67) Sommer, M.; Lang, A. S.; Thelakkat, M. *Angew. Chem., Int. Ed.* **2008**, *47*, 7901.
(68) Sivula, K.; Ball, Z. T.; Watanabe, N.; Fréchet, J. M. J. *Adv. Mater.* **2006**, *18*, 206.
(69) Zhao, Y.; Thorkelsson, K.; Mastroianni, A. J.; Schilling, T.; Luther, J. M.; Rancatore, B. J.; Matsunaga, K.; Jinnai, H.; Wu, Y.; Poulsen, D.; Fréchet, J. M. J.; Paul Alivisatos, A.; Xu, T. *Nat. Mater.* **2009**, *8*, 979.
(70) Sary, N.; Rubatat, L.; Brochon, C.; Hadziioannou, G.; Mezzenga, R. *Macromol. Symp.* **2008**, *268*, 28.
(71) Tamayo, A. B.; Walker, B.; Nguyen, T.-Q. *J. Phys. Chem. C* **2008**, *112*, 11545.
(72) Wienk, M. M.; Turbiez, M.; Gilot, J.; Janssen, R. A. J. *Adv. Mater.* **2008**, *20*, 2556.
(73) Kim, C.; Liu, J.; Lin, J.; Tamayo, A. B.; Walker, B.; Wu, G.; Nguyen, T.-Q. *Chem. Mater.* **2012**, *24*, 1699.
(74) Liu, J.; Walker, B.; Tamayo, A.; Zhang, Y.; Nguyen, T.-Q. *Adv. Funct. Mater.* **2013**, *23*, 47.
(75) Ilavsky, J. *J. Appl. Crystallogr.* **2012**, *45*, 324.
(76) Schneider, C. A.; Rasband, W. S.; Eliceiri, K. W. *Nat. Methods* **2012**, *9*, 671.

Chapter 5

(1) Choi, C. L.; Alivisatos, A. P. *Annu. Rev. Phys. Chem.* **2010**, *61*, 369.
(2) Talapin, D. V.; Lee, J.-S.; Kovalenko, M. V.; Shevchenko, E. V. *Chem. Rev.* **2010**, *110*, 389.
(3) Bockstaller, M. R.; Mickiewicz, R. A.; Thomas, E. L. *Adv. Mater.* **2005**, *17*, 1331.
(4) Balazs, A. C.; Emrick, T.; Russell, T. P. *Science* **2006**, *314*, 1107.
(5) Fogg, D. E.; Radzilowski, L. H.; Blanski, R.; Schrock, R. R.; Thomas, E. L. *Macromolecules* **1997**, *30*, 417.
(6) Shenhar, R.; Norsten, T. B.; Rotello, V. M. *Adv. Mater.* **2005**, *17*, 657.
(7) Haryono, A.; Binder, W. H. *Small* **2006**, *2*, 600.
(8) Chiu, J. J.; Kim, B. J.; Kramer, E. J.; Pine, D. J. *J. Am. Chem. Soc.* **2005**, *127*, 5036.
(9) Kim, B. J.; Chiu, J. J.; Yi, G.-R.; Pine, D. J.; Kramer, E. J. *Adv. Mater.* **2005**, *17*, 2618.
(10) Kim, B. J.; Bang, J.; Hawker, C. J.; Kramer, E. J. *Macromolecules* **2006**, *39*, 4108.

(11) Kim, B. J.; Bang, J.; Hawker, C. J.; Chiu, J. J.; Pine, D. J.; Jang, S. G.; Yang, S.-M.; Kramer, E. J. *Langmuir* **2007**, *23*, 12693.

(12) Warren, S. C.; Disalvo, F. J.; Wiesner, U. *Nat. Mater.* **2007**, *6*, 156.

(13) Warren, S. C.; Messina, L. C.; Slaughter, L. S.; Kamperman, M.; Zhou, Q.; Gruner, S. M.; DiSalvo, F. J.; Wiesner, U. *Science* **2008**, *320*, 1748.

(14) Lauter-Pasyuk, V.; Lauter, H. J.; Ausserre, D.; Gallot, Y.; Cabuil, V.; Kornilov, E. I.; Hamdoun, B. *Physica B* **1997**, *241-243*, 1092.

(15) Lauter-Pasyuk, V.; Lauter, H. J.; Ausserre, D.; Gallot, Y.; Cabuil, V.; Hamdoun, B.; Kornilov, E. I. *Physica B* **1998**, *248*, 243.

(16) Bockstaller, M. R.; Lapetnikov, Y.; Margel, S.; Thomas, E. L. *J. Am. Chem. Soc.* **2003**, *125*, 5276.

(17) Thompson, R. B.; Ginzburg, V. V.; Matsen, M. W.; Balazs, A. C. *Science* **2001**, *292*, 2469.

(18) Lee, J. Y.; Shou, Z.; Balazs, A. C. *Macromolecules* **2003**, *36*, 7730.

(19) Lee, J. Y.; Shou, Z.; Balazs, A. C. *Phys. Rev. Lett.* **2003**, *91*, 136103.

(20) Kato, T.; Fréchet, J. M. J. *Macromolecules* **1989**, *22*, 3818.

(21) Ruokolainen, J.; Saariaho, M.; Ikkala, O.; ten Brinke, G.; Thomas, E. L.; Torkkeli, M.; Serimaa, R. *Macromolecules* **1999**, *32*, 1152.

(22) Ikkala, O.; ten Brinke, G. *Chem. Commun.* **2004**, 2131.

(23) Valkama, S.; Ruotsalainen, T.; Nykänen, A.; Laiho, A.; Kosonen, H.; ten Brinke, G.; Ikkala, O.; Ruokolainen, J. *Macromolecules* **2006**, *39*, 9327.

(24) Zhao, Y.; Thorkelsson, K.; Mastroianni, A. J.; Schilling, T.; Luther, J. M.; Rancatore, B. J.; Matsunaga, K.; Jinnai, H.; Wu, Y.; Poulsen, D.; Fréchet, J. M. J.; Paul Alivisatos, A.; Xu, T. *Nat. Mater.* **2009**, *8*, 979.

(25) Thorkelsson, K.; Mastroianni, A. J.; Ercius, P.; Xu, T. *Nano Lett.* **2012**, *12*, 498.

(26) Thorkelsson, K.; Nelson, J. H.; Alivisatos, a. P.; Xu, T. *Nano Lett.* **2013**, *13*, 4908.

(27) Kao, J.; Bai, P.; Chuang, V. P.; Jiang, Z.; Ercius, P.; Xu, T. *Nano Lett.* **2012**, *12*, 2610.

(28) Kao, J.; Bai, P.; Lucas, J. M.; Alivisatos, A. P.; Xu, T. *J. Am. Chem. Soc.* **2013**, *135*, 1680.

(29) Ku, K. H.; Kim, M. P.; Paek, K.; Shin, J. M.; Chung, S.; Jang, S. G.; Chae, W.-S.; Yi, G.-R.; Kim, B. J. *Small* **2013**, *9*, 2667.

(30) Thorkelsson, K.; Rancatore, B. J.; Mauldin, C. E.; Luther, J. M.; Poulsen, D.; Fréchet, J. M. J.; Alivisatos, A. P.; Xu, T. *10th IEEE International Conference on Nanotechnology* **2010**, 51.

(31) Huynh, W. U.; Dittmer, J. J.; Alivisatos, A. P. *Science* **2002**, *295*, 2425.

(32) Fang, C.; Qi, X.-Y.; Fan, Q.-L.; Wang, L.-H.; Huang, W. *Nanotechnology* **2007**, *18*, 035704.

(33) Maria, S.; Susha, A. S.; Sommer, M.; Talapin, D. V.; Rogach, A. L.; Thelakkat, M. *Macromolecules* **2008**, *41*, 6081.

(34) Li, L.; Hollinger, J.; Coombs, N.; Petrov, S.; Seferos, D. S. *Angew. Chem., Int. Ed.* **2011**, *50*, 8148.

(35) Xu, J.; Hu, J.; Liu, X.; Qiu, X.; Wei, Z. *Macromol. Rapid Commun.* **2009**, *30*, 1419.

(36) Ren, S.; Chang, L.-Y.; Lim, S.-K.; Zhao, J.; Smith, M.; Zhao, N.; Bulović, V.; Bawendi, M.; Gradecak, S. *Nano Lett.* **2011**, *11*, 3998.

(37) Milliron, D. J.; Alivisatos, A. P.; Pitois, C.; Edder, C.; Fréchet, J. M. J. *Adv. Mater.* **2003**, *15*, 58.

(38) Liu, J.; Tanaka, T.; Sivula, K.; Alivisatos, A. P.; Fréchet, J. M. J. *J. Am. Chem. Soc.* **2004**, *126*, 6550.

(39) Skaff, H.; Sill, K.; Emrick, T. *J. Am. Chem. Soc.* **2004**, *126*, 11322.

(40) Bokel, F. A.; Sudeep, P. K.; Pentzer, E.; Emrick, T.; Hayward, R. C. *Macromolecules* **2011**, *44*, 1768.

(41) Pentzer, E. B.; Bokel, F. a.; Hayward, R. C.; Emrick, T. *Adv. Mater.* **2012**, *24*, 2254.

(42) Rancatore, B. J.; Mauldin, C. E.; Tung, S.-H.; Wang, C.; Hexemer, A.; Strzalka, J.; Fréchet, J. M. J.; Xu, T. *ACS Nano* **2010**, *4*, 2721.

(43) Rancatore, B. J.; Mauldin, C. E.; Fréchet, J. M. J.; Xu, T. *Macromolecules* **2012**, *45*, 8292.

(44) Cademartiri, L.; Bertolotti, J.; Sapienza, R.; Wiersma, D. S.; von Freymann, G.; Ozin, G. A. *J. Phys. Chem. B* **2006**, *110*, 671.

(45) Carbone, L.; Nobile, C.; De Giorgi, M.; Sala, F. D.; Morello, G.; Pompa, P.; Hytch, M.; Snoeck, E.; Fiore, A.; Franchini, I. R.; Nadasan, M.; Silvestre, A. F.; Chiodo, L.; Kudera, S.; Cingolani, R.; Krahne, R.; Manna, L. *Nano Lett.* **2007**, *7*, 2942.

(46) Ilavsky, J. *J. Appl. Crystallogr.* **2012**, *45*, 324.

(47) Schneider, C. A.; Rasband, W. S.; Eliceiri, K. W. *Nat. Methods* **2012**, *9*, 671.

Appendix

A.1 Supporting Information for Chapter 3

A.1.1

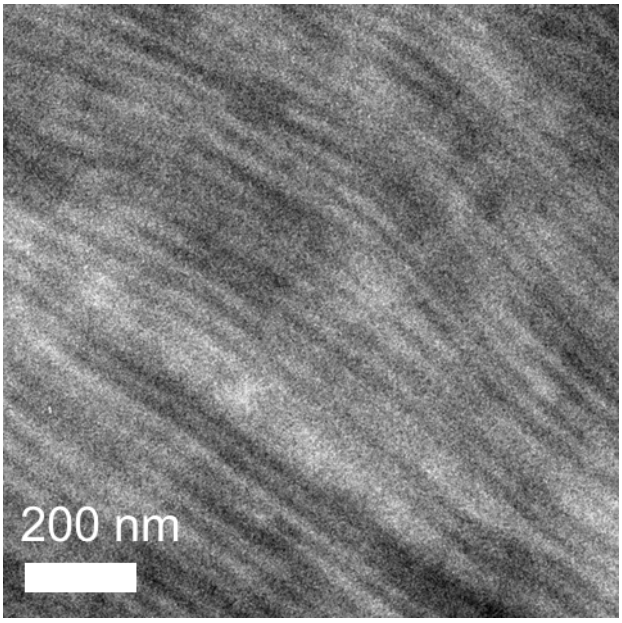

A.1.1. TEM image of an unstained PS-*b*-P4VP**(4T)**$_{1.5}$ supramolecule.

A.1.2

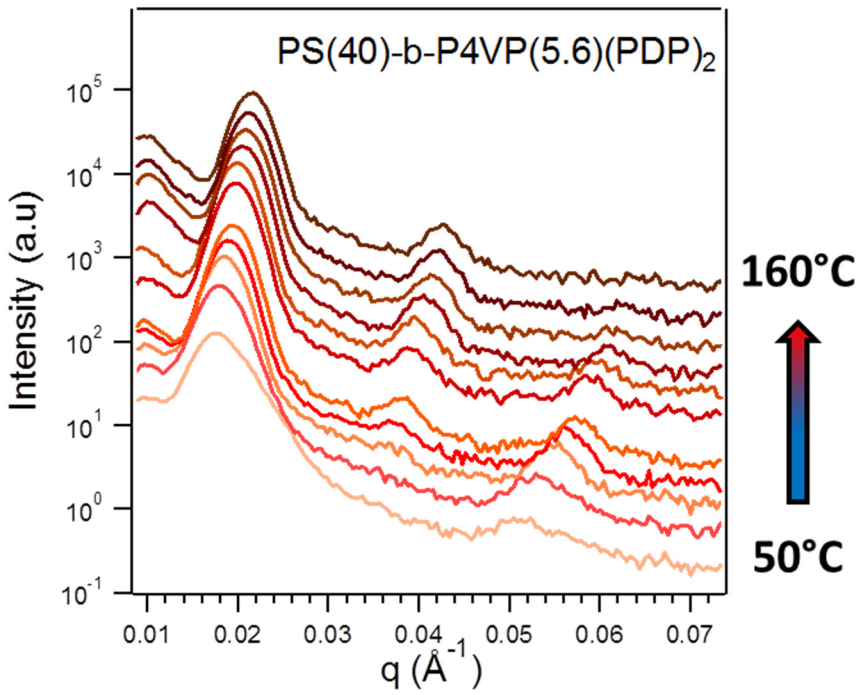

A.1.2. *In-situ* SAXS heating profile of PS-*b*-P4VP(PDP)$_2$ supramolecule. The change in the BCP periodicity upon heating is much smaller (~20%) than **4T**-based supramolecules.

A.1.3

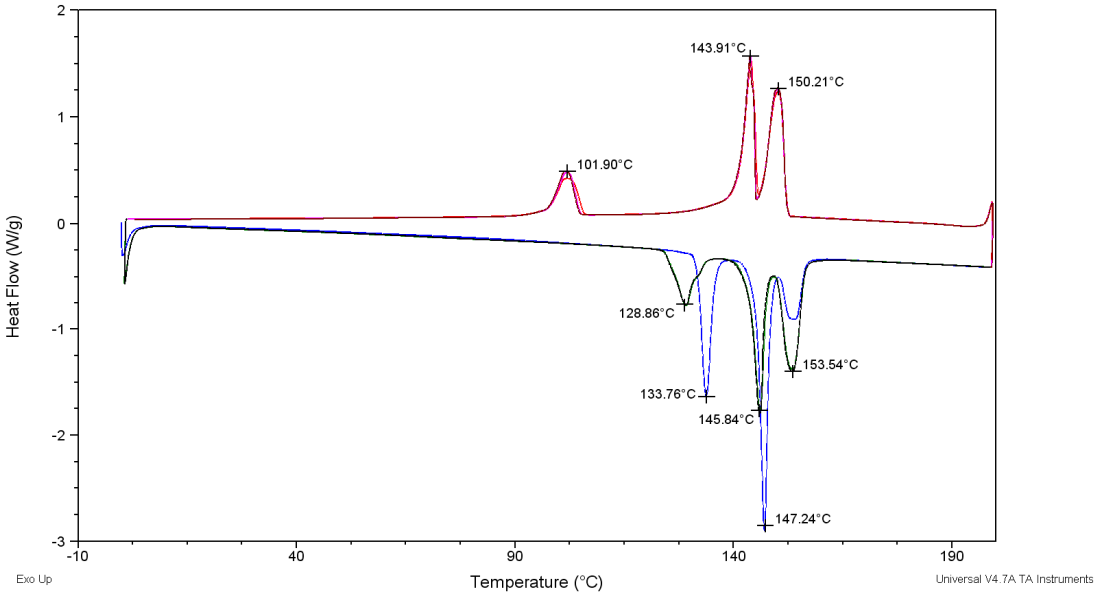

A.1.3. DSC curves during three heating and cooling cycles of P4VP(**4T**)$_{1.5}$ supramolecules. The first heating and cooling cycles are blue and red, respectively.

A.2 Supporting Information for Chapter 4

A.2.1

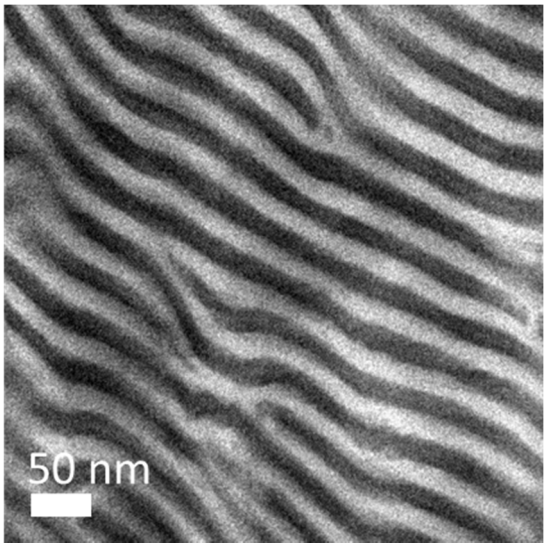

A.2.1. TEM image of PS-*b*-P4VP(**4T**)$_2$ (63 wt% P4VP(**4T**)) supramolecules.